Erratum

Frontiers in Offshore Geotechnics III
Editor: Vaughan Meyer
ISBN: 978-1-138-02848-7

After the publication of the volume, it was noticed that amendment of a few figures in the Third ISSMGE McClelland Lecture 'Cyclic soil parameters for offshore foundation design' by K.H. Andersen on pages 5-82 was required. Please find the correct version of the paper here.

The Publishers

Introduction to Knut H. Andersen, The Third ISSMGE McClelland Lecturer

Knut H. Andersen was born in 1945 in Oslo, Norway, where he has also lived and worked, apart from 4 years study in Trondheim and one year military service in the Norwegian Corps of Engineers.

He received his MSc from the Norwegian University of Science and Technology (NTNU), then named NTH, in Trondheim in 1968 and selected Soil Mechanics as his Major, influenced by the inspiring lectures of Prof. Nilmar Janbu. He went to NGI for his master thesis in 1968 with Carl J. F. Clausen as supervisor. The subject was interpretation of settlement records of two heavy buildings on soft clay (Oslo Jernbanetollsted) which had settled 50 and 70 cm, respectively, over a 50 year period. The thesis work involved valuable practical experience with site investigation and laboratory testing in addition to the theoretical analyses. Dr. Laurits Bjerrum, NGI's first director, followed the work very closely and gave encouraging input and comments.

Dr. Bjerrum offered Knut a position after his thesis, and Knut started as a regular employee at NGI on 1 January 1970, after a year military service in 1969. The continued co-operation with Dr. Bjerrum until his premature death in 1973 shaped Knut as an engineer and has been decisive for his professional career. In line with NGI's philosophy, he has worked on both consulting and research projects, taking advantage of the beneficial interaction between consulting and research.

Knut has had the opportunity to work closely with and co-author publications with all the five NGI directors. In his first years at NGI, Knut had the privilege to assist Dr. Bjerrum in his work on stability and settlement of embankments and structures on soft clay and stability of excavations, which was basis for part of Bjerrum's State-of-the-Art report to the International Conference on Soil Mechanics and Foundation Engineering, ICSMFE, in Moscow in 1973. Knut developed an in-situ technique to measure lateral pressures in clays by hydraulic fracturing during these first years, and he analyzed stresses and displacements in rockfill dams by the finite element method. He was, along with Carl J. F. Clausen, active in introducing and utilizing finite element programs in geotechnical engineering at NGI. This included development and implementation of material models.

The discovery of the Ekofisk field in the North Sea in the late 1960 s caught Dr. Bjerrum's enthusiastic attention and lead to significant new and interesting challenges for NGI. Knut's work was then directed towards offshore foundation engineering, which has been his focus since early 1972. This has involved design of offshore gravity structures, jacket structures, jack-ups, seabed structures, seabed slope stability, and suction anchors in clay, silt, sand and carbonate soil. The work has included practical foundation design, concept development, development of design methods, determination of foundation design parameters,

and planning and interpretation of laboratory tests, model tests and prototype monitoring.

The first involvement was the foundation design of the Ekofisk oil storage tank, which is the first GBS installed in the North Sea on 30th June 1973. Later the involvement has included, to different degrees, most of the gravity platforms installed in the North Sea and a number of others worldwide, covering different soil conditions, ranging from very soft clays to very dense sands, silts, hard clays and carbonate soils. The deepest one is the Troll Platform in 330m water.

Knut participated in the foundation design of the first North Sea tension leg platform with skirted anchors at the Snorre field and in the development of skirted anchors (suction anchors) for anchoring of floaters and skirted foundations for jackets. He was project manager for the large 1-g field testing program of the Snorre TLP skirted anchors at Lysaker in Norway and has been involved in installation and holding capacity design for suction anchors in various soil conditions worldwide.

He has also participated in deepwater geohazard and submarine slope stability evaluations offshore Norway, offshore West Africa and in the Gulf of Mexico. He has established soil parameters for earthquake analyses of structures and slopes for various onshore and offshore locations with different soil conditions, and has participated in evaluation and remediation of accidental leakage from oil wells.

His offshore knowledge and experience has been used for design of harbours and sea flood protection barriers, like the Oosterschelde storm surge barrier in the Netherlands. He also analyzed and evaluated the piers of the western part of the Storebælt Bridge between Funen and Zealand, Denmark, for cyclic loading from waves and from ice sheet drifting from the Baltic Sea.

During the last 10 to 15 years Knut has been active in the development of offshore wind turbine foundations. This includes concept development (monopods, monopiles, skirted multipods, piles, etc.), foundation design analyses (installation, stability, soil stiffness for structural dynamic analyses, cyclic displacements, settlements, permanent displacements, etc.), planning and specification of laboratory and field testing programs of the foundation soil, interpretation of laboratory and field test results, and determination of soil parameters for foundation design for several fields.

Knut has participated in a number of joint industry sponsored research projects (JIP) and been project manager for 12 of them. The first one was the study on cyclic behavior of clay, which was initiated in 1974 in co-operation with 12 industry companies who saw the need for more knowledge about cyclic soil behavior in connection with the foundation design of the first North Sea gravity platforms.

The results from this JIP have formed the basis for NGI's modelling of cyclic soil behavior. Later JIPs have included cyclic behavior of sand; interpretation of prototype performance observations; performance and interpretation of 1g field and model tests on monopod and tripod gravity structures and suction anchors; planning and interpretation of centrifuge tests on gravity platforms and suction anchors; foundation design procedures for gravity platforms, skirted foundations, suction anchors and jack-ups; conductor setting depth for drilling of oil wells; slope stability under cyclic loading from earthquakes and vibrations; interpretation of T-bar and ball penetrometer tests; and soil sampling disturbance and means of correction.

Several of the projects have been performed in co-operation with geotechnical companies and universities in countries outside Norway and sponsored by international oil companies, certifying agencies, research councils, and construction companies. He has also participated in the EU funded projects on foundation design of caisson breakwaters.

Knut has been keynote speaker and chairman and given presentations at a number of international conferences. He gave the 21st Bjerrum Lecture in 2007 and the Distinguished Lecture at the Memorial University of Newfoundland, Canada in 1997. He was examiner for several PhD and MSc theses at AUC, Denmark in the period 1992–96. He is author or co-author of more than 100 contributions to professional journals, books and conferences.

Knut has been member of several international technical committees, including ISSMGE's Technical Committee TC209 on Offshore Geotechnics (2010), ISSMGE's Technical Committee TC1 on Offshore and Nearshore Geotechnical Engineering (2005), ISO TC67/SC7 WG8 Arctic Structures Part 2: TP 3: Foundation Design (2007), and API RG7 Geotechnical Resource Group, Risers and flowlines (2006–2008).

He was chairman of the board of NGI Inc. in Houston from its start in 2002 until 2008.

Knut has wide management experience as project manager for consulting projects and major joint industry sponsored research programs, and management positions at NGI. He was technical director from 1996 to 2012, when he also coordinated NGI's research activities. He reached his retirement age in 2012 and now serves as technical advisor at NGI.

Over the last twenty years, I have had the privilege and honor to work with Knut on many challenging deepwater projects. It is therefore with great pride and pleasure that I, on behalf of the International Society of Soil Mechanics and Geotechnical Engineering and its Technical Committee 209 on Offshore Geotechnics, hereby present him with the Third ISSMGE McClelland Lecture award.

Philippe Jeanjean, Ph. D., P.E., M. ASCE
Chairman, ISSMGE TC209, Offshore Geotechnics
June 10th, 2015

Cyclic soil parameters for offshore foundation design

K.H. Andersen
Norwegian Geotechnical Institute, Oslo, Norway

ABSTRACT: Foundation design of structures subjected to cyclic loading, including stability, cyclic and permanent displacements, soil stiffness for use in dynamic analyses, and soil reactions, requires that effect of cyclic loading is accounted for in the soil parameters. A primary goal of this paper is to provide correlations of these parameters with index parameters for use in practical design. The contour diagram framework for interpretation and presentation of cyclic soil behavior is summarized, as well as pore pressure and cyclic strain accumulation procedures to establish equivalent number of maximum loads, N_{eq}, that gives the same degradation as the irregular cyclic load history. Guidance is given on how the soil parameters can be applied in design, and calculated and measured prototype observations and model test results are used to validate the soil parameter framework. Focus is given to foundation design of structures, but a procedure to analyze the stability of slopes subjected to cyclic loading is also included.

1   INTRODUCTION

I feel honored being asked to present this 3rd McClelland Lecture, and I would like to thank the ISSMGE TC209 committee for inviting me.

I did not have the privilege to meet Bramlette McClelland. The closest I got was in connection with the design of the Ekofisk oil storage tank, which was installed in the North Sea in 1973. The geotechnical site investigation was done by McClelland Engineers, and NGI did the geotechnical design verification on behalf of the Norwegian government through its agent, DNV. I was then a young engineer and was greatly inspired by McClelland's achievements in offshore geotechnical engineering that I learnt about in connection with the Ekofisk project and from the literature.

One of the special issues with offshore structures is that they have to withstand severe cyclic wave loading. In later years wind power structures have also been placed offshore, and these structures will be subjected to significant cyclic loading from the wind in addition to the wave loading. Cyclic loading effects can also be important for structures along the coast and on land. Cyclic loading will influence the strength and deformation characteristics of the soil, and foundation design of these structures requires that the effect of cyclic loading is accounted for in the soil parameters that are applied.

The aim of this paper is to present a framework for cyclic soil behavior that can be used for practical foundation design of structures subjected to cyclic loading, and to provide data and correlations with index parameters that can be used to establish the parameters of this framework for various soil types. Correlations with index parameters are also given for initial shear modulus, static shear strength, friction angle and consolidation characteristics (compressibility and permeability), since these parameters are also needed in cyclic foundation design.

The correlations can help estimate parameters for feasibility studies before site specific data are available and guide specification and interpretation of site specific laboratory programs. This guidance will help reduce the required number of site specific tests and provide quality control of the test results. The correlations naturally contain some scatter and cover a limited number of soil types. For final design, the parameters from correlations should be verified by site specific tests to avoid unwanted error or conservatism.

Some of the correlations have been presented in previous publications, but they have been updated and revised by including more data and additional variables. The correlations are primarily valid for non-calcareous soils, but some correlations for DSS type of shearing are also given for calcareous soils.

The paper first gives examples of cases where cyclic loading is important, and presents the foundation design aspects and the parameters required for the foundation design. It continues by explaining what happens to the soil when subjected to cyclic loading and presents a contour diagram framework to characterize the cyclic soil behavior. The contour diagram framework has been applied in offshore foundation design for many years (e.g. Andersen et al. 1988, Andersen & Lauritzsen 1988, Andersen & Høeg 1991).

It is therefore not a new concept, but it is summarized herein as background for the correlations. Advice is also given about aspects that are important to consider when establishing cyclic contour diagrams. The contour diagrams can be used directly in design, as shown later, or they can be used to develop mathematical cyclic soil models. Since the contour diagrams represent non-manipulated data, mathematical models should be verified by checking that they can reproduce the contour diagrams and the various stress conditions that these diagrams cover.

The cyclic load history is normally non-symmetrical and irregular, and may need to be transformed into a simplified, more regular form. It is shown how this can be done and how the regular history can be applied in a pore pressure or a cyclic strain accumulation procedure to establish an equivalent number of maximum cyclic loads, N_{eq}, that gives the same cyclic degradation as the irregular cyclic load history. The accumulation procedures have also been applied for many years (e.g. Andersen 1976, Andersen et al. 1992 & 1994) but their use to establish N_{eq} as well as stress strain relations and cyclic shear strength has not been fully explained in previous publications.

Following individual cycles through a cyclic load history with hundreds or thousands of cycles is not considered feasible in practical design, and the contour diagram framework is defined in terms of cyclic amplitudes, meaning that the stress-strain relation within individual cycles is not defined. A procedure is proposed, however, that can be used to define the load displacement relationship within a cycle at a given time in the load history.

Focus is given to the foundation design of structures, but a procedure to analyze the stability of a slope subjected to cyclic loading, as from an earthquake, is proposed towards the end of the paper.

Comments and guidance are given on how the soil parameter framework can be applied in design, and predicted and backcalculated prototype observations and model test results are presented as validation.

Valuable work on cyclic soil behavior is done in many organizations internationally, but this paper concentrates on models developed and applied at NGI.

The content of the paper is organized in sections as follows:

2 CASES WITH CYCLIC LOADING

Cyclic loading effects have been given most attention in connection with foundation design of offshore structures, traditionally for oil and gas production, and more recently also for offshore wind power structures. The offshore structures can be fixed to the seafloor by their own weight (gravity platforms) or by piles, or the foundations can be monopiles or skirted foundations. The offshore structures can also be floating, and the foundation design then consists of designing the anchors for the mooring system, which can be suction anchors, piles, drag anchors or gravity anchors.

Cyclic effects can also be important for foundation design of structures along the coast and on land, such as harbors, breakwaters, storm surge barriers, wind power structures, and for vibrations from infrastructure and industry. Earthquakes will create cyclic stresses in the soil, and influence the stability of slopes and the behavior of buildings and other structures, both on land and offshore.

3 CYCLIC LOADING CHARACTERISTICS

Cyclic loads can have different origins and vary significantly in amplitude, period and duration. The origin can be waves, wind, drifting ice sheets, icebergs, earthquakes, tidal variations, traffic, blasting, machine vibrations, and emptying and filling of storage. The cyclic loading characteristics can thus vary considerably. For instance, wave loading will typically have a period of 10 to 20 s and the storm event can have a duration of the order of 1 day and contain some thousand cycles. The cyclic load history will be irregular with a cyclic amplitude varying from one wave to the next. In many cases there can also be an average load component that can vary during the storm. On the other hand, earthquakes may have a duration of about 10 to 30 s, a load period of $\sim$1 s and some tens of cycles, whereas tidal forces and storage variations can have a period of 12hrs and more. Different sources may also generate cyclic loading simultaneously, like wind and wave for an offshore wind power structure. Resonance of the structure can also be a source that generates additional cyclic loading on the soil as a reaction to the primary source. An example is the Great Belt Bridge where breaking ice sheets set the pillars in motion, thus generating cyclic loading with a period of $\sim$1 s superimposed on the primary $\sim$10 s cyclic loading period from the ice sheets (Andersen 2009).

More examples and details of cases with cyclic loading can be found in Andersen (2009), Jardine et al. (2012) and Andersen et al. (2013).

4 FOUNDATION DESIGN REQUIREMENTS

The major requirements to be addressed in cyclic foundation design are to:

- ensure sufficient capacity. The capacity under cyclic loading can differ significantly from the capacity under monotonic drained or undrained loading, especially if the cyclic loading involves net load reversal. One example showing the importance of load reversal is the capacity of driven piles for jacket structures where the capacity of the piles of the windward leg can be lower than for the leeward leg because of greater load reversal for the windward leg (Jardine et al. 2012, Andersen et al. 2013).

  For structures it is normally the capacity to carry the cyclic loads that is critical, since the safety against a failure under static load is high in most cases. For slope stability, however, the safety against failure under the static slope weight can be low, and one must also ensure that the temporarily reduced static capacity due to cyclic loading (e.g. from an earthquake) during and some time after the cyclic event is sufficient to carry the weight of the slope.
- demonstrate that cyclic displacements are tolerable. Cyclic displacements can be a serviceability problem, and may also induce stresses in structural elements in the soil or connections to the structure, like oil wells, risers and pipeline connections. All displacement components (vertical, horizontal and rotational) need to be determined, as for instance a rotation at seabed can lead to significant horizontal displacements at deck level for a tall structure.
- provide equivalent soil spring stiffnesses and damping for use in global dynamic soil-structure analyses

and earthquake analyses. The cyclic soil spring stiffnesses are especially important for tall and slender structures as they can influence the resonance frequency. If the resonance frequency approaches the cyclic load frequency the dynamic load amplification will increase. The cyclic soil spring stiffness is especially important for wind turbines, where the resonance frequency should be within a relatively narrow band determined by the operational rate of rotation. Soil spring stiffnesses in terms of both cyclic and average components can also be important for multi-legged structures, as the soil stiffness will determine the distribution of the loads between the legs. Soil damping is not always important, but may be of relevance for tall and slender structures.

- assess whether increased long term permanent displacements due to cyclic loading are tolerable. The predominant permanent displacement will normally be increased vertical settlements in case of a gravity based structure or structures with more or less symmetrical loads, but permanent rotational displacements must also be considered if the loads are not symmetrical or if there are lateral variations in the soil profile. For structures with large horizontal loads, like wind turbines, there can be significant permanent horizontal and rotational displacements. The permanent displacements will accumulate over the lifetime of the structure, and it is necessary to consider more than a single design storm. The calculation of permanent displacements must include components from both permanent shear strains during cyclic loading, increased creep rate due effective stress reduction from cyclic loading, and volumetric strains from dissipation of cyclically induced pore pressure and due to shear induced dilatancy.
- assess how cyclic loading can alter the base and side soil reaction stresses. The cyclic loading can cause redistribution along the base or the side, but also a redistribution between the base and the side, as observed in model tests of skirted foundations in sand (Jostad et al. 1997).

All requirements are not relevant for all structures. For anchors, for instance, sufficient capacity is the main requirement, and displacements are not important. The requirements above are discussed in more detail and illustrated by examples in Andersen (2004) and Andersen et al. (2013).

5 SOIL PARAMETERS FOR CYCLIC FOUNDATION DESIGN

The soil parameters needed to address the foundation design requirements are grouped into cyclic soil data, monotonic soil data and consolidation characteristics. More conventional parameters, like index properties, preconsolidation pressure and overconsolidation ratio are not addressed herein, even if they are also required in a cyclic foundation design.

As mentioned earlier, all foundation requirements in Section 4 are not relevant for all types of structures, and the type and amount will be case specific. Further discussion about soil parameters needed for different cases and their determination can be found in Andersen et al. (2013).

5.1 Cyclic soil data

Cyclic soil behavior and parameters are described in detail and defined in the next section, but a brief summary of required cyclic parameters is given below.

Cyclic shear strength will be required as a function of average shear stress and number of cycles.

The following parameters will be needed as functions of cyclic and average shear stresses and number of cycles:

- Cyclic, average and permanent shear strains
- Permanent pore pressure
- Volumetric strain
- Damping
- Post cyclic static shear strength

The cyclic soil parameters are anisotropic and depend on stress path. Thus, compression, DSS and extension tests are needed, unless the foundation behavior is governed by one type of stress path, as for horizontal sliding of a gravity platform. The post cyclic shear strength is normally only needed in special cases, like slope stability under earthquake loading. Damping may be most important for tall and slender structures and earthquakes. Volumetric strains can be calculated based on permanent pore pressure and reconsolidation modulus, or determined from drained cyclic tests, as discussed in Section 18.3.

5.2 Monotonic data

Monotonic data provide a useful reference for the cyclic soil parameters and are needed to construct the cyclic contour diagrams presented in subsequent sections. In clays, it is convenient to normalize the cyclic parameters by the undrained monotonic shear strength. For piles, the capacity for monotonic loading is needed if the cyclic capacity is evaluated from interaction diagrams or degradation laws where the cyclic capacity is normalized to the monotonic capacity (Jardine et al. 2012, Andersen et al. 2013). Monotonic parameters will also be needed if the cyclic load history or the drainage conditions are such that there is little pore pressure generation prior to the maximum wave.

5.2.1 Undrained parameters
Undrained monotonic parameters that may be needed for both clay and sand are:

- Undrained shear strength
- Undrained stress-strain response

Both the shear strength and the stress strain response are anisotropic, and compression, DSS and extension tests may be needed.

5.2.2 *Effective stress parameters*

The following effective stress parameters may be required for sand in cases where undrained conditions may not be assumed to apply:

– Drained triaxial peak friction angle and slope of failure line in drained DSS tests
– Undrained triaxial effective stress friction angle and slope of effective stress failure line in undrained DSS tests
– Dilatancy angle to determine shear induced volume changes
– Interface friction angles to consider base sliding for shallow foundations and shaft friction for piles.

5.2.3 *Initial shear modulus*

The stress strain response is non-linear, and it is important to know the initial shear modulus in order to model the stress strain behavior properly.

The initial shear modulus may be needed not only near the structure. The small strain response in the far-field can be important because the strain is integrated over a large volume and can give an important contribution to the cyclic displacements and soil stiffness even if the modulus is high.

The initial shear modulus can be determined from bender elements, resonant column tests and in-situ shear wave testing.

5.3 *Consolidation characteristics*

The consolidation characteristics are needed to calculate the dissipation rate of the pore pressure generated by cyclic loading and the magnitude and rate of permanent displacements due to this pore pressure dissipation.

The consolidation characteristics are defined by:

– Virgin, unloading and reloading moduli
– Coefficient of consolidation.

The consolidation characteristics can be determined from oedometer tests, but for clean sand the flow resistance in filters and tubes may be high compared to the flow resistance in the sand specimen, and triaxial tests with low flow resistance can be required to measure the coefficient of consolidation.

6 CYCLIC SOIL BEHAVIOR

6.1 *Typical stress conditions*

The stress conditions in the soil around a foundation subjected to cyclic loading are complicated. A simplified picture of the shear stresses along a potential failure surface in the soil beneath a shallow foundation is shown as an example in Figure 6.1. The elements follow various stress paths (compression, DSS and extension), and they will experience different combinations of average shear stress, τ_a, and cyclic shear stress, τ_{cy}.

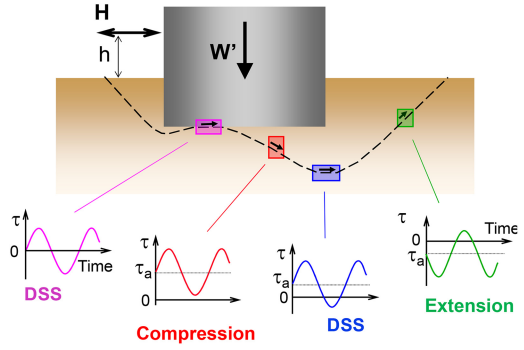Figure 6.1. Simplified stress conditions for typical elements along a potential failure surface beneath a shallow foundation.

In this paper, τ denotes the shear stress on the 45° plane in compression and extension elements and on the horizontal plane in DSS tests. The cyclic loading is stress-controlled, since this is considered to be the best representation for cyclic events defined in terms of loads. This is further discussed in Section 8.2.4.

The average shear stress, τ_a, can be expressed as $\tau_a = \tau_0 + \Delta\tau_a$, where:

– τ_0 is the initial shear stress in the soil prior to the installation of the structure, $\tau_0 = 0.5 \cdot (1 - K_0) \cdot p'_0$ in triaxial tests, and $\tau_0 = 0$ in DSS tests. p'_0 is the vertical effective overburden pressure, and K_0 is the coefficient of earth pressure at rest. The initial shear stress, τ_0, acts under drained conditions, and the soil is consolidated under this stress.
– $\Delta\tau_a$, is the additional shear stress which is induced by the submerged weight of the structure and any average environmental loads. $\Delta\tau_a$ will first act under undrained conditions, but as the soil consolidates, $\Delta\tau_a$ will also act under drained conditions. In the case of sand, drainage will occur relatively rapidly, and it is reasonable to assume that the soil consolidates under the weight of the platform before the design storm arrives. Whether the part of $\Delta\tau_a$ due to environmental loads will act undrained or drained will depend on drainage distance, consolidation characteristics of the sand and the variation of the average load during the cyclic loading event. As shown later, the drainage conditions for $\Delta\tau_a$ can have significant impact on the cyclic shear strength. Consolidation occurs much slower for clays, and when conservative it must be assumed that the design storm occurs before any significant consolidation has taken place.

The cyclic shear stress, τ_{cy}, is caused by the cyclic loads. In general, environmental loads and period vary continuously from one cycle to the next, and the cyclic shear stress will also vary from cycle to cycle.

To determine the soil properties needed in the foundation design analyses, the laboratory tests should first be consolidated to the *in situ* effective stresses, and then subjected to shear stresses that simulate the stress

conditions of the various elements *in situ* during cyclic loading as closely as possible. With existing types of laboratory equipment it is not possible to reproduce all different *in situ* conditions. However, triaxial and DSS tests give reasonable approximations to important stress conditions. One may argue that the intermediate principal effective stress in the prototype is not well modelled in triaxial and DSS tests (Andersen et al. 2013), but triaxial and DSS tests are widely used in design for practical reasons. Prediction and backcalculation of prototype observations and model tests presented in a Section 20 indicate that this is an acceptable approach.

6.2 *Soil behavior under undrained cyclic loading*

Cyclic loading will generally tend to break down the soil structure and cause a tendency for volumetric compression. If the soil is saturated and the conditions are undrained, the volumetric changes will be prevented by the compressibility of the water, which is low compared to the compressibility of the soil skeleton. Part of the normal stresses carried by the soil skeleton will thus be transferred to the pore water, and the effective stresses in the soil will decrease accordingly. This is illustrated by the effective stress paths of a soft soil subjected to monotonic and cyclic loading in Figure 6.2. In the monotonic test the soil exhibits a peak shear stress, softens and approaches and follows the failure envelope. In the cyclic test the soil is loaded with a maximum shear stress that is smaller than the peak shear stress in the monotonic test. The load cycles with a single amplitude shear stress, τ_{cy}, around a constant shear stress, τ_a. During the first cycle the stress path forms a loop that ends up to the left of the initial effective stress, corresponding to a permanent pore pressure, u_p. Each cycle gives an additional incremental pore pressure, and after some cycles the stress path reaches the failure envelope. The shear strains may not necessarily become excessive once the failure line is reached, as the soil may dilate and follow the failure line. This is especially true for dense sand that can have strong dilative properties. Dense sand can exhibit limited shear strains even if the pore pressure gives essentially zero effective stresses when the shear stress passes through zero, because the soil tends to dilate when it experiences shear strains. The dilative capability will, however, be broken down with number of cycles. This is illustrated by examples in the following subsection.

The development of pore pressure and shear strain with time for a soil element subjected to undrained cyclic loading with a constant cyclic shear stress is illustrated in Figure 6.3. The cyclic loading generates a pore pressure characterized by a permanent pore pressure component, u_p, and a cyclic pore pressure component, u_{cy}. The increased pore pressure reduces the effective stresses in the soil, resulting in increased average, γ_a, permanent, γ_p, and cyclic, γ_{cy}, shear strains with time. The stress-strain behavior of a soil element under the cyclic loading in Figure 6.3
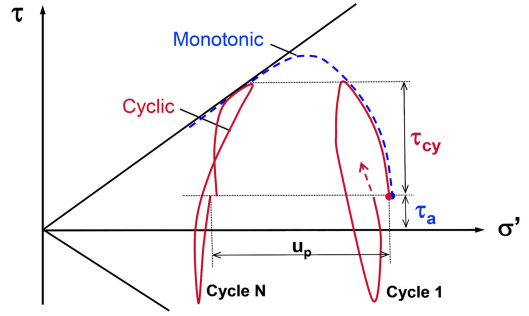

Figure 6.2. Effective stress paths for undrained tests with monotonic and cyclic loading in a contractant soil.
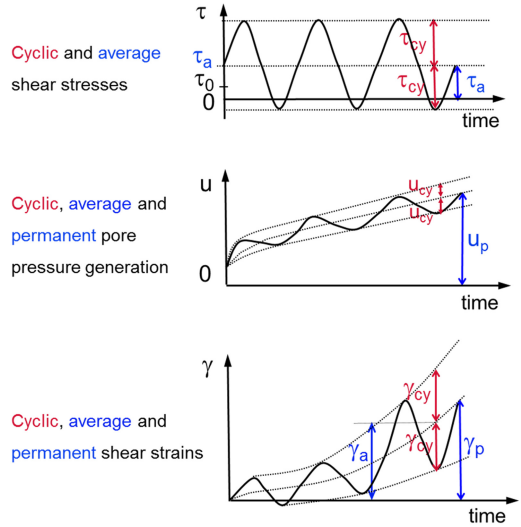

Figure 6.3. Pore pressure and shear strain as functions of time under undrained cyclic loading.

is illustrated in Figure 6.4. The stress strain curve is non-linear and each cycle describes an area that gives hysteretic damping.

The pore pressure and shear strain components are defined as follows:

– The permanent pore pressure, u_p, and the permanent shear strain, γ_p, are the values at the end of a cycle when the shear stress returns to the shear stress at the start of the cycle
– The cyclic pore pressure, u_{cy}, and the cyclic shear strain, γ_{cy}, are the single amplitude values, i.e. half the peak to peak values within a cycle
– The average pore pressure, u_a, and the average shear strain, γ_a, are the average of the high and low peak values within a cycle

The hysteretic damping is defined by the area within the stress strain loop.

The most important components for design are the permanent pore pressure and the cyclic, average and permanent shear strains.
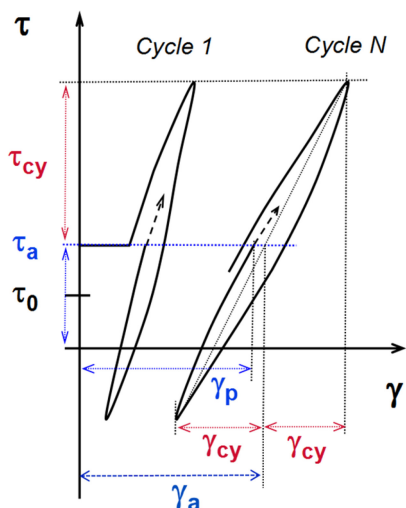
Figure 6.4.   Stress-strain behavior under cyclic loading.

The permanent pore pressure can be used to quantify the accumulated effect of cyclic loading during a cyclic event. Especially for sand, where dissipation of pore pressure can occur in parallel with the pore pressure generation, pore pressure is the preferred parameter (e.g. Andersen et al. 1994). Permanent pore pressure is a fundamental parameter for clay also, but it is more challenging to measure cyclic pore pressure reliably in clay in the laboratory. Due to rapid stress changes and short testing durations the requirement to the system compliance can be difficult to fulfill. For clay, the conditions are normally undrained during the design event, and simultaneous drainage is normally not an issue. Cyclic shear strain has therefore been used as parameter to quantify the accumulated effect of cyclic loading in clay, e.g. Andersen 1976. The permanent pore pressure at the end of the cyclic event may still be needed for clays, however, as input to calculate the permanent displacements from volumetric strains due to dissipation of permanent pore pressure. The pore pressure and cyclic shear strain accumulation procedures are described in Section 8.

The cyclic shear strain is the primary parameter to calculate cyclic displacements and soil spring stiffnesses. The cyclic shear strain is the single amplitude value, and does not define the behavior within a cycle. A procedure to model individual cycles is presented in Section 18.5.

The average shear strain is needed in addition to the cyclic shear strain to calculate the maximum shear induced displacement during the cyclic loading event, which is the sum of average and cyclic components. Volumetric strain during the cyclic event occurs in addition for cases with drainage.

The permanent shear strain is needed to calculate the shear induced permanent displacements that will remain after the cyclic loading event has ended. Traditionally, the permanent shear strain has not been given specific attention, and often assumed to be the same

as the average shear strain. This is discussed further in Section 7.4.

The permanent pore pressure is needed to calculate the volumetric strain when this pore pressure dissipates during and/or after the cyclic event, as explained in Section 18.

Damping may be needed in some cases for tall and slender structures which may have resonance frequencies close to the cyclic load frequency.

6.3   *Examples of laboratory test results*

Examples of stress-strain behavior of soil elements under various loading conditions are presented in Figures 6.5 and 6.6.

Figure 6.5 shows results from laboratory tests on Drammen Clay, a marine clay with a plasticity index of $I_p = 27\%$. The first two tests in Figure 6.5 have symmetrical cyclic loading with about the same cyclic shear stress, but they behave differently and show that the response to symmetrical cyclic loading is different in DSS and triaxial tests. In the DSS tests, the shear strain develops relatively symmetrically, apart from the first quarter cycle, which is a virgin loading. The remaining loading is unloading and reloading. In the triaxial test, the shear strain development is non-symmetrical with an average shear strain of about the same magnitude as the cyclic shear strain. This is due to the strength anisotropy under triaxial loading, with an extension strength that is smaller than the compression strength. The triaxial test also develops large shear strain at a lower number of cycles than the DSS test, even if the cyclic shear stress is about the same in the two tests.

The third test in Figure 6.5 has a shear stress with equal average and cyclic components. The result is a shear strain development where the average and permanent shear strains dominate and increase with number of cycles. The small cyclic shear strain does not increase significantly with number of cycles. The maximum shear stress is greater than in the second test, but the strain development is significantly smaller for a given number of cycles.

Figure 6.6 shows that the cyclic behavior is not governed by the maximum shear stress alone and that the strain development under cyclic loading cannot be explained by creep. The three tests in Figure 6.6 have the same maximum shear stress, but different average and cyclic shear stress components. The test with $\tau_a = 0$ fails after 10 cycles, whereas the tests with $\tau_a = 0.5 \cdot \tau_{max}$ and $\tau a = 0.85 \cdot \tau_{max}$ have developed only small shear strains after 2500 cycles, and the test with the highest τ_a has the smallest shear strains.

Figure 6.7 shows three examples of triaxial tests on very dense Dogger Bank sand. The tests are all consolidated with a vertical consolidation stress of $\sigma'_{vc} = 200$ kPa and a ratio of horizontal to vertical effective stress of $K_0 = 0.45$, corresponding to an initial shear stress of $\tau_0 = 55$ kPa. The first test is cycled around τ_0. In the two other tests, the average shear stress is increased to 140 kPa in the second test and
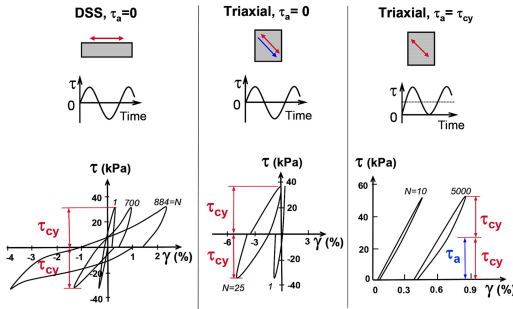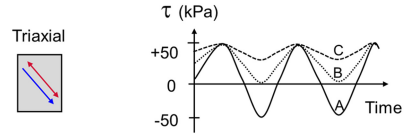
Figure 6.5. Stress-strain behavior of Drammen Clay ($OCR = 4$) under various cyclic loading conditions.

Test	τ_{max}	τ_a	τ_{cy}	Result
A	50	0	50	Failure (γ=15%) 10 cycles
B	50	25	25	γ_p=0.8%, γ_{cy}=0.3% 2500 cycles
C	50	42.5	7.5	γ_p=0.03%, γ_{cy}=0.02% 2500 cycles

Figure 6.6. Results from cyclic triaxial tests on Drammen clay with the same maximum shear stress.

reduced to -140 kPa in the third test before applying cyclic loading. The average stress changes are done by changing the vertical normal stress under drained conditions. A cyclic shear stress of $\tau_{cy} = 200$ kPa was applied under undrained conditions in all three tests. The failure envelope from a monotonic test, defined by a friction angle of $\phi'_u = 43.4°$, is included as reference in the effective stress path plots.

As discussed in connection with Figure 6.2, the pore pressure generated during cyclic loading causes the effective stress path to approach the failure envelope. The cyclic shear stress of 200 kPa gives a high degree of mobilization, and all three tests reach the failure envelope in the first quarter of the first cycle, but without developing large shear strains. As discussed in the Section 6.2, this is possible because the dilation that tends to occur in dense sand when it is sheared is prevented when the conditions are undrained and water cannot flow in or out of the soil element. The tendency for volumetric expansion then gives a negative pore pressure and a corresponding effective stress increase. As cycling continues the stress path repeatedly reaches and follows the failure envelope during a large part of each cycle. The soil structure is gradually broken down, and as cycling continues, larger strains are required to mobilize negative pore pressure. The shear strain increase with number of cycles is normally quite slow in very dense sand. A loose to medium dense sand that does not dilate under monotonic loading will fail more suddenly once the failure envelope is approached.

The shear strain development and failure mode in the three tests in Figure 6.7 is significantly different, even if the cyclic shear stress is the same. The first test with a somewhat higher shear stress in compression than in extension develops essentially cyclic shear strain and small average and permanent shear strains. A high pore pressure is generated, and when the shear stress passes through zero, the effective stresses are essentially zero after less than 25 cycles. The sand is then in an essentially liquefied state, and when the shear stress is increased, the shear strain increases significantly for small additional shear stress. Due to the dilative behavior of the dense sand, however, the shear strain increase slows down and the stiffness increases

significantly after some shear strain has occurred. The shear strain required to arrest the shear strain increases with number of cycles and can become large if cycling is continued.

The test with an increase in average shear stress ($\tau_a = 140$ kPa) experiences a gradual increase in the average compressive strain with number of cycles while the cyclic shear strain remains essentially constant. Failure will result from large average and permanent compression shear strains if cycling is continued. The test with a decrease in average shear stress ($\tau_a = -140$ kPa) will behave in a similar manner, but the average and permanent shear strains will be to the extension side and somewhat larger than on the compression side.

The effective stress paths of all three cyclic tests in Figure 6.7 agreed well with the failure envelope for the monotonic test.

The examples in Figures 6.5 to 6.7 illustrate that cyclic behavior depends on both average and cyclic shear stresses, and that the behavior is different in triaxial and DSS tests. The behavior will also depend on soil type, plasticity (for clay) and density (sand), overconsolidation ratio and whether the average shear stress is drained or undrained. Section 7 describes how this complex behavior can be systemized in the form of contour diagrams.

6.4 *Strength limitation due to drainage within a cycle and cavitation*

6.4.1 *Drainage within a cycle*
The cyclic data presented in this paper assumes that the soil is water saturated and undrained within a cycle. Static and cyclic undrained shear strengths are defined and discussed later.

Undrained conditions can be violated near drainage boundaries or for cases with short drainage path for high permeability soils like clean sand. In contractive soils, like soft clay or silt, drainage may be beneficial, but dilative soils, like dense sand, may reduce or lose its ability to develop negative pore pressure. If negative pore pressure cannot be relied upon, the shear strength will be governed by the effective stresses and depend
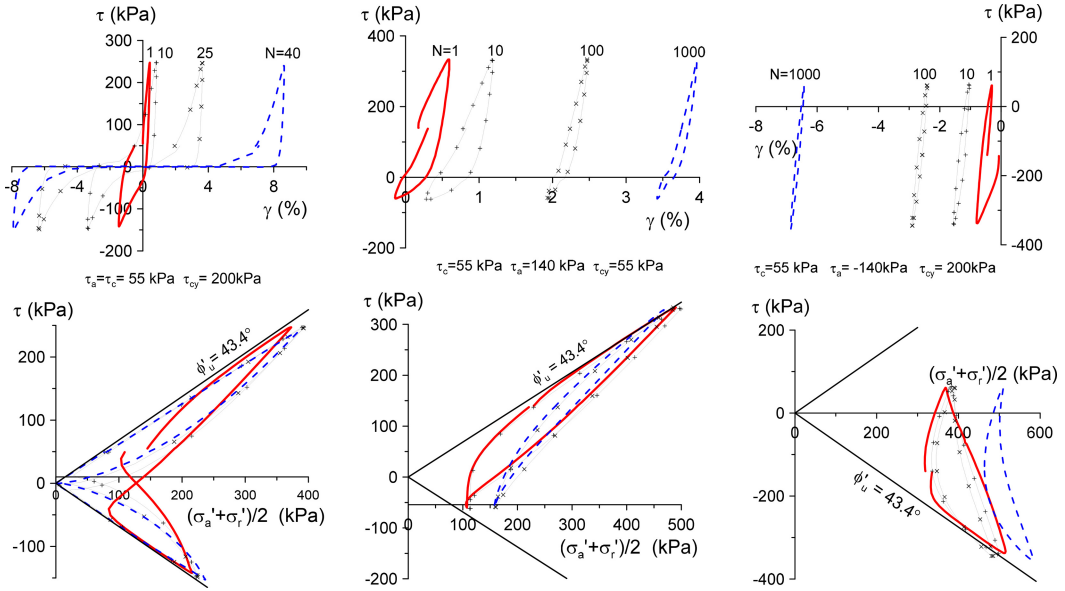
Figure 6.7. Stress-strain behavior in triaxial tests on clean Dogger Bank Sand with relative density of $D_r \sim 95\%$ and water content of $w \sim 22.5\%$ under different average shear stress (Blaker & Andersen 2015).

on the stress path defined by the total normal stresses. The shear strengths for some triaxial and DSS total stress paths are presented in Figure 6.8.

When evaluating drainage during a single cycle, one should keep in mind that the dilatancy is a function of shear strain and that the volumetric strain and the tendency for negative pore pressure within a cycle become non-linear functions of time. Pore pressure drainage solution that start with an initial pore pressure that dissipates with time can therefore overestimate the effect of drainage and be conservative for this purpose in dense sand.

6.4.2 *Cavitation*

Air can come out of solution in the pore water in a water saturated soil if the pore water pressure becomes negative with a magnitude equal to the atmospheric pressure. This has been demonstrated in triaxial laboratory tests on sand (e.g. McManus & Davis 1997) and observed in centrifuge model tests on dense sand (e.g. Andersen et al. 1994).

The soil does not lose its strength when the pore water in sand cavitates, but the soil behavior will change from undrained to drained. The effective stress path transforms from undrained to drained, and the sand fails at the drained failure envelope defined by the peak drained friction angle instead of at the failure envelope defined by the undrained effective stress friction angle. The behavior can change back to undrained if the stress changes direction in a manner that induces compression in the sand. The air that has come out of the water may then go into solution again, accompanied by some volumetric strain.

Cavitation has not been an issue in deep water foundation design since the water depth provides a high
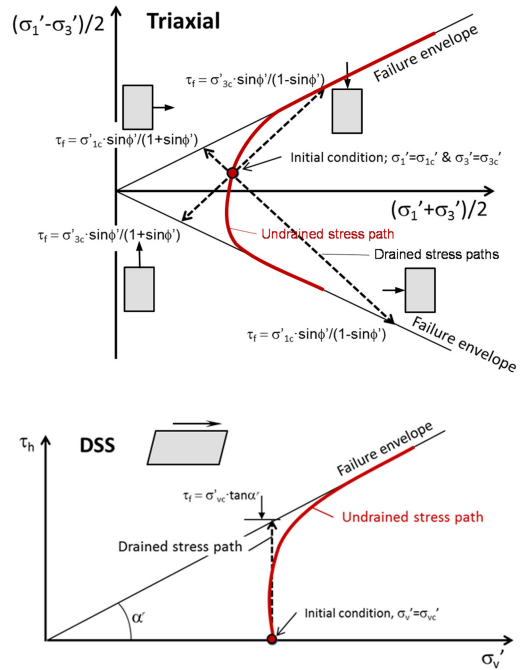
Figure 6.8. Shear strength for triaxial and DSS total stress paths with and without dilatancy (i.e. undrained and drained). ϕ' is the effective stress friction angle and α' is the slope of the failure line for DSS loading.

backpressure. In shallower water, like most wind farm sites, the backpressure is smaller and cavitation can be an issue that needs consideration in cases with tension loads or in dense dilatant sands.

Section 6 shows that the cyclic strength and deformation characteristics depend on both average and cyclic shear stresses, and that the behavior is different in triaxial and DSS tests. It was therefore found convenient to present the cyclic behavior in contour diagrams where the cyclic parameters are given as functions of average and cyclic shear stresses and number of cycles and in separate diagrams for DSS and triaxial tests (e.g. Andersen et al. 1988; Andersen & Lauritzsen 1988). Contour diagrams have formed the basis for practical foundation design of offshore structures for many years and are therefore not a new concept (e.g. Andersen 1991, Andersen & Hoeg 1991, Andersen et al. 1994). Since the contour diagrams represent a compilation of directly measured data without modification, they can also be used to develop other soil models and to provide data to such models. New models should be verified by showing that they can reproduce the contour diagrams and the various stress conditions that these diagrams cover.

The contour diagram concept is summarized in this section as background for the correlations in later sections and to be able to address aspects that are of importance when establishing cyclic contour diagrams.

The contour diagrams consist of a set of diagrams illustrated in the following by using normally consolidated Drammen Clay as an example. Drammen Clay is a marine clay with a plasticity index of about 27%. The shear stresses are normalized to the undrained static shear strength, s_u^{DSS} for DSS tests and s_u^C for triaxial tests, measured in strain-controlled tests with a rate of shear strain of 3–4.5%/hour. For sand and silt it is more common to normalize to the vertical effective normal stress, as discussed later.

In the Drammen Clay examples, the change in average shear stress, $\Delta\tau_a$, is applied undrained and allowed to act for about 1 to 2hrs before cyclic loading is applied. The intersection of contours with the horizontal axis depends on the rate of the monotonic test and the duration of τ_a. The cyclic loads are applied with a period of 10 s. The effect of applying $\Delta\tau_a$ under drained conditions and the effect of load period are discussed later.

7.1 Number of cycles to failure

The diagram in Figure 7.1 presents the number of cycles to failure in DSS tests as a function of τ_a and τ_{cy}. The diagram is based on a number of stress-controlled tests, each with a different combination of constant τ_a and τ_{cy}. Each point in Figure 7.1a represents one test. The numbers written beside each point represent the number of cycles to failure and the failure mode, i.e. the combination of γ_a and γ_{cy} at failure, for that test. Failure is defined as when either γ_a or γ_{cy} reaches 15%. By interpolation and extrapolation of the test results, curves defining the combinations of τ_a and τ_{cy} that cause failure after different number of cycles can be
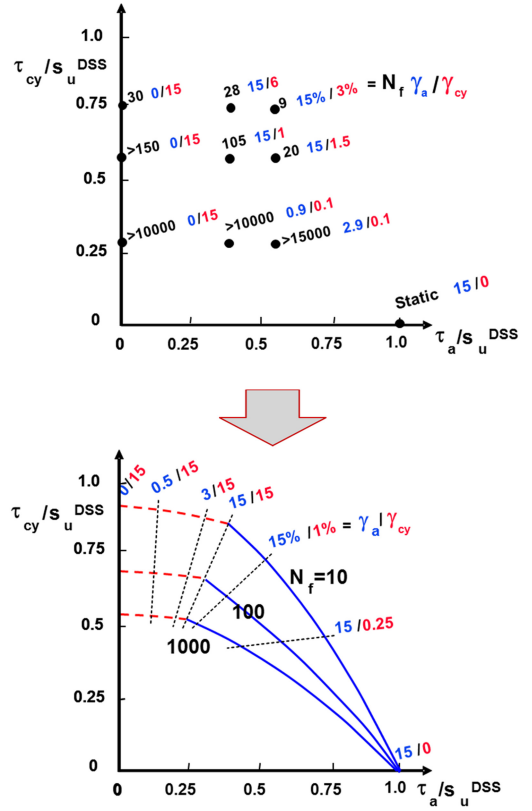

Figure 7.1. Construction of contour diagram with number of cycles to failure as a function of average and cyclic shear stresses. DSS tests on normally consolidated Drammen Clay.
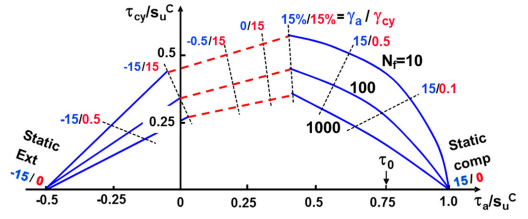

Figure 7.2. Contour diagram with number of cycles to failure as a function of average and cyclic shear stresses. Triaxial tests on normally consolidated Drammen Clay.

drawn, as shown in Figure 7.1b. The intersection of the curves with the horizontal axis is defined by the static shear strength. The failure mode (i.e. γ_a and γ_{cy} at failure) is defined by the thinner dotted curves.

The behavior is different in triaxial and DSS tests. Separate diagrams are therefore presented for DSS and triaxial tests. Diagrams for triaxial tests, as shown in Figure 7.2 can be established in the same way as for DSS tests.

The diagram in Figure 7.1 shows that in DSS tests the failure mode will be large γ_{cy} for small to moderate τ_a values, and large γ_a for τ_a values approaching the undrained static shear strength. In the triaxial tests,
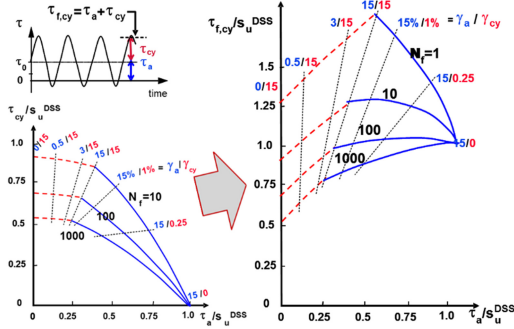
Figure 7.3. Cyclic DSS shear strength. Normally consolidated Drammen Clay.

Figure 7.2 shows that the failure mode will be large compression γ_a for τ_a approaching the static triaxial compression strength, large extension γ_a for τ_a approaching the static triaxial extension strength, and large γ_{cy} for small and moderate values of τ_a.

The contours are valid for stress-controlled tests with constant shear stresses. Real cyclic load histories will have shear stresses that vary from one cycle to the next. Ways to transform irregular cyclic load histories into equivalent number of cycles with constant shear stress are presented in Section 8.

7.2 *Cyclic shear strength*

The cyclic shear strength, $\tau_{f,cy}$, is the peak shear stress that can be mobilized during cyclic loading (e.g. Andersen & Lauritzsen 1988); i.e.:

$$\tau_{f,cy} = (\tau_a + \tau_{cy})_f$$

where $(\tau_a + \tau_{cy})_f$ is the sum of the average and cyclic shear stresses at failure, as also illustrated in the time history sketches included in Figures 7.3 and 7.4.

The cyclic shear strength can be determined from the diagrams in Figures 7.1 and 7.2. The result is presented in Figures 7.3 and 7.4, which show that the cyclic shear strength depends on τ_a, the cyclic load history (i.e. number of cycles), and the type of test (i.e. the stress path). For triaxial tests there is a difference between the cyclic shear strengths in compression and extension, since compression failure occurs when the shear strain is positive, whereas extension failure occurs when the shear strain is negative.

As indicated by the thin dotted curves in Figures 7.3 and 7.4, cyclic failure can occur either as large cyclic shear strains, large average shear strains, or as a combination of the two, depending on τ_a.

The diagrams in Figures 7.3 and 7.4 show that the cyclic shear strength can be greater than the static shear strength. The reason is that the cyclic load is applied much faster that the monotonic load and that there is a rate effect, as illustrated in Figure 7.5.
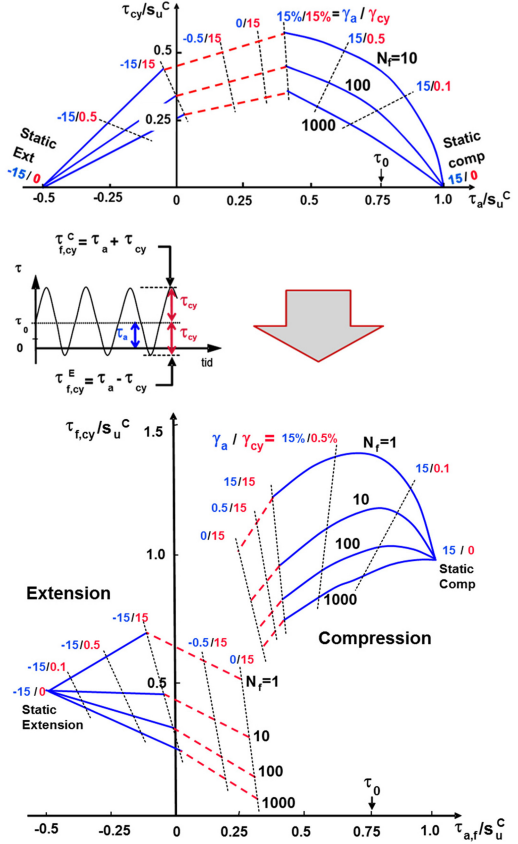

Figure 7.4. Cyclic triaxial compression and extension shear strengths. Normally consolidated Drammen Clay.
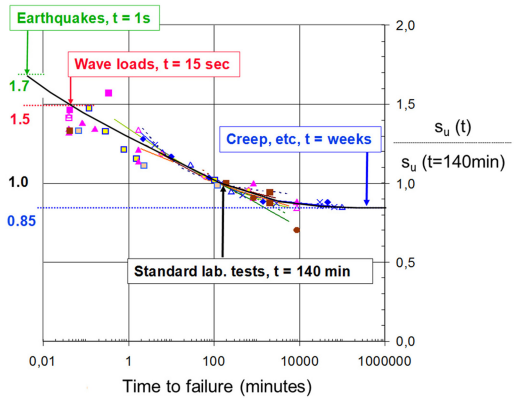
Figure 7.5. Monotonic undrained shear strength as a function of time to failure (based on Lunne & Andersen 2007).

7.3 *Shear strains as functions of average and cyclic shear stresses for constant number of cycles*

The average and cyclic shear strains are plotted and interpreted in the same type of diagrams as the number of cycles to failure. This is illustrated in Figure 7.6 where the upper figure shows the measured γ_a and

γ_{cy} in DSS tests with various combinations of τ_a and τ_{cy} after 10 cycles and the corresponding contours in the middle. The intersection of the γ_a-contours with the horizontal axis is defined by the monotonic test and the strain measured after application of $\Delta\tau_a$ in the cyclic tests. Contours for different values of number of cycles can be established in the same way. Diagrams for DSS and triaxial tests after 10 and 100 cycles are presented in Figures 7.6 and 7.7.

The contours can be used to establish stress strain curves for stress paths defined by given combinations of τ_a and τ_{cy} by reading out and plotting corresponding values of shear stresses and strains at the intersections between the stress paths and the contours in the contour diagrams, as illustrated in principle in Figure 12.34. Examples are presented in Section 13.6.

7.4 *Permanent shear strain*

As mentioned in Section 6.2, the permanent shear strain has often been assumed to be the same as the average shear strain. This can be a good approximation when there is no shear stress reversal (i.e. when $\tau_{cy} < |\tau_a|$). The difference is greater when the cyclic shear strain is predominant, but the difference between the permanent and the average shear strains will be less than the cyclic shear strain, i.e. $\gamma_p < \gamma_a \pm \gamma_{cy}$.

The relationship between permanent and average shear strains can be expressed as $\gamma_p = \gamma_a + x \cdot \gamma_{cy}$, where x is a parameter that varies between $+1$ and -1 and depends on the ratio between average and cyclic shear strains and whether the loading is DSS, triaxial compression or triaxial extension. $x = (\gamma_p - \gamma_a)/\gamma_{cy}$ is given as a function of γ_a/γ_{cy} for normally consolidated Drammen clay and sands with relative density of $D_r = 80\%$ to 100% in Figure 7.8.

The data in Figure 7.8 show that in the DSS tests, γ_p is typically $-0.25 \cdot \gamma_{cy}$ to $-0.5 \cdot \gamma_{cy}$ when $\gamma_a = 0$, within 30% of γ_a when $1 \leq \gamma_a/\gamma_{cy} \leq 2$, and essentially equal to γ_a for $\gamma_a/\gamma_{cy} \geq 4$.

In the triaxial tests, the difference between γ_p and γ_a will depend on the load direction, and the data in Figure 7.8 assumes that the cycle starts with loading in compression when $\gamma_a > 0$ and in extension when $\gamma_a < 0$. This can give a discontinuity in the curves for triaxial tests at $\gamma_a/\gamma_{cy} = 0$ in Figure 7.8. For triaxial compression tests on clay, the relation between γ_p and γ_a is the same as in the DSS tests. For triaxial compression tests on sand, γ_p is essentially the same as γ_a when $\gamma_a/\gamma_{cy} > 1$, but differs from γ_a when $\gamma_a/\gamma_{cy} < 1$. The data show a more scattered picture for the triaxial extension tests, and the tentative curves on the extension side are more uncertain.

7.5 *Shear strains as functions of cyclic shear stress and number of cycles for constant average shear stress*

The development of cyclic shear strain with number of cycles can be plotted as a function of cyclic shear stress for a given average shear stress as shown in Figure 7.9.
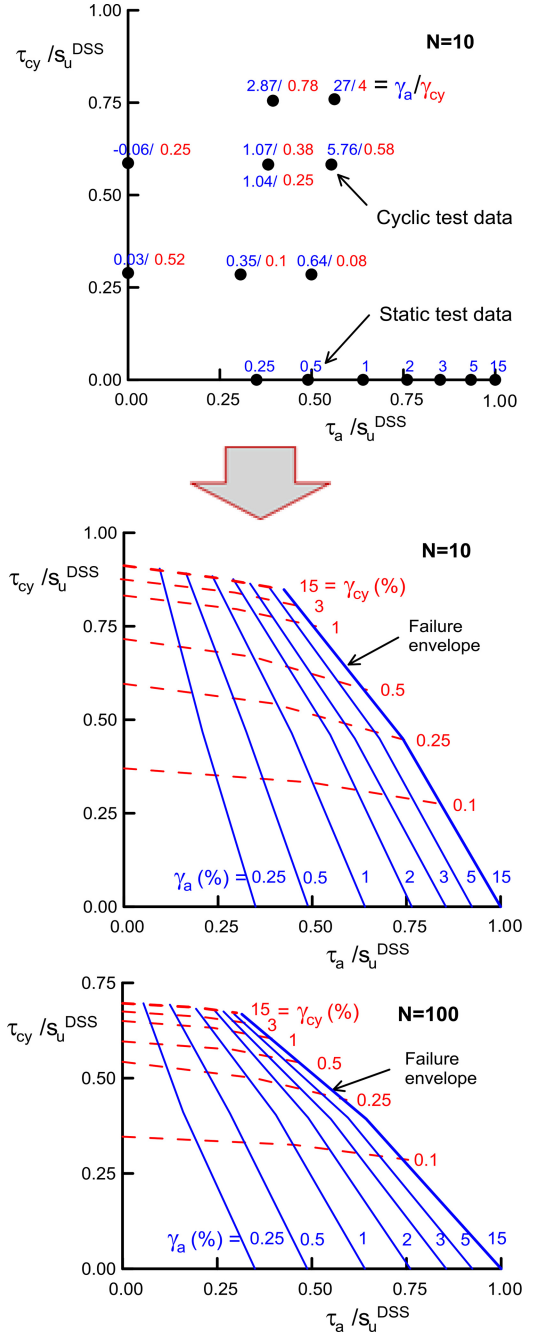

Figure 7.6. Construction of contour diagrams with average and cyclic shear strains after 10 cycles as functions of average and cyclic shear stresses (upper and middle diagrams), and diagram for $N = 100$ (lower diagram). DSS tests on normally consolidated Drammen Clay.

The contours in Figure 7.9 are valid for $\tau_a = 0$ and based on the data from the laboratory tests with $\tau_a = 0$ shown in the figure. Each horizontal line represents one cyclic test. The contours are consistent with the

Figure 7.7. Average and cyclic shear strains after 10 and 100 cycles as functions of average and cyclic shear stresses. Triaxial tests on normally consolidated Drammen Clay.

Figure 7.8. Relationship between permanent and average shear strains for normally consolidated Drammen clay and dense sand ($D_r \sim 80$ to 100%). Undrained loading. Upper: DSS. Lower: Triaxial.

Figure 7.9. Cyclic shear strain as a function of cyclic shear stress and number of cycles in DSS tests with $\tau_a = 0$ on normally consolidated Drammen Clay.

Figure 7.10. 3D representation of cyclic and average shear strains as functions of average and cyclic shear stresses and number of cycles. Normally consolidated Drammen Clay.

and not for $\tau_a = \tau_0$. For $\tau_a = 0$ in the triaxial tests there will be development of both cyclic and average shear strains, and both are shown in Figure 7.11.

7.6 Pore pressure

Pore pressure contour diagrams can be established in the same way as for shear strain. Normally only the permanent pore pressure component is needed. Examples of permanent pore pressure contour diagrams are presented in Figures 7.12 and 7.13. The pore pressure in the triaxial diagram is corrected for the change in total octahedral normal stress, $\Delta\sigma_{oct}$, to make it independent of whether the average shear stress is applied by increasing or decreasing the normal stress.

The failure envelopes in the diagrams are defined by the shear stresses that give large shear strains, as established in diagrams like those in Figures 7.1, 7.2, 7.6 and 7.7.

7.7 Damping

The stress-strain curves in Figures 6.4, 6.5 and 6.7 show that there is hysteretic damping within a cycle.

contours in Figures 7.6 and 7.7, i.e. the data for the contours in a section at $N = 10$ in Figure 7.9 are the same as the data in a section at $\tau_a = 0$ in the diagram for $N = 10$ in Figure 7.7. The relationship between the various diagrams in Figures 7.1, 7.7 and 7.9 is also illustrated in the 3D plot in Figure 7.10.

The equivalent to the type of diagram for DSS tests in Figure 7.9 is shown for triaxial tests in Figure 7.11. Note that the triaxial diagrams are shown for $\tau_a = 0$
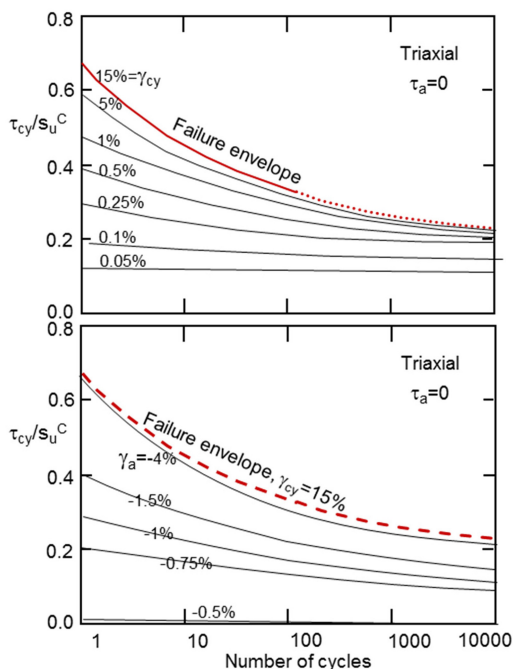
Figure 7.11. Cyclic (upper) and average (lower) shear strains as functions of cyclic shear stress and number of cycles in triaxial tests with $\tau_a = 0$ on normally consolidated Drammen Clay.

The damping should be plotted in contour diagrams like the other cyclic parameters, but this has not be done so far. Some further discussion of damping is given in Section 15.

7.8 *Important parameters*

The contour diagram examples presented earlier in this section are valid for normally consolidated clays with 10 s stress controlled undrained cyclic loading where $\Delta\tau_a$ is also applied undrained, and the shear stresses are normalized to the undrained static shear strength.

The cyclic response, and thus the contour diagrams, will depend on a number of factors, including:

– Relative density or water content
– Grain size distribution
– Plasticity index
– Overconsolidation ratio, OCR
– Sample preparation
– Consolidation time
– Load period
– Preshearing
– Strain-controlled vs. stress-controlled cycling
– Drained vs. undrained application of $\Delta\tau_a$
– Drainage within a cycle or cavitation

The influence of these factors on static and cyclic behavior is discussed in later sections by means of examples and correlations. Table 7.1 presents grain
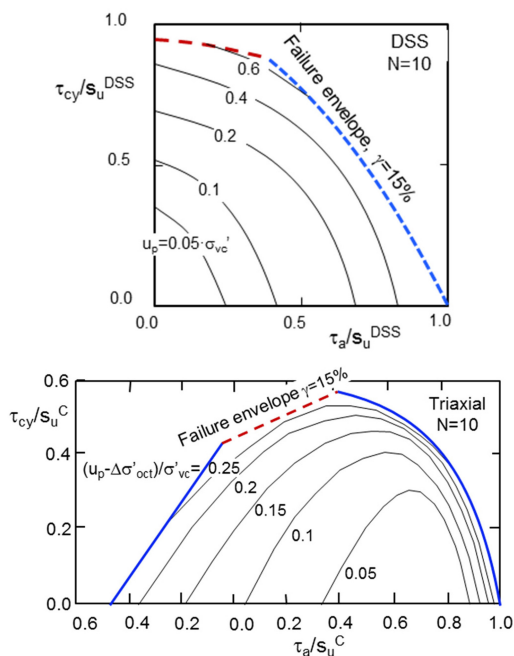
Figure 7.12. Permanent pore pressure as a function of cyclic and average shear stresses for 10 cycles in DSS (upper diagram) and triaxial (lower diagram) tests with $\tau_a = 0$ on normally consolidated Drammen Clay.

Table 7.1. Grain size characteristics (in mm) of sands and silts used in examples.

Soil	<0.002 (%)	<0.06 (%)	<2 (%)	D10	D60	method Prep.
Baskarp	0	3	100	0.075	0.15	Undercomp
Dogger Bank A	0	2	100	0.09	0.17	Undercomp
Dogger Bank B	2	20	100	0.017	0.16	Undercomp
Sand 1	0	1	100	0.094	0.2	Undercomp
Sand 3	0	1	100	0.15	0.22	Pluviation
Sand 26	0	0	100	0.15	0.21	Undercomp
Sand 31	7.5	30	100	0.016	0.074	Intact
Sand 34	0	0	100	0.34	0.6	Pluviation
Sand 52	3	11	100	0.049	0.197	Undercomp
Sand 54	15	45	100	<0.002	0.06	Intact
Toyoura	0	0	100	0.13	0.2	Pluviation
Clayey silt	10	45	100	0.002	0.07	Intact
Drammen clay	45–55		100	<0.002		Intact

size data for soils that are used as examples. The contours of strains and pore pressures for triaxial loading on Sand 3 are based on interpretation of triaxial tests performed by Dr. Kim Parsberg Jakobsen in connection with his Ph.D. research at Aalborg University, under supervision of Prof. Lars Bo Ibsen.

The cyclic response will also depend on the consolidation stresses, even after normalization to the
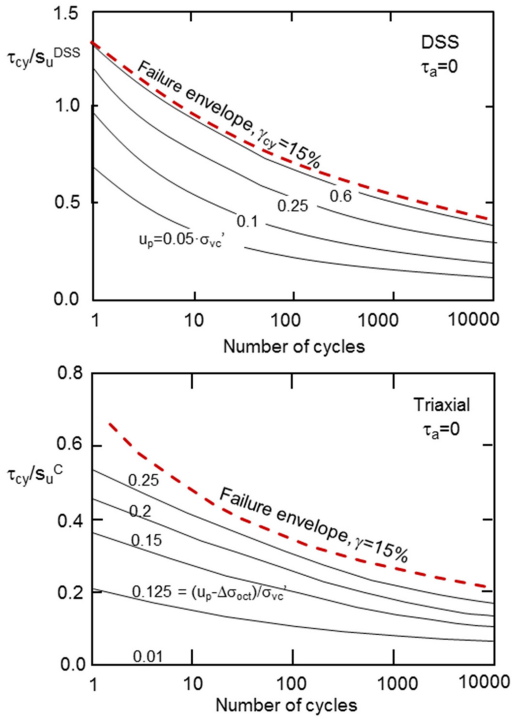
Figure 7.13. Permanent pore pressure as a function of cyclic shear stress and number of cycles in DSS (upper diagram) and triaxial (lower diagram) tests with $\tau_a = 0$ on normally consolidated Drammen Clay.

consolidation stress. This is also the case for the undrained static behavior. Both static and cyclic behavior is therefore in the subsequent sections normalized to a reference stress, defined as

$\sigma_{ref}' = p_a \cdot (\sigma_{vc}'/p_a)^n$, where

p_a is the atmospheric pressure (=100 kPa)
σ_{vc}' is the vertical effective consolidation stress
n is an empirical exponent determined by curve fitting to minimize the effect of consolidation stress.
    The curve fitting, presented later, gave the following values:

n = 0.1 to 0.9 for undrained static strength of sand and silt
n = 0.9 for undrained static strength of clay
n = 0.9 for cyclic shear strength of sand and silt

    However, the cyclic strength of clay can best be normalized to the static shear strength, as in the Drammen clay examples in the previous sections. This normalization has the advantage of being much less influenced by overconsolidation ratio, OCR, than normalization to effective stress (e.g. Andersen et al. 1988, Andersen & Lauritzsen 1988).
    For sand and silt, normalization of cyclic strength is best done to the reference stress, because n is different for static and cyclic strengths, and because the undrained shear strength is often less well defined, especially for dense, dilatant sand and silt.

    The reference stress is, as shown above, determined using the vertical effective consolidation stresses; i.e. the vertical effective stresses at the start of monotonic or cyclic loading. An alternative could have been normalization to the octahedral effective consolidation stress, but this would require assumptions about the horizontal stress in the DSS test, which is not known.
    Another alternative normalization might be normalization to the current effective stress; i.e. updating the effective stress for the change in pore pressure due to cyclic loading, but this is considered as an additional interpretation outside the scope of this paper.

7.9 Testing strategy

Plotting in contour diagrams permits interpolation between test results and reduces the number of tests required to establish a full picture of cyclic soil behavior. The number of tests required to establish the contour diagrams in a practical project depends on whether a complete set of diagrams is needed. For instance, one may need only DSS diagrams if the critical design situation is horizontal sliding at skirt tip level. The ambition level can also depend on the project stage (feasibility vs. detailed design) and the consequence of uncertainty in the cyclic soil parameters.
    The strategy is illustrated for failure envelope contours in Figure 7.14, but the considerations are valid for all the different contour diagrams in Section 7.
    The first step in a testing strategy would normally be to identify a set of contours for a soil similar to the one to be investigated and that covers the relevant parameters for the actual conditions. Contours for a number of different soils are presented later. Correlations that can be used to establish the contour diagrams are also presented in the following sections:

10. Static strength correlations
11. Monotonic stress-strain characteristics
12. Cyclic strength correlations
13. Cyclic stress-strain characteristics
14. Pore pressure

    One should then perform a set of monotonic triaxial compression, triaxial extension and DSS tests and a limited number of cyclic tests to see if the project specific soil data fit with these existing reference contours. The monotonic tests will define the intersections with the horizontal axis, and define the normalization parameter for clays. Three cyclic triaxial and three DSS tests numbered from 1 to 3 and distributed as shown in Figure 7.14 will tell whether the match with the existing contours is acceptable. If a reasonable match is not found, further cyclic testing needs to be performed until reliable contours can be defined. If the reference contour set needs to be significantly modified, a total of 5 triaxial and 5 DSS cyclic tests, as indicated in Figure 7.14, is probably a minimum. More tests may be needed if a new contour set must be established. Tests with both high and low cyclic shear stresses and different combinations of average and cyclic shear stresses
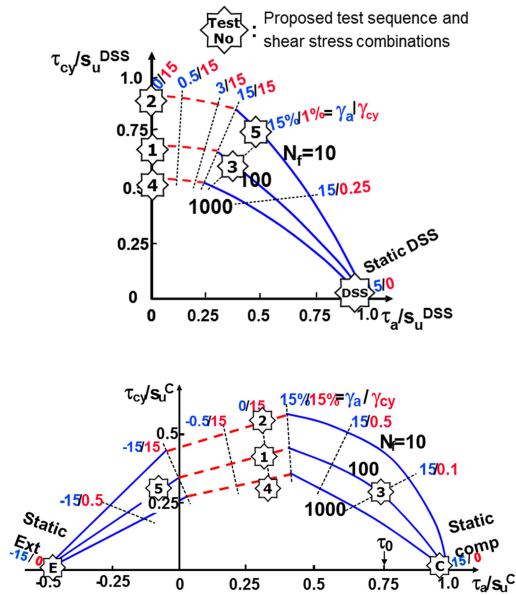
Figure 7.14. Strategy to establish cyclic contour diagrams.

should be included. If a complete set of both triaxial and DSS contours is not required, however, the testing can be limited to the contours that are important for design. The samples for both monotonic and cyclic tests must be from the same soil unit and as close to each other as possible to avoid scatter. Laboratory testing to establish the cyclic contour diagrams is discussed in more detail by Andersen et al. (2013).

8 CYCLIC SHEAR STRENGTH AND DEFORMATION PROPERTIES FOR A DESIGN STORM

8.1 *Design storm composition and cycle counting*

The contour diagrams are valid for stress-controlled loading with a constant cyclic shear stress. The cyclic design event normally consists of a load history where the cyclic load varies from one cycle to the next. In order to use contour diagrams as in Section 7, this irregular load history needs to be translated into a number of parcels with different constant cyclic loads. This section will describe how this can be achieved. In some cases there is also an average component from environmental loads in addition to the weight of the structure. The cyclic load history can also be from more than one source and with different frequencies, like simultaneous waves and wind for offshore wind turbines, and cases where the structure is set in motion at the natural frequency by the external forcing frequency.

It is impractical to use irregular load histories both in design calculations and in the laboratory. Finite element codes have been developed that can follow irregular time histories, as briefly summarized by Jardine et al. (2012) and Andersen et al. (2013).
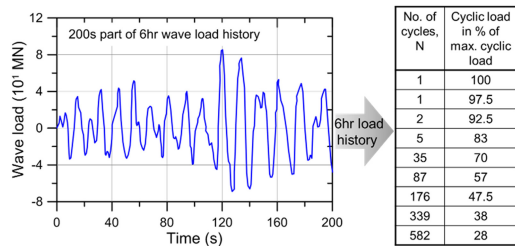
Figure 8.1. Transformation of cyclic load history to parcels.

However, such procedures become difficult for long duration load histories both for technical and practical reasons, as small errors within a cycle can accumulate and computational time and cost become high. In the laboratory it would increase the complexity and costs significantly. In practical design the irregular cyclic load history is therefore normally transformed into parcels of constant cyclic loads, as exemplified in Figure 8.1.

The parcels in Figure 8.1 are arranged in ascending order. Applying the loads in this order and with the maximum load at the end will cause maximum cyclic degradation prior to the maximum load and be conservative for capacity and maximum cyclic displacement. For soil stiffness in dynamic and fatigue analyses, however, a different order can be more critical. The stiffness for the smaller loads can be lower if they come after the maximum load than if they come before.

In fatigue analysis of structures the transformation into parcels has often been performed by the "rain flow" method (Matsuishi & Endo 1968, ASTM E1049-85). In the rain flow method, all peaks are identified and counted. However, the method allows amplitudes to be determined from local maxima and minima belonging to different cycles, and this can overestimate the amplitudes. An alternative method proposed by Noren-Cosgriff et al. (2015) transforms the irregular cyclic history into single frequency amplitudes with separation of average and cyclic components based on adjacent local maxima and minima. The method requires operator input and is more sensitive to operator judgement. Comparisons have shown that the two methods may give significant differences in cyclic shear strength.

The discretization in Figure 8.1 shows the composition of the cyclic load component. As one can see from the other sections, the cyclic shear strength and deformation characteristics depend strongly on the average load and how the average load varies with time. Information about the variation in average load is therefore crucial.

8.2 *Equivalent number of cycles N_{eq}*

In practical design, the effect of cyclic loading can be taken into account by determining the equivalent number of cycles of the maximum load, N_{eq}, that will give the same cyclic degradation as the actual irregular

20

cyclic load history. When N_{eq} is known, the contour diagrams can be used directly.

The determination of N_{eq} can be done by the pore pressure accumulation procedure or the strain accumulation procedure. As mentioned in Section 6.2, the pore pressure accumulation procedure is the preferred procedure in cases where there can be drainage during the cyclic load history, whereas the strain accumulation procedure may be more suited for clay.

8.2.1 *Pore pressure accumulation procedure.*
Undrained conditions

The pore pressure accumulation procedure assumes that the pore pressure at the start of a load cycle is equal to the pore pressure at the end of the previous cycle (e.g. Andersen 1981, Andersen et al. 1994, Jostad et al. 1997).

The simplified load history in Figure 8.1 is used as an example. In the table in Figure 8.2 the loads are scaled to shear stresses, assuming that the shear stresses are proportional to the loads. Different scaling factors are used, with maximum normalized cyclic shear stresses of $\tau_{cy,max}/\sigma'_{vc} = 0.10$, 0.15, 0.20 and 0.25. The pore pressure accumulation is performed in a pore pressure contour diagram established from laboratory tests as explained in Section 7. The detailed accumulation is shown in Figure 8.2 (middle) for the history with $\tau_{cy,max}/\sigma'_{vc} = 0.15$, with the loads in ascending order. The first parcel of 582 cycles with $\tau/\sigma'_{vc} = 0.042$ starts at Point A and ends at Point B after 582 cycles. The contours show that the permanent pore pressure in Point B is $u_p/\sigma'_{vc} = 0.02$. In the next parcel $\tau/\sigma'_{vc} = 0.057$, and since the soil remembers the pore pressure from the first parcel, it follows the contour for $u_p/\sigma'_{vc} = 0.02$ up to $\tau/\sigma'_{vc} = 0.057$, marked as Point C, where $N = 10$. It means that the effect of the first parcel is equivalent to applying 10 cycles at $\tau/\sigma'_{vc} = 0.057$. The 339 cycles in the second parcel is thus counted from Point C and the second parcels ends at 349 cycles in Point D. This procedure is repeated for all the parcels, and ends at $N = 21$ in the last parcel when $\tau/\sigma'_{vc} = 0.15$. These 21 cycles represent the number of cycles of the maximum shear stress that will be equivalent to applying the actual load history; i.e. $N_{eq} = 21$.

The accumulation is repeated for the histories scaled to $\tau_{cy,max}/\sigma'_{vc} = 0.10$ and 0.20. It can be seen that N_{eq} can vary with the scaling factor. A locus has been drawn between the end points for the different scaling factors. This locus is copied to the strain contour diagram in the lower part of Figure 8.2. The intersection between this locus and the failure envelope defines N_{eq} at failure to be 25 and the cyclic shear strength to be $\tau_{f,cy}/\sigma'_{vc} = 0.19$ in this case, representing a DSS test with symmetrical loading, i.e. $\tau_a = 0$.

The intersection between the locus and the different cyclic shear strain contours can be used to establish the relationship between cyclic shear stress and cyclic shear strain, as indicated in the lower part of Figure 8.2. The curve in Figure 8.2 represents the relationship

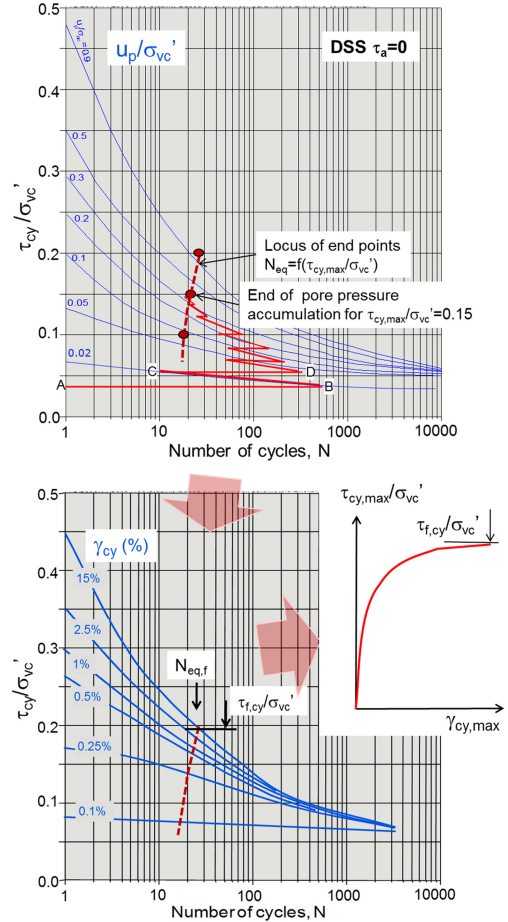| N	F/F$_{max}$	τ/σ_{vc}'	τ/σ_{vc}'	τ/σ_{vc}'	τ/σ_{vc}'
1	100	0.100	0.150	0.200	0.25
1	97.5	0.975	0.146	0.195	0.24
2	92.5	0.925	0.139	0.185	0.23
5	83	0.83	0.125	0.166	0.21
35	70	0.70	0.105	0.140	0.18
87	57	0.57	0.085	0.114	0.14
176	47.5	0.475	0.071	0.095	0.12
339	38	0.38	0.057	0.076	0.10
582	28	0.28	0.042	0.056	0.07

Figure 8.2. Pore pressure accumulation for undrained conditions and determination of cyclic shear strain.
Upper: Table with cyclic load composition.
Middle: Pore pressure accumulation. Undrained conditions.
Lower: Transfer of locus to shear strain contour diagram and determination of stress-strain relationship.

between cyclic shear stress and cyclic shear strain for the maximum load in the cyclic load history, and can be used as input to calculate the cyclic displacement during the maximum cyclic load.

The results can be used in a more general way by assuming that the N_{eq} determined for DSS tests with $\tau_a = 0$ is valid for all stress paths. With this assumption one can determine the cyclic shear strength for all stress paths and average shear stresses from diagrams of the types in Figures 7.3 and 7.4. The relationships between shear stresses and shear strains can be determined from diagrams of the types shown in Figures 7.9 and 7.11. More accurate determination of N_{eq} for $\tau_a \geq 0$ can be done by also performing the accumulation in contour diagrams for $\tau_a \neq 0$.

The assumption that the pore pressure at the start of a cycle is the same as the pore pressure at the end of the previous cycle may not be valid in all cases, such as in dense dilatant sand. The sand will tend to dilate when the cyclic shear stress is increased from $\tau_{cy,a}$ to $\tau_{cy,b}$ (Figure 8.3), introducing a negative change in the pore pressure, Δu_p. When the shear stresses before and after the change in cyclic shear stress are on the failure envelope, the change in pore pressure can be expressed as (Jostad et al. 1997):

$$\Delta u_p = (1 - \tau_{cy,b}/\tau_{cy,a}) \cdot (\sigma'_a - \tau_a/\tan\alpha')$$

The same correction should be made when the cyclic shear stress is decreased, i.e. $\tau_{cy,b} < \tau_{cy,a}$. Δu_p will then become positive.

If $\tau_{cy,a}$ (or $\tau_{cy,b}$) is not on the failure envelope, the stress path should be extrapolated to intersect the failure envelope and $\tau_{cy,a}$ (or $\tau_{cy,b}$) should be replaced by τ_{cy} at the intersection.

The correction in Figure 8.3 assumes that the slope of the unloading part of the effective stress paths of the first cycle with $\tau_{cy} = \tau_{cy,b}$ and the last cycle with $\tau_{cy} = \tau_{cy,a}$ are parallel and constant. The slope will change during a cycle, and the validity of the correction will depend on τ_a and how much the slope of the stress path changes when it crosses the τ_a line and returns. More detailed corrections including the effect of changes in slope of stress path are presented in Jostad et al. (2015).

Some effect of change in cyclic shear stress may also occur if neither $\tau_{cy,a}$ nor $\tau_{cy,b}$ reaches the failure envelope. It should therefore be considered whether a correction in the pore pressure should be introduced also when the cyclic shear stress is below the failure envelope.

An alternative to the correction proposed above would be to use a correction similar to what is done in the cyclic strain accumulation procedure described in Section 8.2.3, where $\Delta\gamma_{cy}$ is determined based on γ_{cy} vs τ_{cy} for N = 1. The use of the pore pressure for N = 1 to determine the correction could also be an alternative to the Δu_p-correction described above.

8.2.2 *Pore pressure accumulation procedure. Effect of drainage.*

The effect of drainage during the cyclic load history can be considered by determining the amount of drainage that occurs simultaneously with the pore pressure generation during each parcel, as illustrated in Figure 8.4 (Andersen et al. 1994). The pore pressure will be zero at the start of the storm (Point A).
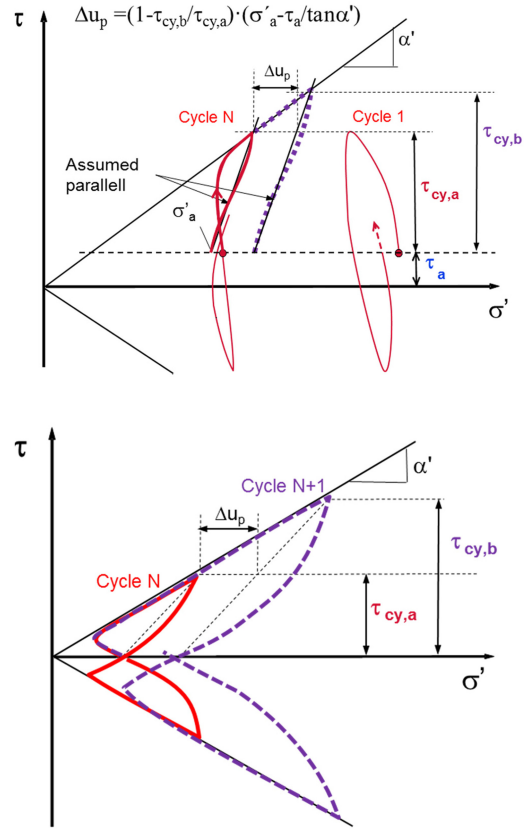

Figure 8.3. Change in u_p when cyclic shear stress is increased from $\tau_{cy,a}$ to $\tau_{cy,b}$ Upper: Principle. Lower: Stress paths from DSS test on dense sand with $\tau_a = 0$.

If the conditions are undrained, the pore pressure will increase to Point B during the first parcel and to Point D during the second parcel. If the conditions are not fully undrained, drainage will occur continuously during the storm. The pore pressure will then follow curve AC rather than AB during the first parcel. In the second parcel the soil will start in Point C and go to Point E if the conditions were undrained. The pore pressure that is generated during the second parcel will dissipate and take the pore pressure to curve CF. However, the pore pressure that remained after the first parcel (Point C) will also continue to dissipate, and the dissipation of this component will reduce the pore pressure further from Point F to Point G.

The pore pressure dissipation can be determined most rigorously in finite element consolidation analyses, but simplified analyses can be performed by means of simple diagrams, like the ones in Figures 8.6 and 8.7. Separate diagrams are given for pore pressure generated by a constant rate, C, and for dissipation with time for an initial pore pressure, u_0. Two boundary conditions are considered: one-dimensional flow and radial flow in a disk.

The example in Figure 8.5 illustrates how the pore pressure can be determined when drainage occurs.
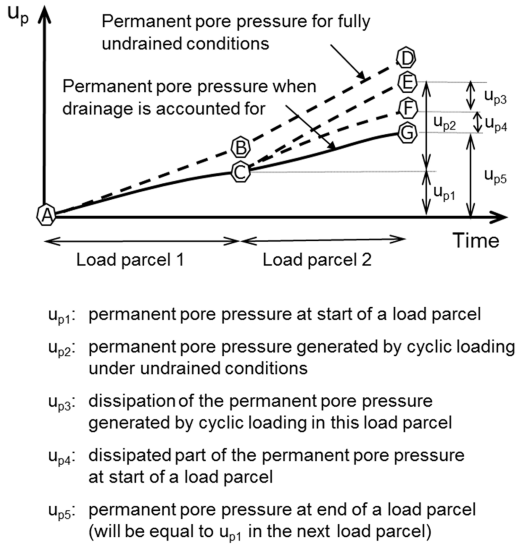
Figure 8.4. Pore pressure development in a storm under partly drained conditions.
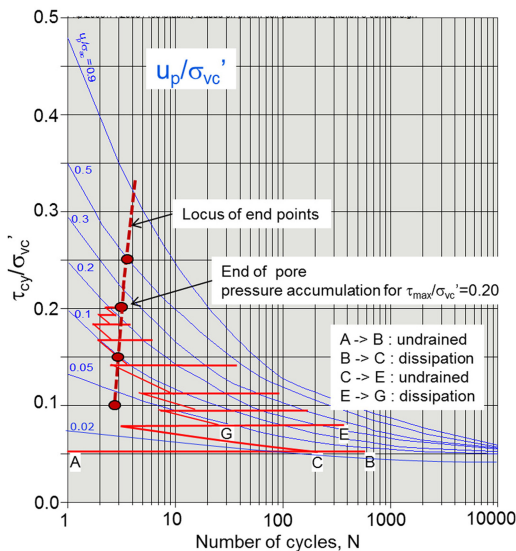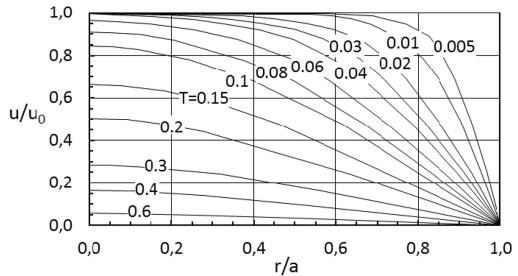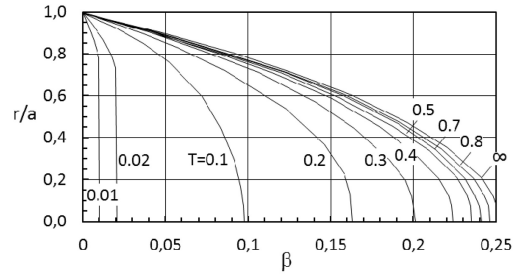
u_{p1}: permanent pore pressure at start of a load parcel

u_{p2}: permanent pore pressure generated by cyclic loading under undrained conditions

u_{p3}: dissipation of the permanent pore pressure generated by cyclic loading in this load parcel

u_{p4}: dissipated part of the permanent pore pressure at start of a load parcel

u_{p5}: permanent pore pressure at end of a load parcel (will be equal to u_{p1} in the next load parcel)

Figure 8.6. Dissipation of pore pressure in circular disk with radial drainage. Left: Pore pressure generated at constant rate (based on Heiberg 1973), Right: Initial pore pressure $u = u_0$ in entire volume at $t = 0$ (based on Madshus & Hårvik 1988).

$T = (k \cdot M / (\gamma_w \cdot a^2)) \cdot t$ $u = \beta \cdot (\gamma_w \cdot a^2 / (k \cdot M)) \cdot C$

C: rate of pore pressure generation

u_0: initial pore pressure

Figure 8.5. Example of pore pressure accumulation for partly drained conditions.

The example considers the same cyclic shear stress history as in the undrained case in Figure 8.2a, but shows the detailed accumulation for $\tau_{cy,max}/\sigma'_{vc} = 0.20$. In the first parcel, the soil ends up at Point B where $N = 582$ when there is no drainage. Interpolation between the contours shows that $u_p/\sigma'_{vc} = 0.025$ at this point. The drainage that takes place during this parcel can be determined as explained in connection with Figure 8.4. The drainage reduces the pore pressure to $u_p/\sigma'_{vc} = 0.025$ (Point C). Following the $u_p/\sigma'_{vc} = 0.025$ contour to the next stress level and adding the 339 cycles at this stress level brings the soil to Point E

before drainage and back to Point G after drainage. This procedure is repeated for all the parcels, and ends up with an equivalent number of cycles of $N_{eq} = 4$. Repetition with the parcels for the other scaling factors gives the locus of end points indicated in Figure 8.5. The equivalent number of cycles at failure is 4, compared to the 25 for undrained conditions.

If performing simplified dissipation analyses with the dissipation diagrams in Figures 8.6 and 8.7 one needs to exercise caution in cases with layering. If there are layers with different pore pressure generation and dissipation characteristics, pore pressure redistribution may occur between the layers. For sand, for instance, a looser layer will generate more pore pressure than a dense layer, and water from the looser layer can flow into the denser sand, increasing the pore water pressure in the denser sand. In some cases, this can reduce the shear strength of the denser sand considerably.

The dissipation analysis approach described above assumes fully undrained conditions within a cycle and that the pore pressure is generated with a constant rate within each parcel. The assumption of a constant rate may not be accurate in cases with small number of cycles in a parcel and significant pore pressure variation within a cycle. The procedure also becomes uncertain when the dilatancy in the first cycle is so strong that the pore pressure at the end of the cycle is negative, such as for high cyclic shear stresses in the lower pore pressure contour diagrams in Figure 14.1.
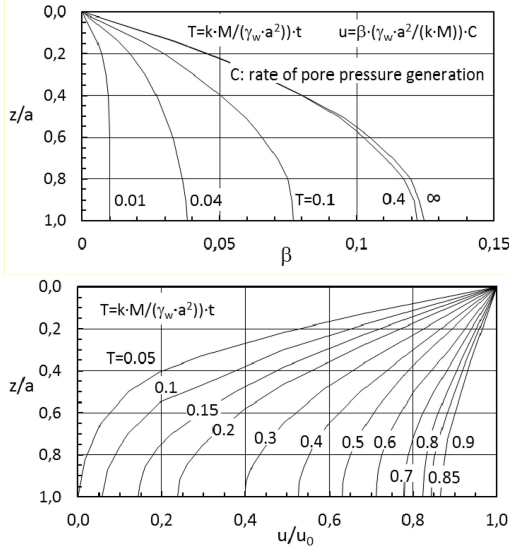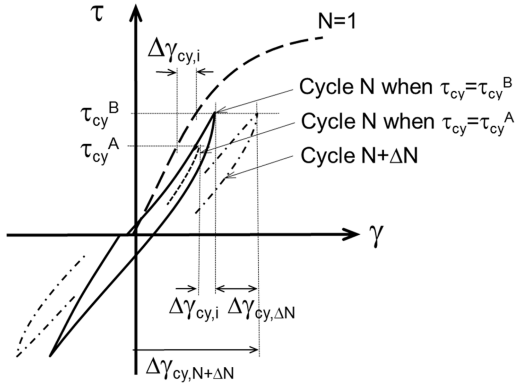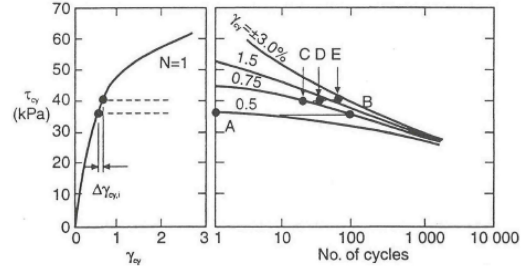
Figure 8.9. Principle for cyclic shear strain accumulation.

The behavior under varying cyclic shear stress is determined in a cyclic shear strain contour diagram as shown in Figure 8.9. The curve on the left is the relationship between cyclic shear stress and cyclic shear strain for the first load cycle (N = 1). This curve can be established from a vertical section at N = 1 in the contour diagram.

In the example in Figure 8.9 the soil element is first subjected to 100 cycles with $\tau_{cy}^A = 36$ kPa, taking the soil from point A to point B where the cyclic shear strain contours show that the cyclic shear strain is $\gamma_{cy} = 0.75\%$. τ_{cy} is then increased from 36 kPa to 41 kPa. The soil remembers the $\gamma_{cy} = 0.75\%$ it has experienced and follows the $\gamma_{cy} = 0.75\%$ contour to $\tau_{cy} = 41$ kPa (Point C). However, when the cyclic shear stress is increased, the cyclic shear strain will increase by $\Delta\gamma_{cy,i}$ as explained above, where $\Delta\gamma_{cy,i}$ is determined as the difference in cyclic shear strain for $\tau_{cy} = 41$ and 36 kPa from the curve for N = 1. The increase in cyclic shear strain due to the change in cyclic shear stress is approximately 0.1% and takes the soil to $\gamma_{cy} = 0.85\%$ at Point D where N = 35. This is the condition when cycling starts at $\tau_{cy}^B = 41$ kPa. The cyclic load history to this point is thus equivalent to 35 cycles at $\tau_{cy}^B = 41$ kPa. When 40 cycles are applied at $\tau_{cy}^B = 41$ kPa, the soil goes from N = 35 to N = 75 (Point E). In this manner the development of γ_{cy} during any cyclic load history can be predicted. The cyclic strain accumulation procedure cannot consider the effects of drainage.

The cyclic shear strain accumulation procedure can be applied in the same manner as the pore pressure accumulation procedure in order to scale a given load history to different maximum shear stresses and produce a locus of end points. This locus defines the equivalent number of cycles and can be used to determine cyclic shear strength and deformation characteristics, as explained in connection with the pore pressure accumulation procedure.

The cyclic shear strain accumulation procedure has been found to give good prediction of the behavior of laboratory tests with varying cyclic shear stresses when the cyclic shear stresses are in ascending order. The agreement has been somewhat less satisfactory when the cyclic shear stresses are reduced. An improvement may be achieved by using a stiffer $\Delta\gamma_{cy,i}$

Figure 8.7. Dissipation of pore pressure under one-dimensional conditions. Left: Pore pressure generated at constant rate (based on Heiberg 1973), Right: Initial pore pressure u = u₀ in entire volume at t = 0 (based on Lambe & Whitman 1969).

Figure 8.8. Cyclic stress-strain curves when cyclic shear stress is increased from τ_{cy}^A to τ_{cy}^B.

8.2.3 Cyclic strain accumulation procedure

The cyclic shear strain accumulation procedure (e.g. Andersen 1976) uses the cyclic shear strain as a memory to quantify the effect of cyclic loading. This procedure corrects for the change in cyclic shear strain that will occur when the cyclic shear stress is changed. This is illustrated by the stress-strain curves in Figure 8.8, which show that there will be an immediate increase in the cyclic shear strain of $\Delta\gamma_{cy,i}$ if the cyclic shear stress is increased from τ_{cy}^A to τ_{cy}^B. Based on empirical data from cyclic laboratory tests run with varying cyclic shear stresses it has, as an approximation been assumed that $\Delta\gamma_{cy,i}$ is independent of the cyclic shear stress history and that $\Delta\gamma_{cy,i}$ can be determined from the curve for cycle number one.
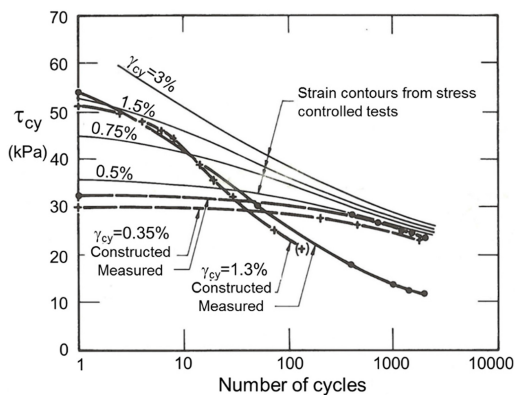
Figure 8.10. Results from strain-controlled cyclic tests plotted in diagram with strain contours from stress-controlled cyclic tests. DSS tests with $\tau_a = 0$ on Drammen Clay with OCR = 4 (Andersen et al. 1980).

when the cyclic shear stresses are reduced, corresponding to the initial shear modulus or following a Masing rule.

8.2.4 *Stress vs. strain controlled cyclic loading*

Stress-controlled testing is considered the best representation for cyclic events that are defined in terms of forces, such as for wave and wind loading, as shear stresses and forces can be directly correlated. In strain-controlled tests, neither the average nor the cyclic shear stresses can be controlled. The contour diagrams presented in Section 7 are all based on stress-controlled tests. In connection with earthquake loading, however, strain controlled testing has been more common.

It is important to be aware of the significant difference between stress and strain controlled cyclic tests. The difference is illustrated in Figure 8.10, where the results from two strain-controlled tests are plotted together with strain contours established from stress-controlled cyclic tests. The strain-controlled tests are run with a specified constant cyclic shear strain, and the cyclic shear stress required to maintain the specified cyclic shear strain is measured.

The strain-controlled test with a cyclic shear strain of $\gamma_{cy} = 1.3\%$ starts at the contour for $\gamma_{cy} = 1.3\%$ at N = 1, but the cyclic shear stress drops much faster than the strain contour from the stress-controlled test. The reason is that after a given number of cycles, N, the strain-controlled test has experienced N cycles with $\gamma_{cy} = 1.3\%$, whereas the stress-controlled test that exhibits $\gamma_{cy} = 1.3\%$ in cycle N has had smaller cyclic strains in all the previous cycles, and therefore a less severe cyclic load history.

The strain-controlled test with a cyclic shear strain of only $\gamma_{cy} = 0.35\%$ suffers less cyclic degradation than the test with $\gamma_{cy} = 1.3\%$ and is closer to the strain contour from the stress-controlled tests.

The strain-controlled tests have been predicted by the strain accumulation procedure described in Section 8.2.3. The predicted behavior is compared to the measured behavior in Figure 8.10, showing that the
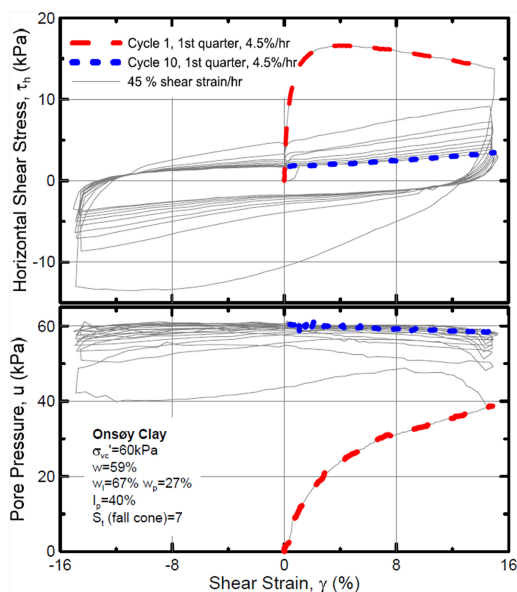
Figure 8.11. Strain-controlled undrained cyclic DSS test on p_0'-consolidated Onsøy Clay with 10 cycles of $\gamma_{cy} = 15\%$.

strain-controlled tests can be well predicted by the strain accumulation procedure. Details of how this can be done are presented in Andersen et al. (1978). This agreement gives confidence in the ability of the strain-accumulation procedure to predict the behavior in zones with high stress concentrations where the conditions may be closer to strain controlled.

The strain controlled tests in Figure 8.10 show that cyclic loading has the potential to degrade the soil more than one may believe based on strain contours from stress-controlled tests. However, the number of cycles to reach cyclic failure under stress-controlled conditions would be very high below a cyclic shear stress of 10 kPa. This asymptote is likely to correspond to the remolded strength. One example illustrating this further is given in Figure 8.11, which presents the result of a strain-controlled DSS test on p_0'-consolidated Onsøy Clay subjected to symmetrical cyclic loading at a cyclic shear strain of $\gamma_{cy} = 15\%$. The 1st quarter of cycles 1 and 10 are run with the conventional rate of loading for monotonic tests. The rest of the test is run with 10 times faster strain rate to speed up the testing time. A high pore pressure is generated in the first quarter cycle and soon a pore pressure equal to the consolidation stress is developed, corresponding to zero effective stress when the shear stress passes through zero. This is an important finding in connection with set-up calculations for skirted anchors and foundations (Andersen & Jostad 2002 & 2004). The shear stress required to give 15% shear strain drops with number of cycles, as seen from Figures 8.11 and 8.12. It seems that the shear stress will continue to decrease after 10 cycles and that it will asymptotically approach the remolded shear strength.
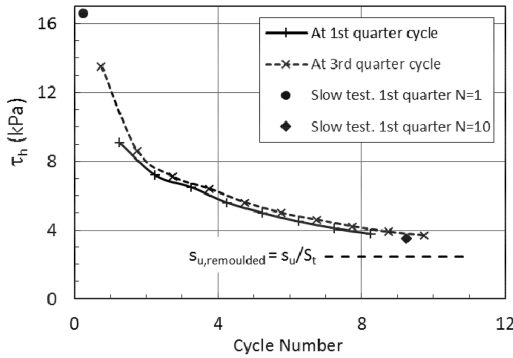
Figure 8.12. Maximum shear stress in 1st and 3rd quarter cycle as a function of number of cycles for the test in Figure 8.11.

The remolded shear strength in Figure 8.12 is determined as the shear strength in the 1st quarter cycle divided by the sensitivity from fall cone tests.

9 SAMPLE PREPARATION AND LABORATORY TESTING

The contour diagrams are established from monotonic and cyclic laboratory tests, and as for all laboratory testing it is important that the samples are representative for the in situ conditions. This requires careful soil sampling, sample preparation and consolidation.

9.1 *Sample preparation*

9.1.1 *Clay*

Sample disturbance and consolidation procedures are important for the quality of laboratory tests on clay. Consolidation of clay samples and possible ways to correct the static shear strength of clays for sample disturbance are discussed by Lunne et al. (2006), Berre et al. (2007) and Lunne et al. (2012).

Lunne et al. (2006) and Lunne & Andersen (2007) show that the static triaxial strength is more influenced by sample disturbance than static triaxial extension and DSS strengths, and this causes the anisotropy to decrease with increasing sample disturbance, as shown in Table 9.1.

The change in void ratio, $\Delta e/e_0$, has been used by Lunne et al. (2006) as a measure of sample disturbance. Δe is the change in void ratio for consolidation to the in situ effective stresses, and e_0 is the void ratio at start of consolidation. The shear strength as a function of $\Delta e/e_0$ is presented for soft, close to normally consolidated Luva clay in Figure 9.1. Luva clay has a plasticity index around $I_p = 35\%$. The strength depends on the depth, and curves for different depths are drawn based on the individual data points. Data from Onsøy clay which has approximately the same plasticity is included to help draw the curves. There is scatter in the data, but the curves still indicate that the compression strength increases and the extension

Table 9.1. Anisotropy ratios as functions of sample quality (based on Lunne & Andersen 2007).

Sample type	Block samples	54/95 mm diam. onshore	Offshore samples
s_u^C/s_u^{DSS}	1.45	1.35	1.25
s_u^E/s_u^{DSS}	0.61	0.68	0.78
s_u^E/s_u^C	0.42	0.50	0.62
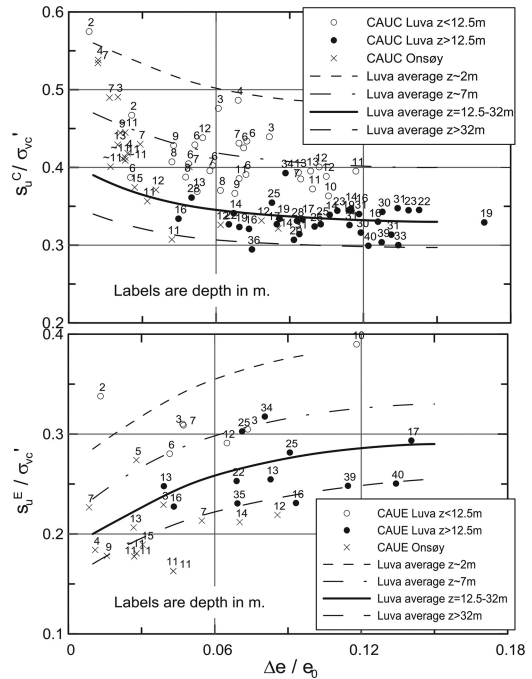
Figure 9.1. Compression (upper) and extension (lower) shear strengths as functions of $\Delta e/e_0$ (based on Lunne et al. 2012).

strength decreases with decreasing $\Delta e/e_0$. This trend is explained by the compression strength being governed by the soil structure, which is broken down by sample disturbance, whereas the extension strength is more governed by the water content, which is reduced by sample disturbance when the soil is reconsolidated to the in situ stresses. Calculating the anisotropy ratio from these curves gives values close to those in Table 9.1.

The anisotropy ratio is important for the construction of cyclic contour diagrams, since the left side intersection with the horizontal axis in the triaxial contours is defined by the anisotropy ratio s_u^E/s_u^C. The contour diagrams therefore depend on the sample quality, and it is important that one is aware of this when denormalizing the diagrams. One will overestimate the static and the cyclic shear strengths on the extension side if denormalizing is done by multiplying by a static

compression strength of higher quality than used to establish the diagram.

9.1.2 *Sand and silt*

It is difficult to obtain high quality samples of sand and silt that are representative of the in situ conditions. In cases where "intact" samples are very disturbed, the specimens are normally prepared by reconstituting the soil, but this may give samples that are not fully representative of the in situ conditions. Several authors have shown that the cyclic shear strength of sand and silt depends on the sample preparation method (e.g. Silver et al. 1976, Mulilis et al. 1977a, Vaid et al. 1999) and that reconstituted samples can give lower strength than "intact" samples (e.g. Mulilis et al. 1977a, Høeg et al. 2000). Andersen (2009) discusses this and, based on comparison with strength of samples taken by in situ frozen sampling technique, recommends to reconstitute sand samples by wet tamping or water deposition, unless the in situ soil has been deposited under dry conditions. If the silt content is high, however, reconstitution can be difficult, especially if the fines include clay. Use of "intact" samples may then be possible and preferable, even if such specimens will be disturbed. Whether the disturbance may give too high or too low cyclic strength will depend on the relative density. In particular, one should be aware that disturbed samples of silt and silty clay may experience a reduction in water content during reconsolidation that transforms the soil from contractive to dilative (e.g. Lunne et al. 2006, Berre et al. 2007). This can result in a significant overestimate of the shear strength.

The samples should be presheared if the soil is subjected to cyclic loading accompanied by drainage prior to and/or during the main design event. Intact samples, however, should not be presheared for cyclic loading that has occurred prior to sampling, as such preshearing is already reflected in their structure.

Preshearing involves cyclic loading accompanied by drainage during or after cyclic loading. The preshearing is normally applied after the specimen has been consolidated to the specified consolidation stresses, before starting the monotonic or cyclic loading. This is also the practice in cases with partial drainage during the cyclic event, even if the soil behavior may then change continuously during the cyclic event. The shear stress and number of cycles for preshearing should be determined with this behavior in mind. For large offshore gravity platforms on dense sand, preshearing has typically been estimated to 400 cycles at $\tau_{cy}/\sigma'_{vc} = 0.04$, as this level of loading is estimated to occur during the build-up period of the design storm or during previous smaller storms. In earthquake areas, the soil may have experienced smaller earthquakes during its history.

Modest preshearing will increase the cyclic shear strength and may also reduce the effect of the sample preparation method, but the effect on sample preparation method has not been systematically studied. Preshearing effects are discussed further in Section 12.6.

When reconstituting sand, it is necessary to decide what density the samples should be reconstituted to. The target density can be determined based on the estimated in situ relative density, D_r, or the in situ water content, w. Both are, however, difficult to estimate with high confidence in situ.

The in situ D_r is normally determined based on CPT-correlations, but there are uncertainties with these correlations, such as effect of sand type, fines content and preconsolidation (e.g. Kort et al. 2015). The boundary conditions and use of dry sand in the calibration chambers also add uncertainty. Based on existing CPT-correlations, the in situ D_r is significantly higher than 100% at several offshore sites. It is uncertain whether this is due to deficiency in the correlations or may be related to preshearing, ageing or other long term effects to the soil structure in situ that are not captured in conventional laboratory tests or in calibration chambers.

The in situ water content can be overestimated in dense sand and underestimated in loose sand due to volume changes in connection with the sampling process and loss of water before the water content can be measured.

In the laboratory, the water content is well defined and would be the preferred reference parameter. The relative density requires determination of maximum and minimum dry densities. These values are also uncertain as different standards recommend different procedures that can give significant differences, especially for the maximum density (e.g. Blaker et al. 2015). Most of the correlations for sand and silt in the following sections are given as functions of both relative density and water content after consolidation.

9.2 *Effect of consolidation time*

It has long been recognized that clay strength increases with time due to secondary compression in addition to consolidation. This also leads to an apparent preconsolidation stress (e.g. Bjerrum 1967).

The effect of secondary compression has not received the same attention for sand and silt, but a long term effect of consolidation time can also be seen for sand and silt samples, even for clean sand. One example of secondary compression during rest periods in oedometer tests on a very dense clean sand is shown in Figure 16.1.

Examples of effect of time on cyclic shear strength are summarized in Figure 9.2. Tatsuoka et al. 1986a found that the cyclic strength in isotropically consolidated triaxial tests on air pluviated Toyoura sand with no fines increased by 15–20% after 68 days, for relative densities of both 50 and 80%. Tatsuoka et al. (1988) found that the cyclic shear strength of isotropically consolidated triaxial tests on water-vibrated Sengenyama Sand with 2.4% fines and $D_r = 80\%$ increased by about 25% after 64 hours and 40% after 68 days. Mulilis et al. (1977b) found that the cyclic strength of isotropically consolidated triaxial tests on air pluviated Monterey No. 0 sand with no fines
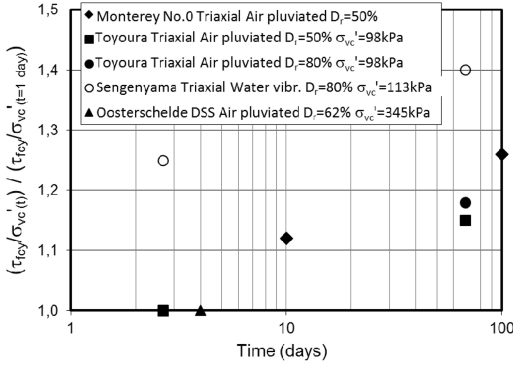
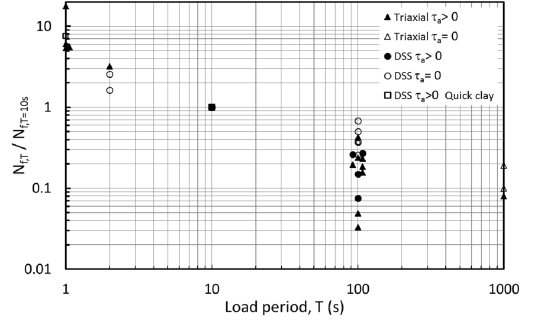Figure 9.2. Increase in cyclic shear strength as a function of consolidation time.

Figure 9.3. Ratio between number of cycles to failure with 1, 100 and 1000 s load period and number of cycles to failure with 10 s load period for given cyclic and average shear stresses. Various clays.

at $D_r = 50\%$ was essentially the same after 20 minutes and one day consolidation, whereas it increased by 12% and 26% after 10 and 100 days consolidation time, respectively. The volume change was small, however. The cyclic strength in DSS tests at NGI on air pluviated Oosterschelde Sand with no fines and $D_r = 62\%$, however, gave the same cyclic shear strength after 16 hours and 4 days consolidation.

Mitchell (2004) summarizes research on the effect of time on the initial shear modulus, G_{max}. He refers to the formula $G_{max,t} = G_{t,1000} \cdot (1 + N_G \cdot \log(t/t_{1000}))$ (Anderson & Stokoe 1978), expressing the shear modulus with time as a function of the shear modulus at a reference time of 1000 minutes and a coefficient N_G. Mesri et al. (1990) report that N_G for sands varies between 0.01 and 0.03 and increases as the soil becomes finer. Jamiolkowski & Manassero (1995) give values of 0.01 to 0.03 for silica sands, 0.039 for sand with 50% mica and 0.05–0.12 for carbonate sand. N_G of 0.01 and 0.03 gives an increase in G_{max} of between 2 and 6% after 100 days. This increase in G_{max} with time confirms the effect of time on sand behavior, but the increase in G_{max} is smaller than the data for cyclic shear strength in Figure 9.2.

For conventional projects it may be impractical to reproduce the long term effect in the laboratory, but the final consolidation stress should act overnight. The effect of longer consolidation time must be evaluated by judgement, including the experience referenced above. The examples above are for reconstituted samples with no preshearing. One should be aware that the effect is likely to be less on intact samples and on samples with preshearing. One should also keep in mind that samples can lose this ageing effect if they are consolidated above their apparent preconsolidation pressure.

9.3 Load period

The results presented in this paper are from tests with 10 s load period, unless specifically stated. 10 s is typical for wave loading. For other types of loading, the load period can go from less than 1 s to much longer than 10 s, as mentioned in Section 3.

The effect of load period on number of cycles to failure for clay is summarized in Figure 9.3. The figure contains triaxial and DSS data from clay with plasticity indeces in the range $I_p = 33$ to 90%, including triaxial tests on Onsøy clay with $I_p = 33\%$ (Wichtman et al. 2013), triaxial tests on Wenzhou clay with $I_p = 36\%$ (Li et al. 2011) and DSS tests on a quick clay with $I_p = 11\%$ and a sensitivity of $S_t > 75$. The figure shows the ratio between number of cycles to failure for a given load period, T, and number of cycles to failure for $T = 10$ s, $N_{f,T}/N_{f,T=10\,s}$. There is scatter in the data, but the ratio decreases with increasing load period. For instance, the number of cycles to failure for a 1s period will be about 8 times the number of cycles to failure for 10 s, and the number of cycles to failure for a 100 s period will be 0.03 to 0.8 times the number of cycles to failure for 10 s, i.e. 1.5 to 30 10 s cycles will be equivalent to one 100 s cycle. The effect of load period is smaller for symmetrical cyclic loading ($\tau_a = 0$) than for $|\tau_a| > 0$, and there is no clear difference between DSS and triaxial tests. Although it is not shown in the figure, no clear effect of plasticity was found for the plasticity range covered. This is in agreement with the findings for static shear strength (Lunne & Andersen 2007).

Cyclic tests on sand seem to indicate no significant effect of load period in triaxial and DSS tests in the range 0.25 to 60 s (Lee & Vernese 1978) and in triaxial tests in the range 1 to 20 s (Tatsuoka et al. 1986a).

No systematic data has been found for silt, but it seems reasonable to expect an effect somewhere between that for clay and sand, depending on the grain size distribution.

10 STATIC STRENGTH CORRELATIONS

As mentioned in Sections 5.2 and 7.9, monotonic test data is required to construct the cyclic contour diagrams in order to define the intersections of the contours with the horizontal axis. Monotonic data also provide a useful reference for the cyclic soil parameters, and the static shear strength is used to normalize
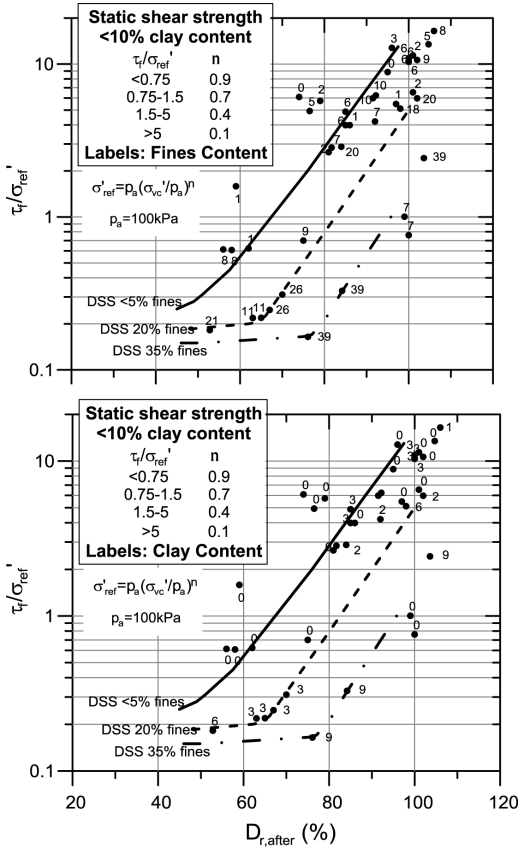
Figure 10.1. Static shear strength in DSS tests on normally consolidated sand and silt (<10% clay content) as a function of relative density after consolidation. Upper: Data points indicate fines content. Lower: Data points indicate clay content.
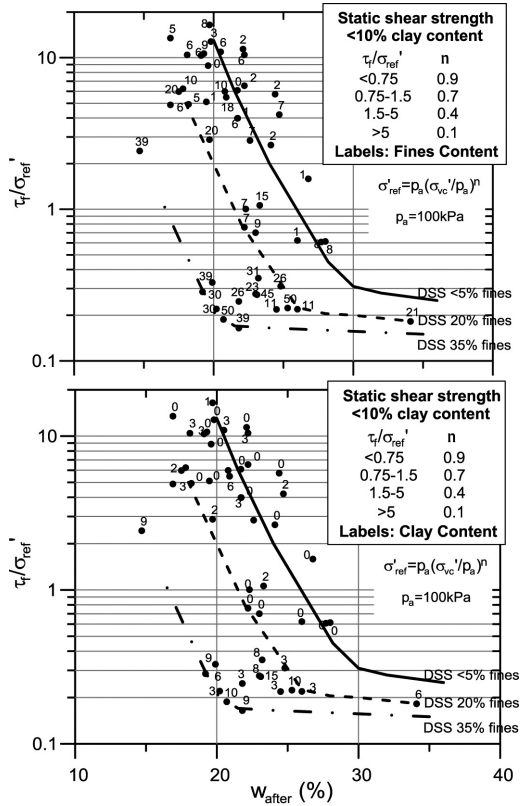
Figure 10.2. Static shear strength in DSS tests on normally consolidated sand and silt (<10% clay content) as a function of water content after consolidation. Upper: Data points indicate fines content. Lower: Data points indicate clay content.

the cyclic parameters for clays. Monotonic parameters can also be needed if the cyclic load history or the drainage conditions are such that there is little pore pressure generation prior to or during the maximum wave.

This section first presents correlations for the undrained static strength of normally consolidated soils, starting with silt and sand and followed by clays. Thereafter, correlations for the effect of overconsolidation are presented. Drained strength parameters for silt and sand are given in the last subsection.

10.1 Static DSS strength of NC sand and silt

The undrained static shear strength of normally consolidated sand and silt is presented as a function of relative density in Figure 10.1 and as a function of water content in Figure 10.2. The relative density and the water content are the values after consolidation. The use of relative density or water content as the correlation parameter is discussed in Section 9.1.2. One should be cautious about using Figure 10.1 when the fines content exceeds 15%.

The tests have been run on normally consolidated samples that are either "intact" or prepared by moist reconstitution. In cases with "intact" samples, the specimens are loaded so far above the in situ stresses that they experience volumetric strains that break down any in situ preconsolidation effect. The data contains soils with clay content less than 10%.

The shear strength, τ_f, has been defined as the peak shear stress for cases with strain softening. The shear stress at a large shear strain is given where no clear peak is observed. Large shear strain has generally been defined as a shear strain of 15%, but some of the tests with very high density dilated strongly and did not reach 15% shear strain. The shear strength was in these cases defined as the shear stress at a shear strain of 5 or 7.5%. These shear strengths are all very high, and the deviation from the general failure criterion is not believed to be of practical consequence.

The shear strength will depend on the vertical effective consolidation stress, σ'_{vc}, but the ratio τ_f/σ'_{vc} will increase with decreasing σ'_{vc}. The shear strength in Figures 10.1 and 10.2 is therefore normalized to a reference stress $\sigma'_{ref} = p_a \cdot (\sigma'_{vc}/p_a)^n$, as defined in Section 7.8. Different values of n were evaluated. The best fit

with the data was found when varying n between 0.1 and 0.9 as indicated in Figures 10.1 and 10.2. The data include tests with vertical consolidation stress in the range of $\sigma'_{vc} = 5$ to 800 kPa, but most of the data are in the range of $\sigma'_{vc} = 150$ to 400 kPa. The figures are thus less reliable outside this range.

The number above each data point is the fines content (upper diagrams) and the clay content (lower diagrams). The fines content varies from 0% (clean sand) to 50%. The clay content varies from 0% to 9%.

The data in Figures 10.1a and 10.2a show that the undrained static shear strength decreases with increasing fines content. Estimated curves for fines content less than 5% and fines content of 20% and 35% are included in the figures. This effect of fines content is in agreement with the effect of fines content reported by Yang et al. (2005) and Papadopoulou & Tika (2008). They found that the cyclic shear strength in isotropically consolidated triaxial tests at constant water content and consolidation stress decreased when the fines content increased from 0% to about 35%. When the fines content increased beyond about 35%, the strength increased again. The curve for 35% fines content is thus expected to represent a lower limit.

Half of the samples were not presheared. The other half were presheared with 250 to 400 cycles at a cyclic shear stress of $\tau_{cy}/\sigma'_{vc} = 0.04$ to 0.15. The curves are valid for tests with moderate preshearing with 400 cycles at a cyclic shear stress of $\tau_{cy}/\sigma'_{vc} = 0.04$ or less.

Hight & Leroueil (2003) presented data indicating that silt will have increased tendency for dilation with increasing sand content and decreasing clay content. For the tests included in this study, there is some correlation between silt and clay content, and it can be seen from Figure 10.1b and 10.2b that the curves for <5%, 20% and 35% fines content would be consistent with curves with clay content of about 0, 3 and 9%.

One data point for soil with 20% fines content gives a higher normalized strength than the rest of the data when plotted against relative density. This may be related to uncertainty in the determination of the relative density for soil with higher fines content. The data for this soil agrees better with the rest of the data when plotted versus water content.

Figure 10.3 shows results from tests with fines content higher than 35% plotted together with the recommended curves in Figure 10.2. Figure 10.3b shows that the clay content is higher than 10% for these tests. The shear strength for these soils is generally higher than that for 35% fines and is relatively independent of water content. The shear strength of soils with fines content greater than 35% should rather be determined based on the plasticity index, as discussed in Section 10.3.

10.2 Static shear strength anisotropy, sand and silt

The undrained shear strength of triaxial compression and extension tests are plotted together with the DSS shear strength in Figure 10.4a, as functions of both
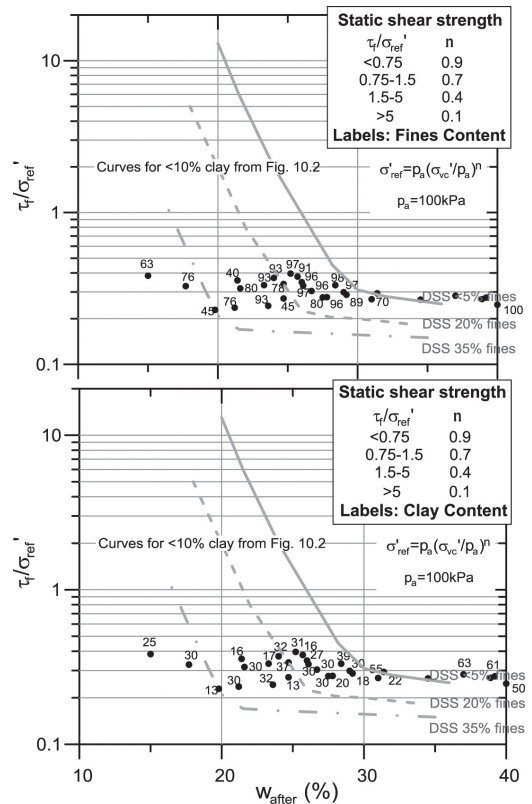
Figure 10.3. Static shear strength in DSS tests on normally consolidated soil as a function of water content after consolidation. Soils with more than 35% fines content. Curves for <10% clay included for reference. Upper: Data points indicate fines content. Lower: Data points indicate clay content.

relative density and water content. There are more data relating to water content than to relative density, because relative density was not measured on the soil with higher fines content. When looking at the diagrams one should compare the results of tests with similar fines content. Some of the very dense sands could not be brought to 15% shear strain due to limitations in the equipment, and for very dense sands the shear strength has been taken as the shear strength at 5% shear strain.

The plots show that the triaxial compression strength is significantly higher than the DSS strength for tests with the same fines content. The ratio between triaxial compression and DSS strengths varies, but is typically about 5, which is much higher than for clays.

There are fewer data for triaxial extension strength, but the values seem to be about the same as, or slightly higher than, the DSS strength. This conclusion seems more consistent for water content than for relative density.

The triaxial data in the diagrams are for relatively high relative densities and low water contents, and
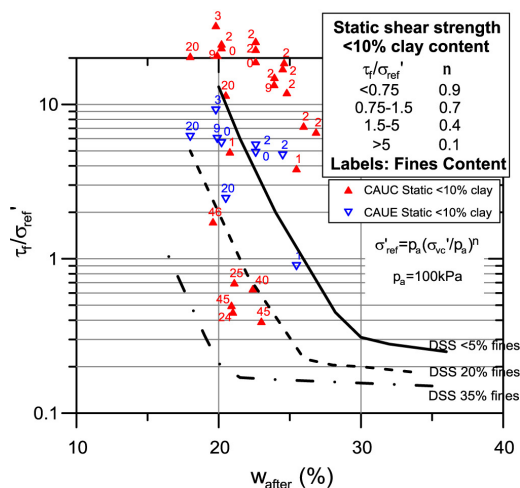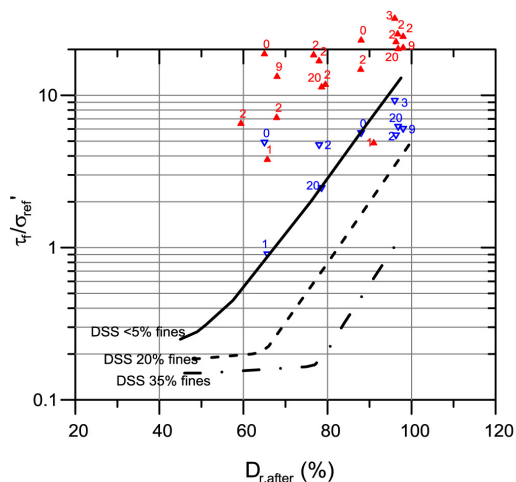
Figure 10.4a. Static shear strength in triaxial compression, DSS and triaxial extension tests on normally consolidated sand and silt (<10% clay content). Upper: Function of D_r. Lower: Function of water content.
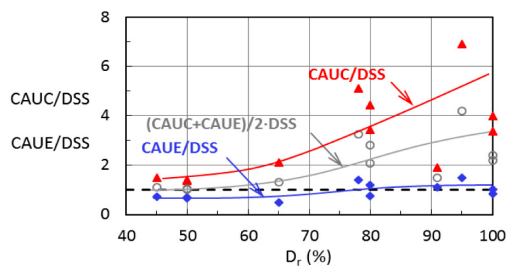

Figure 10.4b. Undrained static shear strength anisotropy. Sand and silty sand.

Table 10.1. Undrained static shear strength anisotropy. Sand, silty sand and Drammen clay.

Sand	D_r %	w %	γ_f %	s_u/σ_{vc}' DSS	C	E	C/DSS	E/DSS
Baskarp 1) No fines	95	19.8	5	1.6	11	2.4	6.9	1.5
Dogger Bank 2) No fines	100	22.3	5	3.5	>10	2.9	>2.85	0.83
Dogger Bank 2) No fines	78	24.4	5	1.75	9	2.5	5.1	1.4
Dogger Bank 2) OCR = 4 No fines	80	24.3	5	2.7	12	3.25	4.44	1.2
Dogger Bank 2) 20% silt	100	17.7	5	3.2	10.8	3.3	3.38	1.03
Dogger Bank 2) 20% silt	80	20	5	1.9	6.5	1.4	3.42	0.74
Sand 3	91	20.8	5	1.45	2.8	1.55	1.9	1.1
Sand 3	65	25.5	10	1.35	2.87	0.68	2.1	0.5
Clayey silt 10%<0.002 45%<0.06	–	21.5	15	0.34	0.46	0.22	1.4	0.7
Clayey silt OCR~6 10%<0.002 45%<0.06	–	24.5	15	0.57	0.77	0.40	1.38	0.67
Drammen clay	–	–	15	0.22	0.33	0.16	1.5	0.72

1) Andersen & Berre (1999); 2) Blaker & Andersen (2015)

the anisotropy ratios may decrease with decreasing relative density and increasing water content.

Sets of DSS, triaxial compression and triaxial extension tests are available for Baskarp sand, Dogger Bank sand and Sand 3. The anisotropy ratios for these soils types are given in Table 10.1 and plotted in Figure 10.4b. Results for Sand 3 are more uncertain than the others, as the DSS and triaxial tests are not at exactly the same density, and interpolation of strengths was necessary. Sample preparation was also different for Sand 3, with moist tamping of DSS and pluviation of triaxial samples. In order to have comparable data, the shear strengths were taken as the shear stress at 5% shear strain, apart from the lower density Sand 3 where a failure shear strain of 10% was used. The anisotropy ratios for these sands confirm the anisotropy ratios estimated from Figure 10.4 with the ratio for compression and DSS varying between 2 and 7, and for extension and DSS between 0.5 and 1.5. The average

ratios for Baskarp sand ($D_r = 95\%$) and the Dogger Bank sand with no fines ($D_r = 100\%$ and 78%) are >5 between compression and DSS and 1.2 between extension and DSS. The lower ratios were found for Sand 3. One should keep in mind that the ratios for Sand 3 may be less representative, as mentioned above.

Strength anisotropy of clay is discussed in Section 9.1.1, but data for a clayey silt and Drammen clay are included in Table 10.1 in order to link the anisotropy ratios for sand and silt to anisotropy ratios for clay. The data show that the anisotropy ratios are lower for clayey soils and that the DSS strength becomes closer
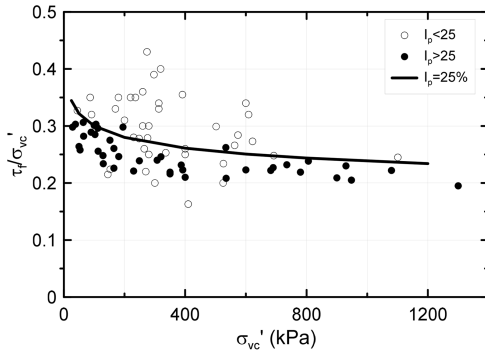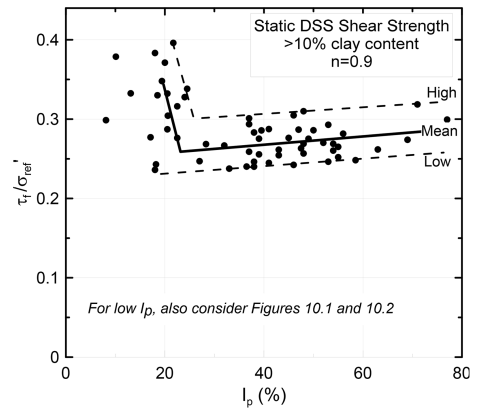
Figure 10.5. Static shear strength in DSS tests on normally consolidated clay (>10% clay content) as a function of consolidation stress.

10.3 Static DSS strength of NC clay

The undrained static DSS shear strength of normally consolidated clays from 81 tests on clays from 10 different locations with plasticity index varying from 3% to 77% is plotted as a function of consolidation stress in Figure 10.5. Normally consolidated specimens were produced by consolidating the specimens above the in situ preconsolidation stress.

The plots indicate that the normalized undrained DSS shear strength tends to decrease with increasing consolidation stress and increasing plasticity. The curve fitted for a plasticity index of $I_p = 25$ assumes that the shear strength ratio τ_f/σ'_{vc} is inversely proportional to σ'^n_{vc}, where n = 0.9. The exponent n = 0.9 indicates a smaller effect of σ'_{vc} than for sand and silt, where n = 0.5 was found to give the best fit with the data.

Quiros et al. (2000) also plotted the static shear strength from normally consolidated DSS tests as a function of consolidation stress. Their data included 172 tests on clays with plasticity index between $I_p = 14\%$ and 101%. Their average curve corresponds to an exponent of n = 0.9, as the curve in Figure 10.5. They did not find a clear effect of I_p, however, and their average curve was about 12% lower than the curve for $I_p = 25\%$ in Figure 10.5.

The data in Figure 10.5 are replotted in Figure 10.6, presenting the shear strength normalized to the reference stress, $\sigma'_{ref} = p_a \cdot (\sigma'_{vc}/p_a)^n$ with n = 0.9, as a function of the plasticity index, I_p. The plot shows that the normalized static shear strength increases somewhat with increasing plasticity index for a plasticity index above $I_p = 20$ to 22%. For a plasticity index below $I_p = 20$ to 22%, however, the normalized shear strength increases significantly with decreasing plasticity index. The increase in normalized strength with decreasing plasticity has some similarity with the DSS

Figure 10.6. Static shear strength in DSS tests on normally consolidated clay (>10% clay content) as a function of plasticity index.

failure envelope inclination (Figure 10.11), the initial shear modulus (Figure 11.5) and reloading constrained modulus (Figure 16.4).

At low plasticity indexes (e.g. $I_p < 15\%$), one should also consider the correlations for sand and silt (Figures 10.1 and 10.2).

10.4 Static shear strength anisotropy, clay

The shear strength anisotropy for clays depends on the degree of sample disturbance. Anisotropy factors are presented and discussed in Section 9.1.1.

10.5 Effect of OCR on static strength

The shear strength will depend on whether the soil has experienced higher effective stresses than the present ones. Ladd & Foot (1974) expressed the effect of preconsolidation in the equation

$$s_u/\sigma_{vc}' = (s_u/\sigma_{vc}')_{NC} \cdot OCR^m$$

where this expression is valid for clay where the preconsolidation is due to a previous overburden. The effect of overconsolidation ratio on the undrained triaxial compression, DSS and extension static shear strengths of Drammen Clay presented in Andersen (2004) is reasonably consistent with $(s_u/\sigma_{vc}')_{NC} = 0.33$, 0.21 and 0.16 and m = 0.79, 0.83 and 0.88 for triaxial compression, DSS and triaxial extension, respectively.

Figure 10.7 shows the ratio between shear strength of overconsolidated and normally consolidated soils as a function of OCR for 4 different soils. Drammen clay is included with the label "plastic clay". The effect of OCR on the static shear strength differs considerably for the four soils. The effect of OCR is significantly smaller for the very dense sand than for plastic clay. The reason is believed to be that very dense sand tends to dilate even when it is in a normally consolidated state, and the undrained shear strength is governed by the increased effective stresses induced by the negative
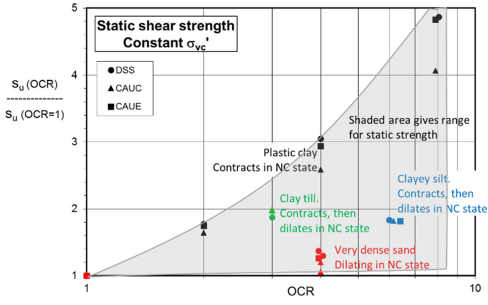
Figure 10.7. Undrained static shear strengths as a function of OCR.
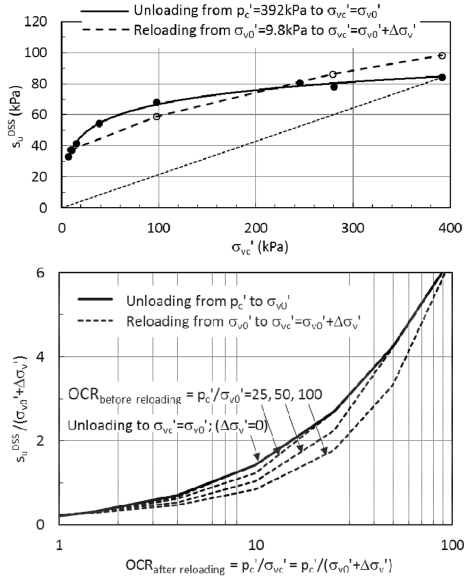

Figure 10.8. Undrained static DSS shear strength of Drammen clay as a function of OCR. Effect of reloading from lower effective stress. Upper: Data for $p'_c = 392$ kPa. Lower: Estimated general behavior.
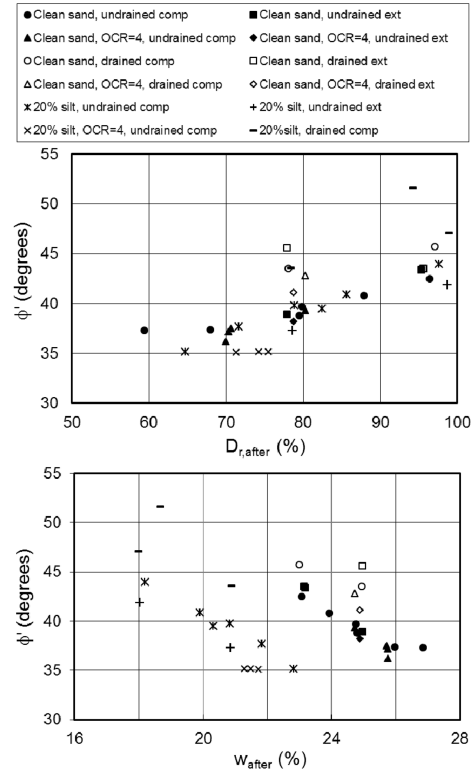

Figure 10.9. Friction angles for Dogger Bank sand for sand with no fines and with 20% fines as a function of D_r (upper) and w (lower).

shear induced pore pressure, rather than by the initial effective stresses. Plastic clays will be contractive in their normally consolidated state, becoming dilative as the overconsolidation increases. Soils that are contractive in their normally consolidated state, like most clays, loose sands and loose silts will thus be more influenced by OCR than dense sand and silt that are dilatant already in the normally consolidated state. Intermediate soils with dilatant behavior between clay and dense sand plot in between. The dilatant behavior of sand and silt, and thus the effect of OCR, also depends on the effective stresses in the normally consolidated state. The effect of consolidation stress is less pronounced for clays.

Figure 10.7 is valid for the case where the variation in OCR is generated by varying the preconsolidation stress, whilst keeping the consolidation stress the same. Because of the non-linearity in $s_u/\sigma'_{vc} = f(\sigma'_{vc})$, the effect of OCR on s_u/σ'_{vc} will be different if OCR is

generated by keeping the preconsolidation stress constant, whilst varying the consolidation stress. To go from a constant consolidation stress to a constant preconsolidation stress, the vertical axis in Figure 10.7 shall be multiplied with OCR^{n-1}, where $n = 0.5$ for sand and 0.9 for clay, as determined for static shear strength in Sections 10.1 and 10.3, respectively.

For Drammen clay the anisotropy ratio s_u^C/s_u^{DSS} decreases from 1.57 to 1.44 and s_u^E/s_u^{DSS} increases from 0.76 to 0.85 as OCR increases from 1 to 10. The data in Table 10.1 also show that the effect of OCR on anisotropy ratios is small for the clayey silt and the Dogger Bank sand with $D_r \sim 80\%$. However, these data sets are too limited to draw firm general conclusions about the effect of OCR on the anisotropy ratio.

The overconsolidation ratio is in this paper defined as $OCR = p'_c/\sigma'_{vc}$, and assumes that the soil is unloaded from a vertical preconsolidation stress, p'_c, to its present vertical effective stress, σ'_{vc}. In some situations, however, the soil may undergo an unload/reload history where the soil has been unloaded from p'_c to a vertical effective stress, σ'_{v0}, before it is reloaded to $\sigma'_{vc} = \sigma'_{v0} + \Delta\sigma'_v$. This is the case for a gravity platform installed on an overconsolidated clay with a preconsolidation stress, p'_c. The vertical effective in situ stress is then σ'_{v0} before installation, and increases by $\Delta\sigma'_v$
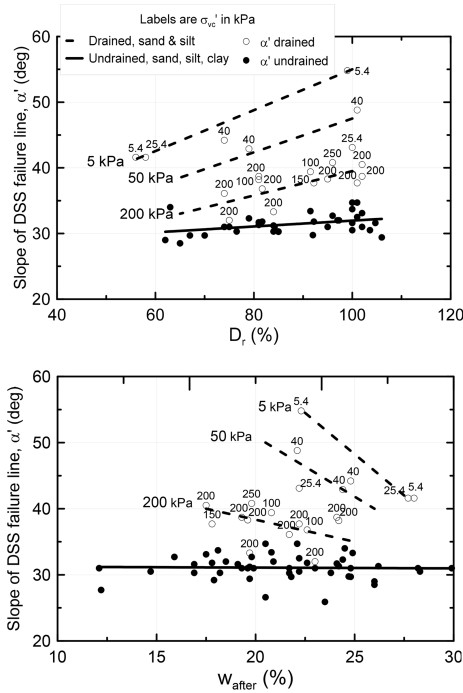
Figure 10.10. Slope of failure line, α', in effective stress path for drained and undrained monotonic DSS tests as a function of D_r (upper) and w (lower).

with time due to consolidation under the weight of the platform, to $\sigma'_{vc} = \sigma'_{v0} + \Delta\sigma'_v$.

The upper diagram in Figure 10.8 shows the undrained DSS shear strength of Drammen clay as a function of the vertical effective stress history. The unloading curve is consistent with the data in Figure 10.8. The reloading curve shows that the shear strength at a given σ'_{vc} will be influenced if the clay has been at a lower effective stress previously. The shear strength will be lower if $\sigma'_{vc} < \sim 200$ kPa, corresponding to OCR~2, and somewhat higher if $\sigma'_{vc} > \sim 200$ kPa. The data is used to make a more general estimate about the effect of lower previous stress history in the lower part of Figure 10.8.

10.6 Slope of failure envelope in effective stress path plots

Triaxial friction angles for sand as a function of relative density and consolidation stress can be found in Andersen & Schjetne (2013). Both peak and constant volume drained friction angles (ϕ'_p and ϕ'_{cv}), undrained effective stress friction angle, ϕ'_u, and dilatancy angle, ψ', are given. The data are predominantly for quartz sand with no or very little fines content. The effect of fines has been investigated in triaxial tests on Dogger Bank sand in the Schmertman Research Laboratory at NGI by S. Quinteros in connection with his Master Thesis at the University of British Colombia. The tests were run on clean sand and on sand where 20%
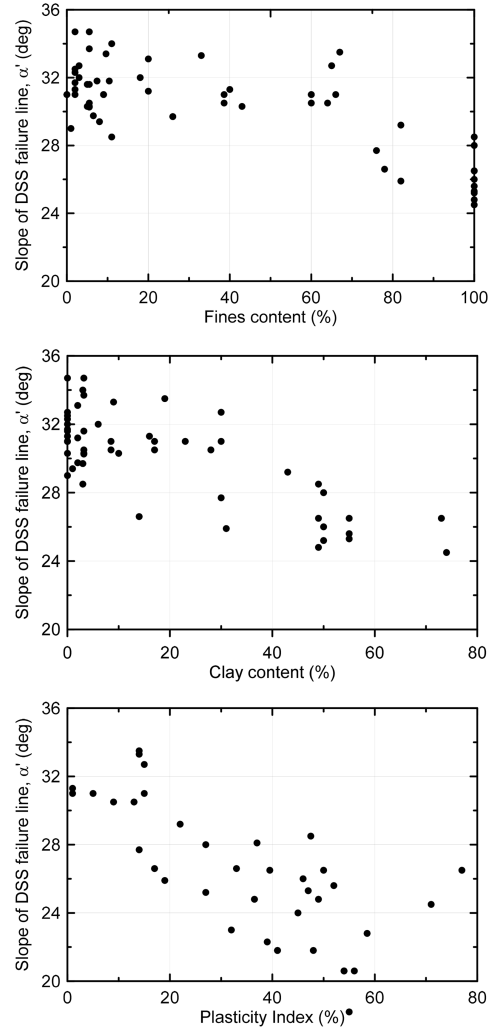
Figure 10.11. α'-value in undrained monotonic DSS tests as a function of fines content, clay content and plasticity index.

fines were added. The results are plotted in Figure 10.9 which also includes results from Blaker & Andersen (2015). The majority of the tests were run undrained, but some drained tests are also included. The tests were prepared by moist tamping and consolidated to a vertical effective stress of $\sigma'_{vc} = 200$ kPa and $K'_0 = 0.45$. Some tests were overconsolidated to an OCR = 4 and run at $\sigma'_{vc} = 200$ kPa and $K'_0 = 1$. The friction angles for Dogger Bank sand confirm that the peak drained friction angle is greater than the undrained effective stress friction angle, but values generally plot above the data in Andersen & Schjetne (2013). Since the diagrams in Andersen & Schjetne (2013) are based on a much larger data base with different sands, it is recommended to use that reference to select friction angles for design. Nonetheless, the data in Figure 10.9 reveal interesting results about the effect of fines. There is essentially no effect of fines when comparing friction

angles as a function of relative density, but a clear effect when comparing results as a function of water content.

Data for the slope of the failure envelope, α', in DSS tests (Figure 6.8) are plotted as a function of relative density and water content for both drained and undrained conditions in Figure 10.10. The data for drained conditions contain sand with fines content between 0 and 20%. The vertical consolidation stress ranges from 5.4 to 250 kPa. The data for undrained conditions contain sand, silt and clay with consolidation stress ranging from 30 to 1300 kPa.

For drained conditions, α' depends strongly on the vertical consolidation stress, increasing with increasing relative density and decreasing with increasing water content. There is also a tendency for α' to decrease with increasing fines content. The curves are estimates for 0 to 10% fines content.

For undrained conditions, α' increases slightly with relative density, but is essentially independent of water content. Undrained α' was determined at relatively high effective stresses where the soil dilates and was found to be essentially independent of the vertical consolidation stress.

The α'-value for undrained conditions is also plotted as a function of fines content, clay content and plasticity index in Figure 10.11. The plots show that the undrained α' is essentially constant for fines content below 70% and clay content below 30%. Above these limits, α' deceases linearly with increasing fines and clay content. α' deceases linearly with increasing plasticity index. There are different number of data points in the three diagrams in Figure 10.11, because fines content, clay content and plasticity index were not available for all the points.

11 MONOTONIC STRESS-STRAIN CHARACTERISTICS

11.1 *Normally consolidated sand and silt*

The comparison of the stress-strain curves for very dense Baskarp sand presented in Figure 11.1 gives an impression of the difference between drained and undrained stress strain behavior and the stress-strain anisotropy of very dense sand. The samples were consolidated with $K_0 = 0.45$, giving $\tau_0 = 0.5 \cdot \sigma'_{vc} \cdot (1 - K_0) = 0.275 \cdot \sigma'_{vc}$. The tests were run by increasing the vertical stress in compression and increasing the horizontal stress in extension. The drained stress strain behavior will be different if the drained tests are run by decreasing the normal stresses (see Figure 6.8).

The plot for the triaxial tests is in terms of vertical strain. The shear strain will be 1.5 times the vertical strain in the undrained case. In the drained tests the vertical strain is influenced by the volumetric strains due to change in octahedral stress and dilatancy. Volumetric strains can be calculated with the constrained moduli in Section 16 and the dilatancy parameters in Andersen & Schjetne (2013).
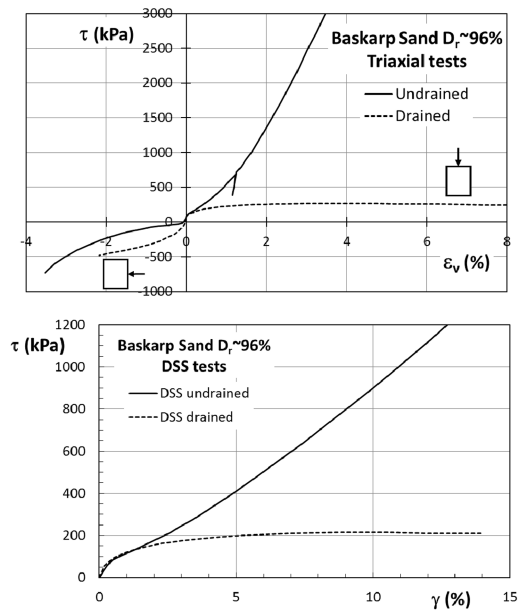
Figure 11.1. Stress-strain relations for drained and undrained monotonic triaxial compression and extension tests (upper) and DSS tests (lower) on very dense normally consolidated Baskarp sand.

The curves in Figure 11.1 show that the stress-strain behavior is highly non-linear and highly anisotropic. The drained and undrained stress-strain curves are similar until the effective stress paths approach the failure envelope. Then the undrained tests dilate and excessive shear strains do not develop within shear stresses of practical interest. The extension test does exhibit soft behavior just after the shear stress is reversed, but the stiffness increases again as the shear strain increases. The drained extension test is temporarily stiffer than the undrained test, but this would not have been the case if the test had been run by decreasing the vertical stress, which can be the case in some prototype situations.

Figure 11.2 shows the additional shear stress, $\tau - \tau_0$, applied after consolidation in the undrained tests. The shear stress is normalized to the reference stress, σ'_{ref}, and an anisotropy factor f. The anisotropy factors that give the best fit of triaxial compression and extension curves with the DSS curve are f = 0.33 for triaxial compression and 0.85 for triaxial extension. The figure shows that the use of the anisotropy factors bring the curves closer together, but there is still some difference between the three curves, and the anisotropy also varies with shear strain. The anisotropy factors indicate that the shear stiffeness for compression and extension are generally higher than for DSS. The stress-strain anisotropy may be smaller for looser soils.

The stress-strain behavior will be less dilatant for lower relative density and increasing fines content (e.g. Blaker & Andersen 2015).
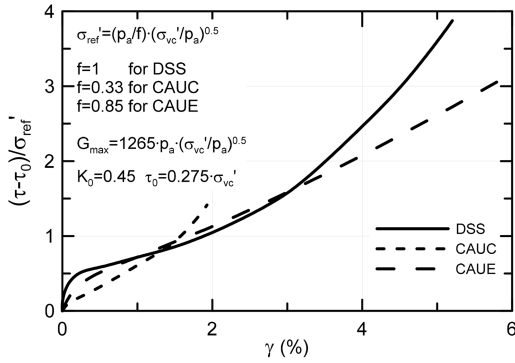
Figure 11.2. Normalised stress-strain relationships for undrained monotonic triaxial and DSS tests. Very dense normally consolidated Baskarp sand (based on Andersen et al. 1994).

An estimate of stress-strain behavior in DSS tests on sand with different relative densities is presented in Figure 11.3. The estimate is based on interpolation and extrapolation of data from various sands and silts in NGI's data base. This involves considerable uncertainty, and the curves should be used for guidance only.

The curves are given for different values of $(\tau_f/\sigma'_{ref})_{N=10}$ $\tau_a = 0$ and can be related to relative density and water content through the diagrams for static shear strength in Figures 10.1 and 10.2. The exponent in the reference stress used for normalization is consistent with the values established in Section 10.1, i.e. $n = 0.1$ to 0.9.

11.2 *Normally consolidated clay*

The stress-strain behavior of clay is also highly anisotropic and non-linear, as seen for normally consolidated Drammen Clay in Figure 11.4. In contrast to the very dense sand (Figure 11.1), however, the normally consolidated clay exhibits a definite failure and strain softening, especially in compression. The stress-strain behavior is sensitive to sample disturbance, as shown in Lunne et al. (2006).

11.3 *Effect of OCR on stress-strain characteristics*

The effect of overconsolidation ratio on the stress strain relationship of clay is illustrated in Figure 11.4. It can be seen that the shear strain at a given degree of shear strength mobilization, τ/s_u, increases with increasing OCR, meaning that the normalized secant modulus, G/s_u, decreases with increasing OCR for a given degree of strength mobilization. The effect of OCR is less significant for very dense sand. The effect of OCR on shear modulus is further illustrated in Figure 13.24 and discussed in Section 13.7, both for monotonic and cyclic loading.
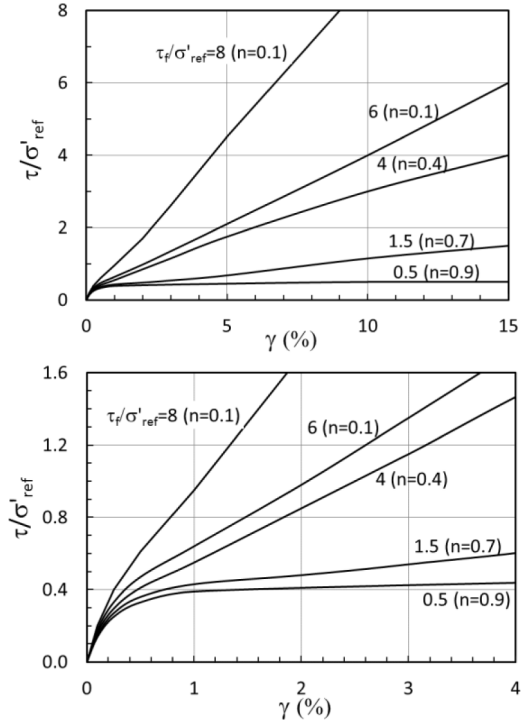
Figure 11.3. Estimate of undrained monotonic DSS stress-strain characteristics for sand and silt with different $(\tau_{cy,f}/\sigma'_{ref})_{N=10}$. The lower diagram is a blow-up of the upper diagram.
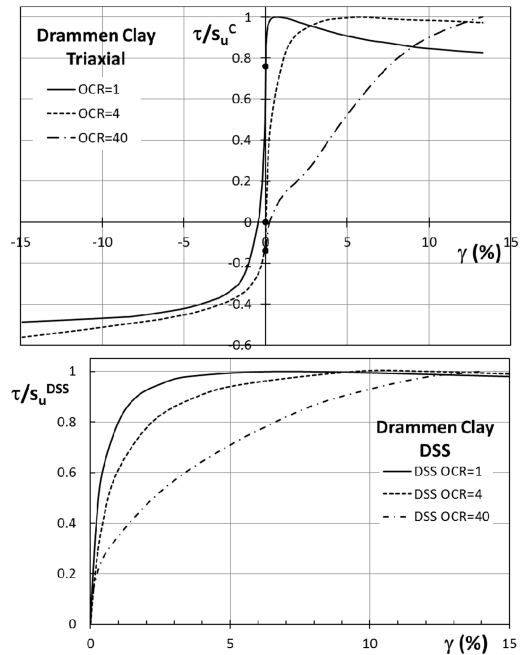
Figure 11.4. Normalized stress-strain relationships in undrained monotonic tests on Drammen Clay with different overconsolidation ratios (based on Andersen et al. 1988).
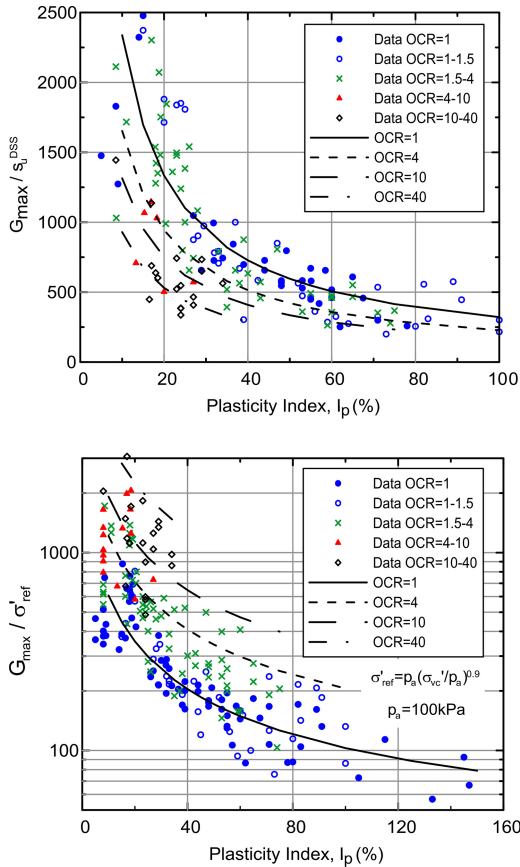
Figure 11.5. Initial shear modulus normalized by s_u^{DSS} (upper) and σ_{ref} (lower) as a function of plasticity index, I_p, and overconsolidation ratio, OCR.

11.4 *Initial shear modulus, G_{max}*

The initial shear modulus from shear wave velocity measurements on a number of clay samples with different plasticity and overconsolidation ratio is plotted as a function of plasticity index and overconsolidation ratio in Figure 11.5. The initial shear modulus is normalized by the undrained DSS strength in the upper diagram and by the reference stress, σ'_{ref}, in the lower diagram. The same exponent, n = 0.9, as for static strength of clay is applied. There is scatter in the data, but still a clear trend for normalized values to decrease with increasing plasticity index. G_{max}/s_u^{DSS} decreases and G_{max}/σ'_{ref} increases with increasing OCR. Best estimate values can be expressed by

$$G_{max}/s_u^{DSS} = (30+300/(I_p/100+0.03))\cdot OCR^{-0.25} \text{ and}$$

$$G_{max}/\sigma_{ref}' = (30+75/(I_p/100+0.03))\cdot OCR^{0.5}$$

The equations should be used with care outside the range of plasticity index that they are drawn for in the diagrams. One should also consider the scatter indicated in the diagrams when using the expressions.

The data in Figure 11.5 and the expressions above are valid for tests where overconsolidation is generated by unloading the vertical effective stress. The effective stress can also be reduced due to pore pressure, u_p, generated by cyclic loading, giving an equivalent overconsolidation defined as

$$OCR_{eq}=\sigma_{vc}'/(\sigma_{vc}'-u_p).$$

G_{max} measured in cyclic tests where the pore pressure is recorded, show that G_{max} is lower in a cyclic test than in a test where the vertical stress is reduced by unloading, probably due to some disturbance to the soil structure due to the cyclic strains. Based on G_{max} measurements during and after undrained cyclic DSS tests on soft clays with $I_p = 16\%$ and 45% and the quick clay in Section 16, it was found that the following expression would apply for these clays when the overconsolidation is caused by pore pressure from cyclic loading:

$$G_{max}/\sigma_{ref}' = (30+75/(I_p/100+0.03))\cdot OCR_{eq}^{0.33}$$

This expression can be applied to calculate the initial shear modulus during a cycle, like in the model proposed by Kaynia & Andersen (2015) in Section 18.5. The reduction in G_{max} due to cyclic loading is in line with the recommendation in Section 16 that the constrained reloading modulus to calculate volumetric strains due to dissipation of cyclically induced pore pressure should be reduced to 2/3 of the reloading measured in a conventional oedometer.

12 CYCLIC STRENGTH CORRELATIONS

12.1 *Cyclic DSS shear strength of normally consolidated sand and silt*

12.1.1 *Symmetrical cyclic loading ($\tau_a = 0$) and N = 10*

The cyclic shear strength of sand and silt for 10 load cycles is presented as a function of relative density in Figure 12.1 and as a function of water content in Figure 12.2. The relative density and water content values are the values after consolidation. The number above each data point shows the fines content (upper diagrams) and the clay content (lower diagrams). The fines content varies from 0% (clean sand) to 81%. The clay content varies from 0% to 10%. More data points are available versus water content than versus relative density, because relative density is not defined for the soils with the highest fines content.

The shear strength has been normalized to the reference stress, $\sigma_{ref}' = p_a \cdot (\sigma_{vc}'/p_a)^n$, as defined in Section 7.8. An empirical exponent of n = 0.9 was found to give the best fit for the cyclic shear strength, as compared to n = 0.5 for the static shear strength (Section 10.1). This difference in exponent value means that the effect of σ_{vc}' on the normalized shear strength is less for cyclic than for static shear strength. The data include tests with consolidation stress in the range of

$\sigma'_{vc} = 40$ to $710\,kPa$, but most data are within $\sigma'_{vc} = 100$ to $250\,kPa$. The curves are thus most representative for the range of $\sigma'_{vc} = 100$ to $250\,kPa$.

The tests have been run on "intact" samples and on samples prepared by moist reconstitution. The samples are normally consolidated. In cases with "intact" samples, the specimens are loaded so far above the in situ stresses that the volumetric strains should break down any in situ preconsolidation effect.

The cyclic loading has been stress controlled with symmetrical cyclic loading and 10 s load period. Six of the samples were not presheared. The other 28 samples were presheared with 200 to 400 cycles at a cyclic shear stress of $\tau_{cy}/\sigma'_{vc} = 0.04$ to 0.1. The curves are valid for tests with moderate preshearing with 400 cycles at a cyclic shear stress of $\tau_{cy}/\sigma'_{vc} = 0.04$ or less.

The cyclic shear strength has been defined as the cyclic shear stress at a large cyclic shear strain, generally 15%. However, some of the tests with very high density did not reach 15% shear strain in 10 cycles even when a high cyclic shear stress was applied. The shear strength was in these cases defined as the shear stress at a shear strain of 5 or 7.5%. These shear strengths were all very high, and the deviation from the general failure criterion is not believed to be of practical consequence.

The data in Figures 12.1 and 12.2 show the same tendencies as the static shear strength, with cyclic shear strength decreasing with increasing fines content. Estimated curves for fines content less than 5% and fines content of 20% and 35% are included in the figures. The curve for 35% fines content in Figure 12.1 is uncertain because relative density determination is questionable for such high fines content, and the lack of data on relative density for tests with fines content above 23%. This curve is therefore estimated from the correlation with water content (Figure 12.2) and the data for static shear strengths. As for the static shear strength in Section 10.1, the curve for 35% fines content is expected to represent a lower limit, with the cyclic shear strength increasing again when the fines content increases above 35%. One data point for soil with 20% fines content gives a higher strength than the rest of the data. This is the same soil that showed a tendency for high static strength, and may be related to uncertainty in the relative density determination for soil with high fines content, as mentioned in Section 10.1. The data for this soil agree better with the rest of the data when plotted versus water content.

The cyclic shear strength curves are compared to the static shear strength curves in Figure 12.3. Figure 12.4 shows the ratio between the cyclic shear strength after 10 cycles and the static shear strength. The comparisons are valid for $\sigma'_{vc} = 100\,kPa$. The comparison will vary with consolidation stresses because the exponent n in σ'_{ref} is different for cyclic and static strengths.

The comparison shows that the cyclic shear strength for 10 cycles is smaller than the static shear strength. The ratio of cyclic to static strength decreases with decreasing fines content, increasing relative density and decreasing water content. The reason is that the
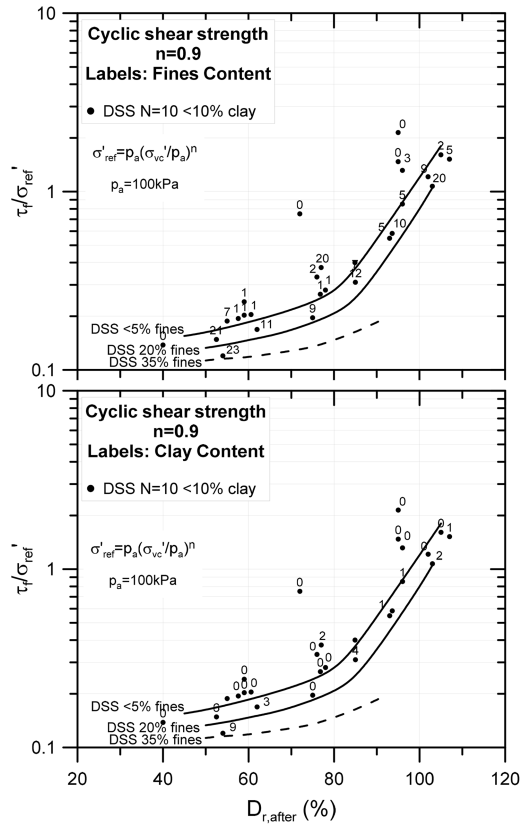

Figure 12.1.   Cyclic shear strength for 10 cycles with symmetrical cyclic loading in DSS tests on normally consolidated sand and silt as a function of relative density after consolidation. Upper: Fines content. Lower: clay content.

static shear strength relies more than the cyclic strength on dilation with decreasing fines content, increasing relative density and decreasing water content.

12.1.2   *Effect of number of cycles*
The cyclic shear strength diagrams in the preceding sections are for 10 load cycles. The cyclic shear stress to failure for other numbers of cycles can be determined by means of Figure 12.5. Normally consolidated Drammen clay is included as reference.

The greatest effect of number of cycles occurs for the strongest soils.

12.1.3   *Non-symmetrical cyclic loading ($\tau_a > 0$)*
The cyclic shear stress at failure and the cyclic shear strength will depend on the average shear stress, τ_a, as explained in Section 7. Figures 12.6 to 12.10 present five examples of combinations of average and cyclic shear stresses that cause failure in DSS tests on sand or silty sand after different number of cycles (N = 1, 10, 100 and 1000). Four of the examples are for clean sand. Grain size characteristics for the different soils are presented in Table 7.1. The upper diagrams are for the case when $\Delta\tau_a$ is applied under drained conditions and the lower diagrams are for undrained $\Delta\tau_a$. It
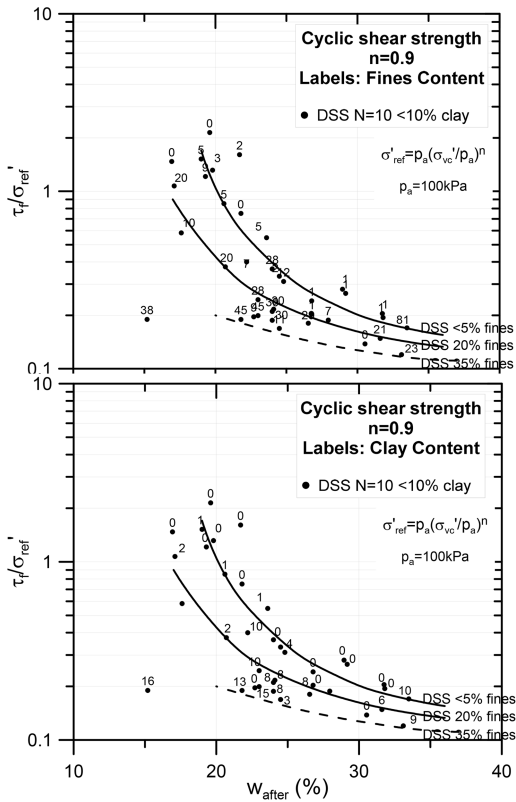
Figure 12.2. Cyclic shear strength for 10 cycles with symmetrical cyclic loading in DSS tests on normally consolidated sand and silt as a function of water content after consolidation. Upper: Fines content. Lower: clay content.
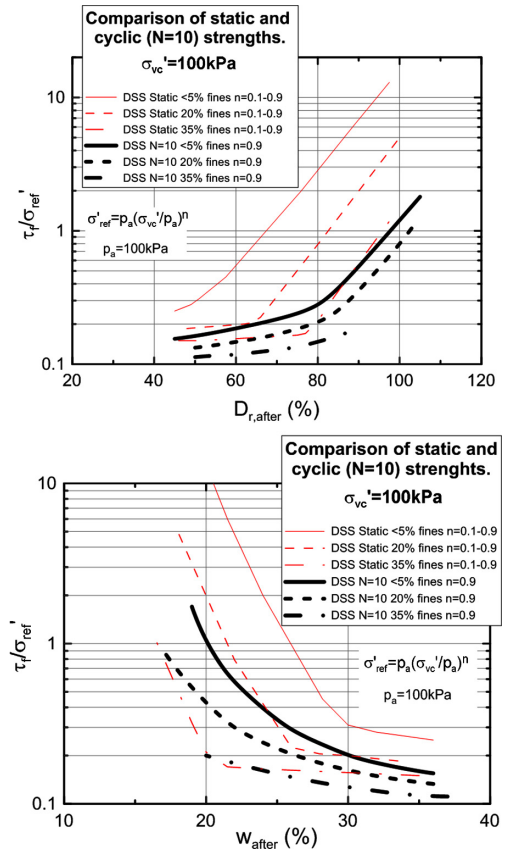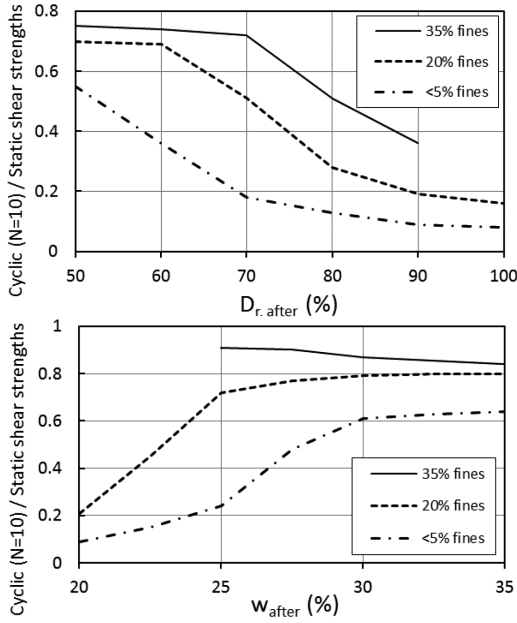

Figure 12.3. Cyclic shear strength for 10 cycles with symmetrical cyclic loading compared to static shear strength as a function of relative density (upper) and water content (lower). DSS tests. Normally consolidated sand & silt. Valid for $\sigma'_{vc} = 100$ kPa.

was generally difficult to bring the very dense samples to 15% shear strain during undrained cyclic loading, and the "failure contours" are presented for 3% shear strain for the Baskarp sand and 5% shear strain for the Dogger Bank sand. The fifth example is a medium dense sand where $\Delta\tau_a$ is applied undrained, and the failure strain is 15%.

The contour plots for drained and undrained $\Delta\tau_a$ have the same intersection points at the vertical axis. For the dense sands, the contours for undrained $\Delta\tau_a$ show considerably higher cyclic strength than the contours for drained $\Delta\tau_a$ when τ_a is large enough for the failure mode to result from large average shear strain. This is due to shear-induced dilatancy under undrained conditions. The dense Dogger Bank and Baskarp sands generally show similar behavior, apart from the contours at high τ_a, where the Dogger Bank sand shows higher cyclic strength than Baskarp sand. The difference is partly due to the difference in shear strain used to define failure. The Baskarp contours would probably look even more like the Dogger Bank contours if they had been drawn for 5% shear strain. Another reason is that Baskarp sand was the first very dense sand to be tested under these shear stress conditions. There was also limited Baskarp test data in the region with

high τ_a. The Baskarp contours were therefore drawn on the conservative side. The Dogger Bank sand is therefore the most representative for very dense sand in the region with high τ_a.

The fifth example (Figure 12.10), which is for a lower density sand, does not show the same increase in cyclic shear strength with undrained $\Delta\tau_a$ as the very dense sand, and the shear strength is considerably lower than for the dense sands.

A collection of $N = 10$ failure contours for sands and silts with different densities is presented in Figures 12.11 and 12.12, for undrained and drained $\Delta\tau_a$, respectively. Grain size characteristics for the different soils are presented in Table 7.1. The intersection with the horizontal axis for drained $\Delta\tau_a$ can be determined by the drained shear strength defined in Figure 6.8 and the failure line angles in Figure 10.10. Normally consolidated Drammen clay is included for reference in the diagram for undrained $\Delta\tau_a$. A failure strain of 15% is used for the lower density soils ($D_r < 80\%$). As discussed earlier, it is difficult to bring very dense soils to 15%, and a failure strain of 5% is used for

Figure 12.4. Ratio of cyclic shear strength for 10 cycles with symmetrical cyclic loading and static shear strength as a function of relative density (upper) and water content (lower) after consolidation. DSS tests. NC sand & silt. Valid for $\sigma'_{vc} = 100$ kPa.
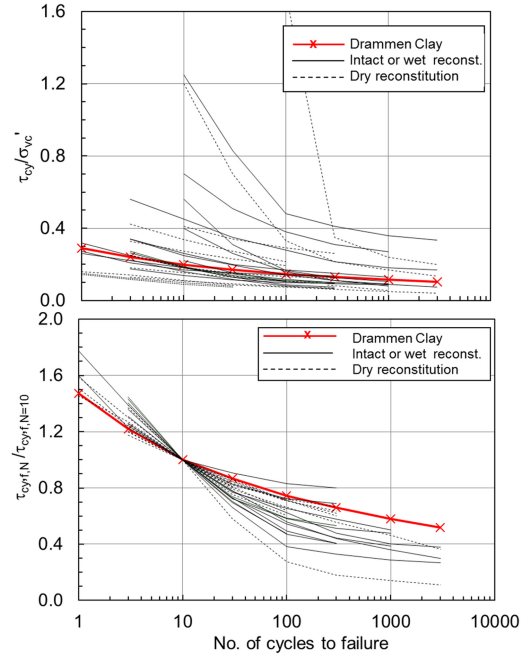

Figure 12.5. Cyclic shear stress at failure as a function of number of cycles in DSS tests with $\tau_a = 0$ on normally consolidated sand and silt. $\sigma'_{vc} = 85$–710 kPa. Upper: $\tau_{cy,f}/\sigma'_{vc}$ vs. N_f. Lower: Normalized to $\tau_{cy,f}$ for $N = 10$ (Adapted from Andersen 2009).

the very dense soils. For the very dense Baskarp sand a lower failure strain criterion of 3% is used. Figure 12.13 shows the effect of failure strain criterion of 5% versus 15% for two sands with 59% and 86% relative density. The effect of failure strain criterion increases with increasing relative density.

Comparison of Figures 12.11 and 12.12 confirms that there can be a significant effect of whether the average shear stress is applied drained or undrained. This is further illustrated for some examples in Figure 12.14. The effect of drained vs. undrained $\Delta \tau_a$ is small when cyclic shear strain is the governing failure mode, but the difference can become significant when the average strain becomes governing. The effect increases with increasing density, and for high relative densities the cyclic strength $(\tau_{f,cy} = (\tau_a + \tau_{cy})_f)$ for undrained $\Delta \tau_a$ can be significantly larger than for drained $\Delta \tau_a$. For lower relative densities, however, the cyclic strength can be lowest for undrained $\Delta \tau_a$. The effect increases with increasing shear strain, as can be seen from the upper diagram in Figure 12.14, where the comparison is made for failure strains of 5% and 15% for one of the sands.

Based on interpolation and extrapolation of the data in Figures 12.6 to 12.14 and other data on different sands and silts in NGI's data base, failure contour diagrams for sand and silt of different densities are sketched in Figures 12.15 and 12.16 for undrained and drained $\Delta \tau_a$, respectively. The construction of the diagrams involves considerable uncertainty, and the contours should be used with caution.

The diagrams are given for different values of $(\tau_{cy,f}/\sigma'_{ref})_{N=10}$ for $\tau_a = 0$ and can be related to relative density and water content through the diagrams for cyclic shear strength in Figures 12.1 and 12.2.

The exponents in the reference stress used for normalization are consistent with the values established in Sections 12.1.1 and 10.1; i.e. $n = 0.9$ for τ_{cy} on the vertical axis and $n = 0.1$ to 0.9 for undrained τ_a on the horizontal axis in Fig 12.15. $n = 0.9$ is used for the drained τ_a on the horizontal axis in Figure 12.16. This gives an intersection of the failure curves with the horizontal axis in Figure 12.16 which is reasonably consistent with the drained static shear strength based on the angle of the drained failure envelope, α', in Figure 10.10.

Cyclic strain contours for the same conditions are presented in Figure 13.1, pore pressure contours in Figure 14.1, and average and cyclic shear strain contours in Figures 13.2 to 13.11.

12.2 *Cyclic triaxial shear strength of normally consolidated sand and silt*

12.2.1 *Cycling at $\tau_a = \tau_0$ and $N = 10$*

Figures 12.17 and 12.18 compare the cyclic shear stress, $\tau_{cy,f}$, at failure for 10 cycles in anisotropically consolidated triaxial tests with $\tau_a = \tau_0$ to DSS tests with $\tau_a = 0$. τ_0 is the shear stress during consolidation. Seven of the samples were prepared dry. The rest were intact samples or prepared wet. Preshearing was
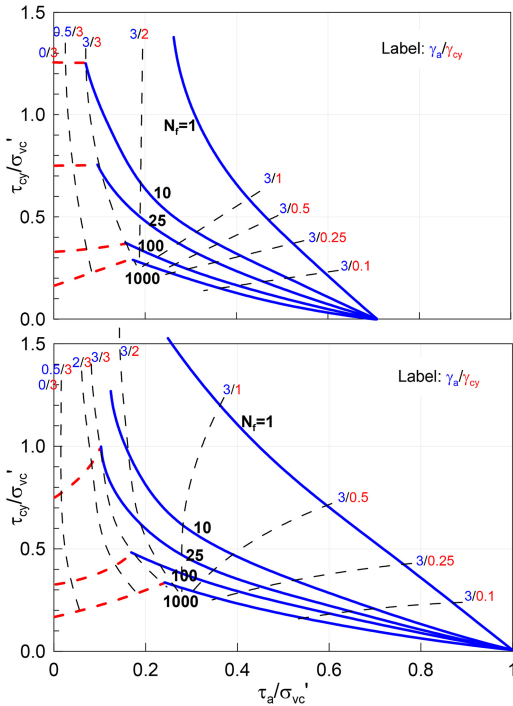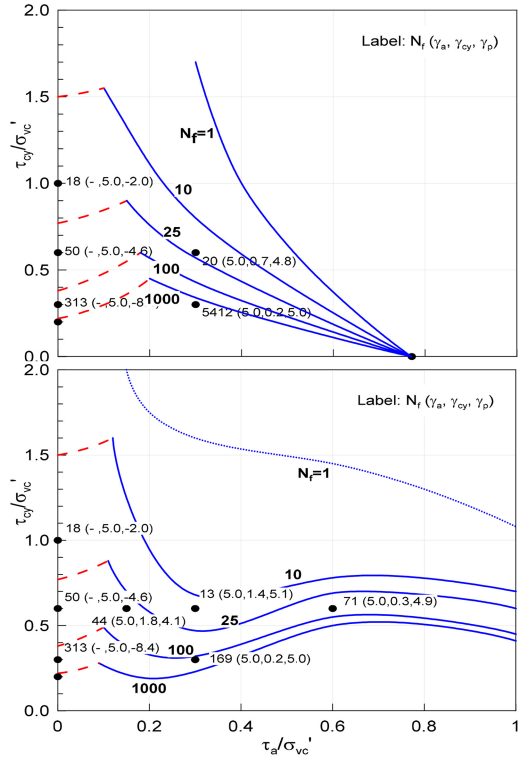
Figure 12.6. No. of cycles to "failure" ($\gamma = 3\%$) as a function of average and cyclic shear stresses. DSS tests. Normally consolidated very dense Baskarp sand (Andersen & Berre 1999). Upper: Drained $\Delta\tau_a$. Lower: Undrained $\Delta\tau_a$. $\sigma'_{vc} = 250$ kPa. Preshearing: 400 cycles at $\tau_{cy}/\sigma'_{vc} = 0.1$.

not applied for the two dry samples with the lowest strength and for two of the wet samples with 30% fines content. The third soil with 30% fines was presheared with 400 cycles of $\tau_{cy}/\sigma'_{vc} = 0.1$. This soil had a cyclic shear stress at failure between the other two. The rest of the samples were presheared with 200 to 400 cycles at a cyclic shear stress in the range $\tau_{cy}/\sigma'_{vc} = 0.05$ to 0.08.

One of the soils with 20% fines content gives a higher strength than the rest of the data when plotted as a function of relative density. This is the same soil that exhibits DSS and triaxial static strengths and DSS cyclic strength on the high side compared to the rest of the data. As speculated previously, this may be related to uncertainty in the relative density since the agreement is better when plotted as a function of water content.

Several of the cyclic triaxial tests were performed on soil that was also used for cyclic DSS testing, and the ratio between cyclic shear stresses at failure in these triaxial and DSS tests is plotted in Figure 12.19. The ratio varies between 1 and 3 with an average of 1.78 and a standard deviation of 0.55. There is some tendency for reduction in the ratio with increasing fines content, but no clear relation to other parameters such as relative density.

The plots in Figures 12.17 and 12.18 present best estimate curves for triaxial cyclic shear stress that

Figure 12.7. Cycles to "failure" ($\gamma = 5\%$) as a function of average and cyclic shear stresses. DSS tests. Normally consolidated very dense ($D_r \sim 105\%$) Dogger Bank sand. No fines. (Blaker & Andersen 2015). Upper: Drained $\Delta\tau_a$. Lower: Undrained $\Delta\tau_a$. $\sigma'_{vc} = 200$ kPa. Preshearing: 400 cycles at $\tau_{cy}/\sigma'_{vc} = 0.06$.

cause failure after 10 cycles. These curves are established by multiplying the DSS curves by 1.78 for fines content of $<5\%$ and 20% and by 1.5 for 35% fines content.

One should keep in mind that the cyclic failure stress in the triaxial tests in Figures 12.17 and 12.18 is the cyclic stress component when $\tau_a = \tau_0$. To establish the cyclic shear strength, the initial shear stress, τ_0, shall be added for compression and subtracted for extension. This is discussed further in Section 12.5.

12.2.2 *Effect of number of cycles*
The cyclic shear strength diagrams in the preceding sections are for 10 load cycles. The cyclic shear stress to failure for other numbers of cycles can be determined by means of Figure 12.20. Normally consolidated Drammen Clay is included as a reference.

12.2.3 *Average shear stress different from initial shear stress ($\tau_a \neq \tau_0$)*
Five examples of combinations of average and cyclic shear stresses that cause failure in triaxial tests on clean sand after different numbers of cycles are presented in Figures 12.21 to 12.25. The upper diagrams are for undrained $\Delta\tau_a$, and the lower diagrams are
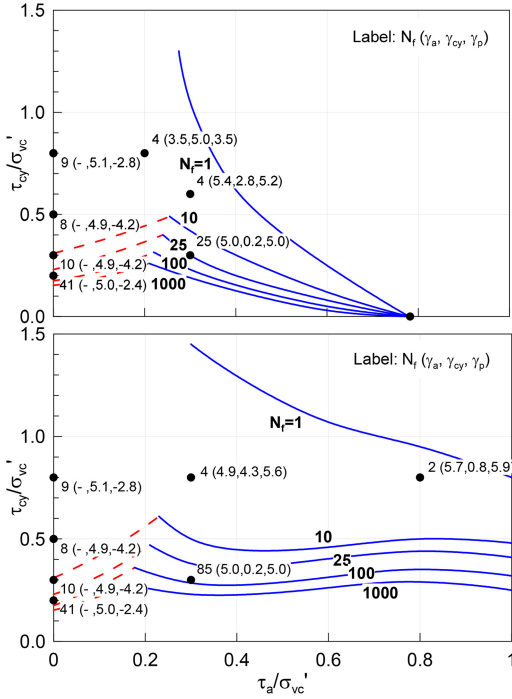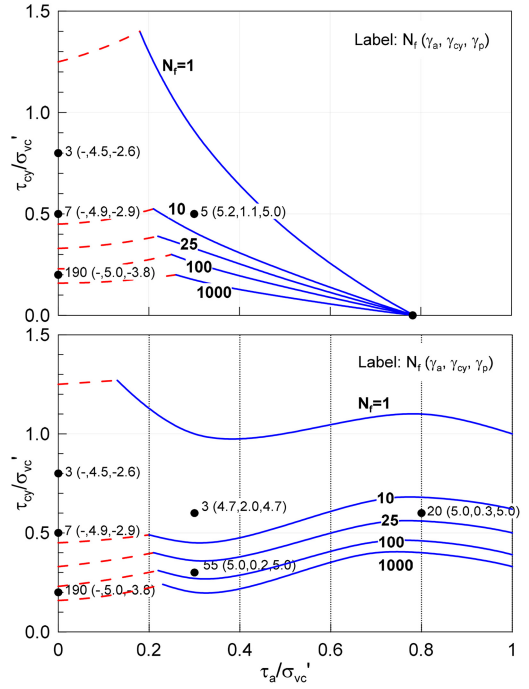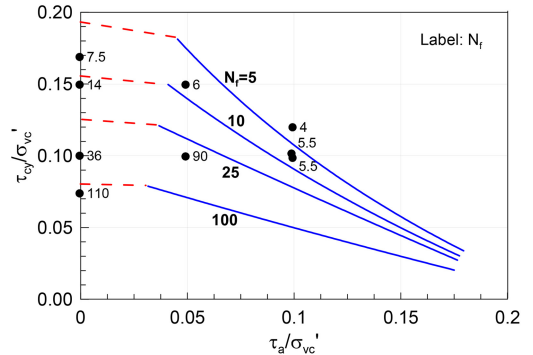
Figure 12.8. No. of cycles to "failure" ($\gamma = 5\%$) as a function of average and cyclic shear stresses. DSS tests. Normally consolidated medium dense ($D_r \sim 77\%$) Dogger Bank sand. No fines. (Blaker & Andersen 2015). Upper: Drained $\Delta\tau_a$. Lower: Undrained $\Delta\tau_a$. $\sigma'_{vc} = 200$ kPa. Preshearing: 400 cycles at $\tau_{cy}/\sigma'_{vc} = 0.06$.

Figure 12.9. No. of cycles to "failure" ($\gamma = 5\%$) as a function of average and cyclic shear stresses. DSS tests. Overconsolidated (OCR=4) medium dense ($D_r \sim 77\%$) Dogger Bank sand. No fines. (Blaker & Andersen 2015). Upper: Drained $\Delta\tau_a$. Lower: Undrained $\Delta\tau_a$. $\sigma'_{vc} = 200$ kPa. Preshearing: 400 cycles at $\tau_{cy}/\sigma'_{vc} = 0.06$.

for drained $\Delta\tau_a$. As discussed earlier, it was difficult to bring the very dense samples to 15% shear strain during undrained cyclic loading, and the "failure contours" are presented for $\leq 3\%$ shear strain for the Baskarp sand, 5% shear strain for the dense Sand 3 ($D_r \sim 89\%$) and Dogger Bank sand, and 10% shear strain for the medium dense Sand 3 ($D_r \sim 62\%$). The shear strain was set to 1.5 times the vertical strain, which is an approximation for γ_a in the drained case, as also discussed in Section 13.4.

The contours for drained and undrained $\Delta\tau_a$ exhibit significant differences, as also seen for the DSS tests in Section 12.1.3. The contours have the same intersections at the vertical section at $\tau_a = \tau_0$, but the intersection at the horizontal axis depends strongly on whether $\Delta\tau_a$ is applied drained or undrained. The intersections with the horizontal axes are defined by the static compression and extension shear strengths. For drained conditions, the drained shear strengths depend on whether the tests are sheared to failure by increasing or decreasing the normal stresses. The different drained stress paths and the corresponding shear strengths are illustrated in Figure 6.8.

The Baskarp sand shows relatively less gain in strength with increasing $\Delta\tau_a$ than the other sands. This is because the Baskarp contours were drawn on the

Figure 12.10. No. of cycles to failure ($\gamma = 15\%$) as a function of average and cyclic shear stresses. DSS tests. Normally consolidated silty sand with w $\sim 24\%$ (Sand 31). Undrained $\Delta\tau_a$. $\sigma'_{vc} \sim 360$ kPa. No preshearing.

conservative (i.e. low) side, as discussed in section 12.1.3.

Average and cyclic shear strain contours for Baskarp sand and Sand 3 are presented in Figures 13.12 to 13.21, and pore pressure contours in Figure 14.2 to 14.10.

See blow-up below for low τ_a and τ_{cy} values
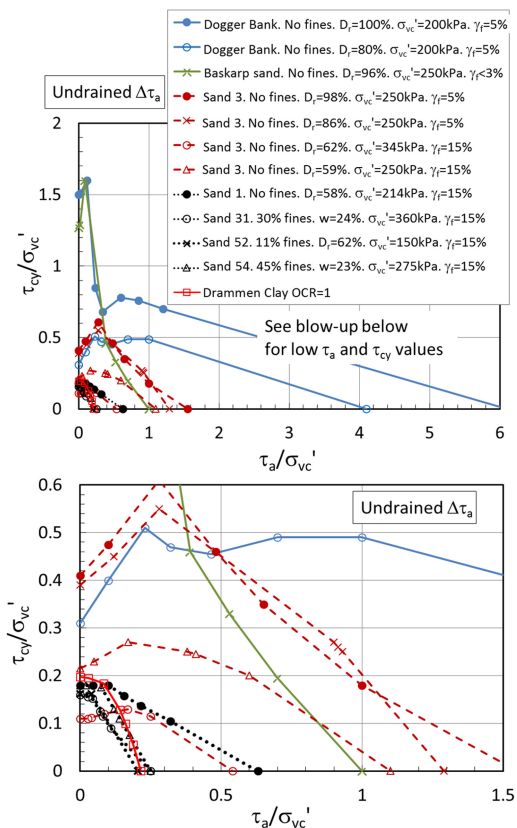
Undrained $\Delta\tau_a$

Figure 12.11.   Average and cyclic shear stresses that give failure in 10 cycles in DSS tests on different normally consolidated sands and silts. $\Delta\tau_a$ applied undrained. (Lower figure is a blow-up of the upper figure).
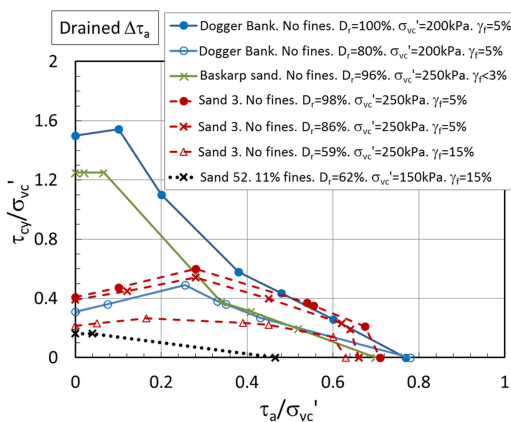
Drained $\Delta\tau_a$

- Dogger Bank. No fines. D_r=100%. σ_{vc}'=200kPa. γ_f=5%
- Dogger Bank. No fines. D_r=80%. σ_{vc}'=200kPa. γ_f=5%
- Baskarp sand. No fines. D_r=96%. σ_{vc}'=250kPa. γ_f<3%
- Sand 3. No fines. D_r=98%. σ_{vc}'=250kPa. γ_f=5%
- Sand 3. No fines. D_r=86%. σ_{vc}'=250kPa. γ_f=5%
- Sand 3. No fines. D_r=59%. σ_{vc}'=250kPa. γ_f=15%
- Sand 52. 11% fines. D_r=62%. σ_{vc}'=150kPa. γ_f=15%

Figure 12.12.   Average and cyclic shear stresses that give failure in 10 cycles in DSS tests on different normally consolidated sands and silts. $\Delta\tau_a$ applied drained.

A collection of N = 10 failure contours for sands and silts with different densities is presented in Figures 12.26 and 12.27. Grain size characteristics for the different soils are presented in Table 7.1.

Effect of failure criterion. Drained $\Delta\tau_a$

- Sand 3. No fines. D_r=86%. σ_{vc}'=250kPa. γ_f=10%
- Sand 3. No fines. D_r=86%. σ_{vc}'=250kPa. γ_f=5%
- Sand 3. No fines. D_r=59%. σ_{vc}'=250kPa. γ_f=15%
- Sand 3. No fines. D_r=59%. σ_{vc}'=250kPa. γ_f=5%

Effect of failure criterion. Undrained $\Delta\tau_a$

- Sand 3. No fines. D_r=86%. σ_{vc}'=250kPa. γ_f=10%
- Sand 3. No fines. D_r=86%. σ_{vc}'=250kPa. γ_f=5%
- Sand 3. No fines. D_r=59%. σ_{vc}'=250kPa. γ_f=15%
- Sand 3. No fines. D_r=59%. σ_{vc}'=250kPa. γ_f=5%
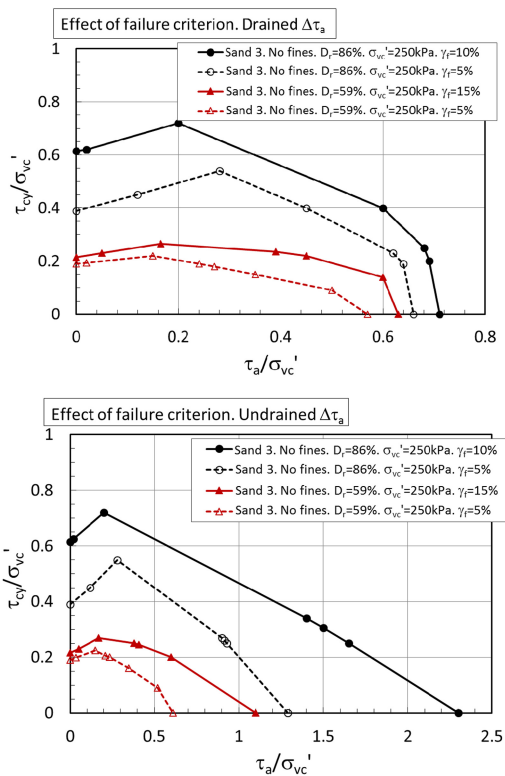
Figure 12.13.   Effect of failure criterion on shear stresses that give failure in 10 cycles in DSS tests on normally consolidated sands with 59% and 86% relative density. Upper: Drained $\Delta\tau_a$. Lower: Undrained $\Delta\tau_a$.

Figure 12.26 shows contours for sands where the change in average shear stress, $\Delta\tau_a$, is applied undrained. The upper figure shows data for high density soils ($D_r > 80\%$) and the lower figure shows data from tests with lower density. The data for sand with $D_r = 65\%$ is included in both plots for reference. Normally consolidated Drammen clay is included in the lower density diagram for comparison with clays. A failure strain of 15% is used for the lower density soils, apart from the soil with $D_r = 65\%$, where 10% is used. As discussed earlier, it is difficult to bring very dense soils to 15% shear strain, and a failure strain of 5% is used for the very dense soils. For Baskarp sand a failure criterion of 2% shear strain is used.

Figure 12.27 shows contours of average and cyclic shear stresses that cause failure after 10 cycles in triaxial tests on different sands and silts when the average shear stress, $\Delta\tau_a$, is applied drained. $\Delta\tau_a$ is applied drained by increasing σ_v' in compression and decreasing σ_v' in extension in all the soils apart from Baskarp sand where $\Delta\tau_a$ was applied by increasing σ_h' in extension. On the extension side it can be seen that the Baskarp contours indicate a significantly stronger behavior than the other soils, demonstrating the importance of whether the drained average shear stress is applied by increasing or decreasing the normal stress,
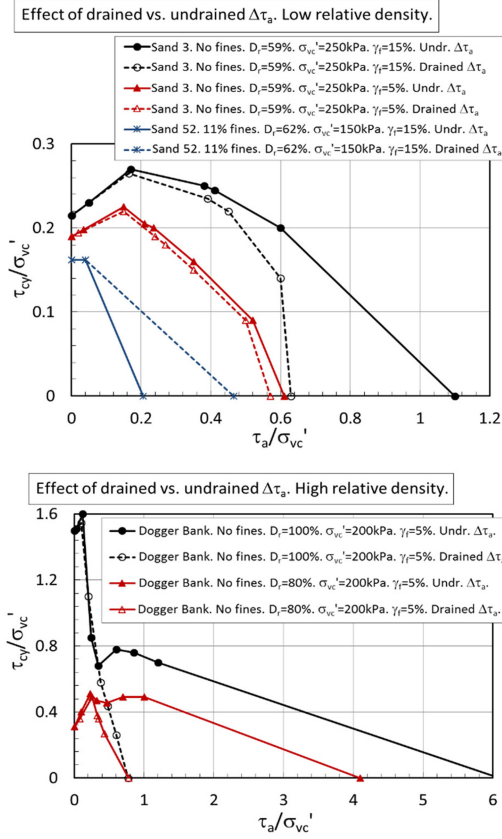
Figure 12.14. Effect of drained vs. undrained $\Delta\tau_a$ on shear stresses giving failure in 10 cycles. DSS tests. NC sands. Different relative density. Upper: Low density. Lower: High density.

in line with the effective stress paths indicated in Figure 6.8. The compression side only includes cases where the normal stresses are increased, but a similar difference would occur on the compression side for a reduction in the normal stress. The intersection with the horizontal axis for drained $\Delta\tau_a$ can be determined by the drained shear strengths defined in Figure 6.8.

The effect of whether the drained average shear stress is applied by increasing or decreasing the normal stress could possibly be reduced or eliminated by normalizing to the current effective stress, rather than the consolidation stress. This would involve updating the effective stress for the change in pore pressure due to cyclic loading, and is considered as a further interpretation outside the scope of this paper, as also mentioned in Section 7.8. Pore pressures required to perform this interpretation are given in Section 14.

Comparison of Figures 12.26 and 12.27 confirms the significant effect of whether the average shear stress is applied drained or undrained. The difference will depend on density, failure mode and whether $\Delta\tau_a$ is applied by increasing or decreasing the normal stress when $\Delta\tau_a$ it is applied drained. When $\Delta\tau_a$ is applied undrained, the sand will generally be stronger for dense
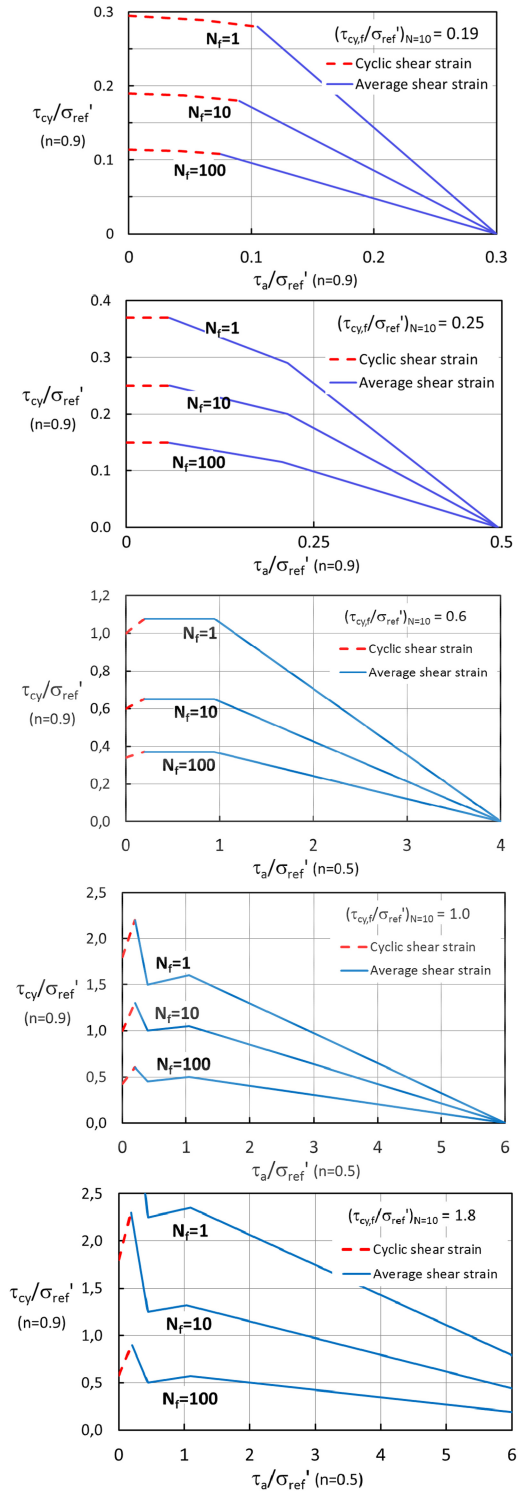
Figure 12.15. Combination of average and cyclic shear stresses that cause failure as a function of number of cycles. DSS tests on normally consolidated sand with <5% fines with different $(\tau_{cy,f}/\sigma'_{ref})_{N=10}$ for $\tau_a = 0$. τ_a applied undrained.

44
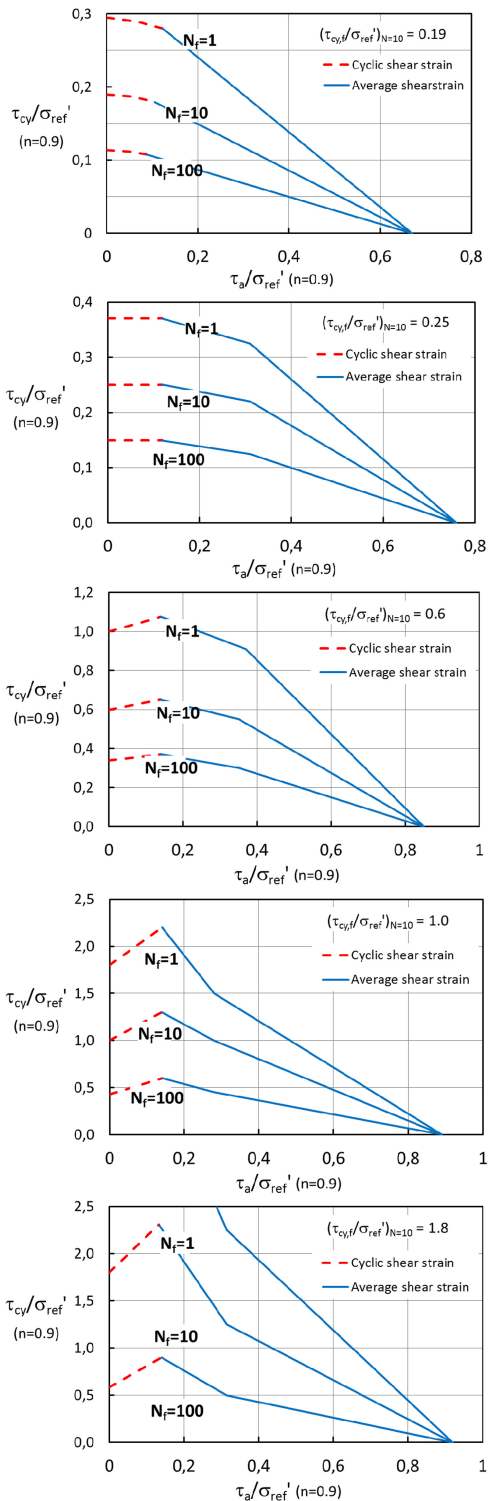
Figure 12.16. Combination of average and cyclic shear stresses that cause failure as a function of number of cycles. DSS tests on normally consolidated sand and silt with different $(\tau_{cy,f}/\sigma'_{ref})_{N=10}$ for $\tau_a = 0$. τ_a applied drained.
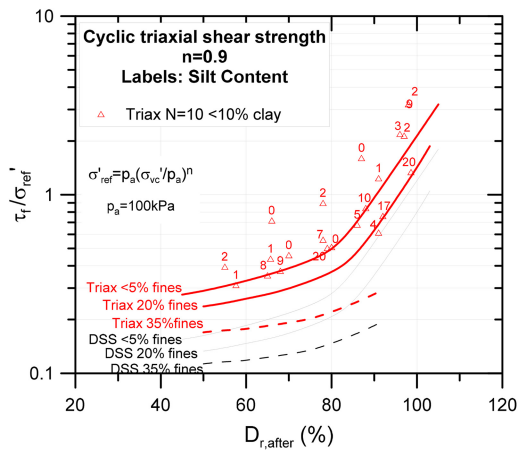
Figure 12.17. Cyclic shear stress to failure in 10 cycles. Anisotropically consolidated triaxial tests with $\tau_a = \tau_0$ as a function of relative density compared to DSS tests with $\tau_a = 0$. Normally consolidated sand and silt.
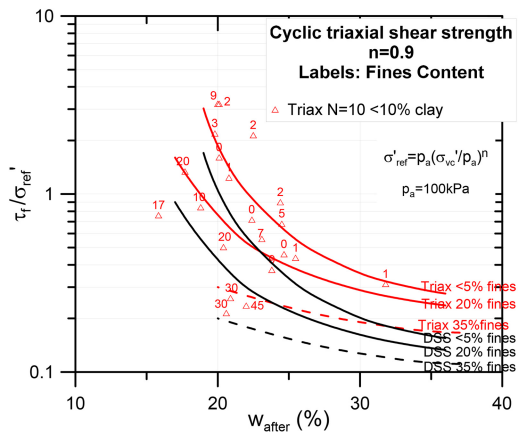
Figure 12.18. Cyclic shear stress to failure in 10 cycles. Anisotropically consolidated triaxial tests with $\tau_a = \tau_0$ as a function of water content compared to DSS tests with $\tau_a = 0$. Normally consolidated sand and silt.
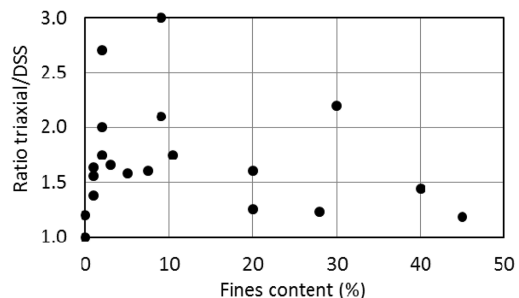
Figure 12.19. Ratio between cyclic shear stresses that give failure in 10 cycles for triaxial tests with $\tau_a = \tau_0$ and DSS tests with $\tau_a = 0$ as a function of fines content.
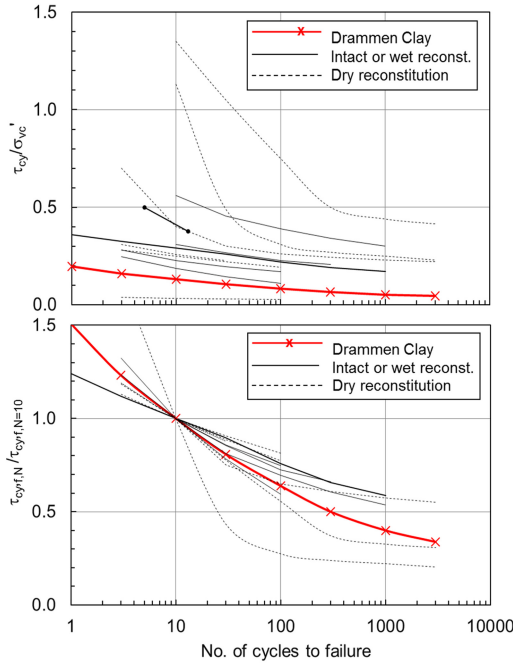
Figure 12.20. Cyclic shear stress at failure as a function of number of cycles in anisotropically consolidated triaxial tests with $\tau_0 = 0.21$ to $0.3 \cdot \sigma'_{vc}$ on normally consolidated sand and silt. $\sigma'_{vc} = 100$–710 kPa. Upper: $\tau_{cy,f}/\sigma'_{vc}$ vs. N_f. Lower: Normalized to $\tau_{cy,f}$ for $N = 10$ (Adapted from Andersen 2009).

Figure 12.21. Number of cycles to $\gamma \leq 3\%$ as a function of average and cyclic shear stresses. Triaxial tests on very dense Baskarp sand (Dr $\sim 96\%$, w $= 20\%$). $\sigma'_{vc} = 250$ kPa. Precycling: 400 cycles of $\tau_{cy}/\sigma'_{vc} = 0.1$ (Andersen & Berre 1999). Upper: Undrained $\Delta\tau_a$. Lower: Drained $\Delta\tau_a$, applied by increasing σ_v in compression and increasing σ_h in extension.

dilatant sand and weaker for loose contractive sand. On the extension side, however, the strength may be highest when $\Delta\tau_a$ is applied drained also for dense sand when $\Delta\tau_a$ is applied by increasing the normal stresses.

Figure 12.28 shows the effect of a failure strain criterion of 5% versus 10% for a sand with 65% relative density. The effect of failure strain criterion is most important when $\Delta\tau_a$ is applied undrained, and especially at large average shear strain in compression. There is also an effect of the failure strain criterion when the failure mode is large cyclic strains, but less significant than when the failure mode is large average shear strain. The effect of failure strain criterion increases with increasing relative density. For very high densities it can be essentially impossible to bring the tests to 15% shear strain.

12.3 Cyclic DSS shear strength of normally consolidated clay

12.3.1 Symmetrical cyclic loading ($\tau_a = 0$) and N = 10

Figure 12.29 shows the cyclic shear strength, normalized to σ'_{vc}, for 10 symmetrical stress controlled 10 s load cycles in DSS tests on normally consolidated clays as a function of consolidation stress. The curve for static shear strength of clay with plasticity index $I_p = 25\%$ is included for comparison (from Figure 10.5). The correlation of the normalized cyclic

shear strength with plasticity index is less clear than for the static shear strength, but there is an effect of consolidation stress on τ_f/σ'_{vc}, and an exponent of $n = 0.9$ seems to give the best fit, i.e. the same as for the static strength of clays and the cyclic strength of sand and silt.

The cyclic shear strength for 10 load cycles is normalized with respect to the reference stress and plotted as a function of the plasticity index in Figure 12.30. The cyclic shear strength increases with increasing plasticity index for a plasticity above $I_p = 22\%$, as for the static shear strength. There is also a tendency for the cyclic shear strength to increase with decreasing plasticity index below $I_p = 22\%$, also in line with the static shear strength. There are, however, four tests that show a lower cyclic shear strength for $I_p = 7$ to 12 %. At a lower plasticity indeces (e.g. below 15%) one should therefore also consider the cyclic shear strength correlations for sand and silt (Figures 12.1 and 12.2).

The ratio between cyclic and static shear strengths is plotted as a function of the plasticity index in Figure 12.31 for tests where there are pairs of static and cyclic tests on the same soil. The ratio decreases with decreasing plasticity index. Curve fitting gives the following best fit curve:

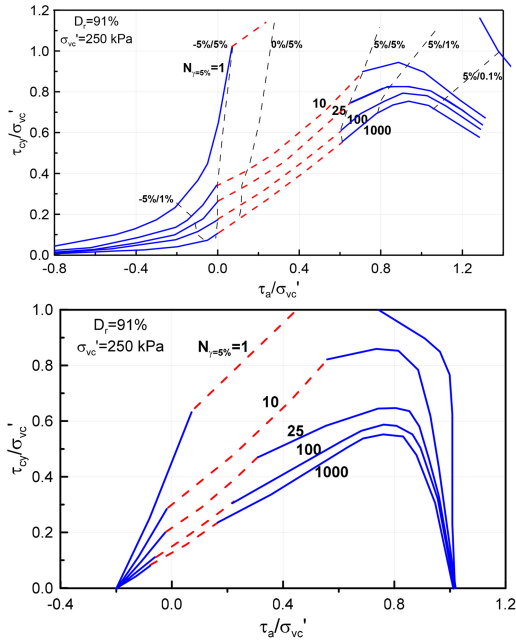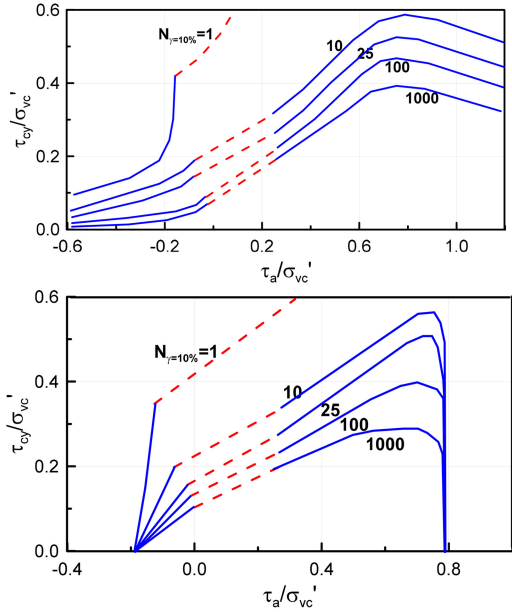$$(\tau_{f,cy} / s_u)^{DSS} = 0.41 \cdot I_p^{0.224}$$

Figure 12.22.   Number of cycles to $\gamma = 5\%$ as a function of average and cyclic shear stresses. Triaxial tests on Sand 3. $D_r \sim 91\%$. $w = 21\%$. $\sigma'_{vc} = 250$ kPa. Precycling: 400 cycles of $\tau_{cy}/\sigma'_{vc} = 0.1$. Upper: Undrained $\Delta\tau_a$. Lower: Drained $\Delta\tau_a$, applied by increasing σ_v in compression and decreasing σ_v in extension.

Figure 12.23.   Number of cycles to shear strain of 5% as a function of average and cyclic shear stresses. Triaxial tests on Sand 3. $D_r \sim 65\%$. $w = 26\%$. $\sigma'_{vc} = 250$ kPa. Precycling: 400 cycles of $\tau_{cy}/\sigma'_{vc} = 0.1$. Upper: Undrained $\Delta\tau_a$. Lower: Drained $\Delta\tau_a$, applied by increasing σ_v in compression and decreasing σ_v in extension.

12.3.2   *Effect of number of cycles*

The cyclic shear strength diagrams in Section 12.3.1 are for 10 load cycles. The cyclic shear strength for other number of cycles can be estimated by the curve for Drammen clay in Figure 12.5.

12.3.3   *Non-symmetrical cyclic loading ($\tau_a > 0$)*

A failure contour diagram for normally consolidated Drammen clay where $\Delta\tau_a$ is applied undrained was shown in Figure 7.1. The shear stresses are normalized to the undrained static shear strength. Similar diagrams for overconsolidated Drammen clay are given in Andersen (2004) and are not reproduced herein.

A collection of $N = 10$ failure contours for clays with different plasticity are presented in Figure 12.32. There is a tendency for the normalized cyclic shear strength to increase with increasing plasticity.

Situations with drained $\Delta\tau_a$ are generally less relevant for clays than for sand and silt. Nevertheless, drained $\Delta\tau_a$ can be important for slope stability under cyclic loading and is further discussed in Section 17.

12.4   *Cyclic triaxial shear strength of NC clay*

12.4.1   *Average shear stress different from initial shear stress ($\tau_a \neq \tau_0$) and $N = 10$*

Figure 7.2 shows a failure contour diagram for normally consolidated Drammen clay where $\Delta\tau_a$ is applied undrained. The shear stresses are normalized to the undrained static compression shear strength. Similar diagrams for overconsolidated Drammen clay are given in Andersen (2004) and are not reproduced herein.

A collection of $N = 10$ failure contours for clays with different plasticity are presented in Figure 12.33. There is a tendency for the normalized cyclic shear strength to increase with increasing plasticity. One should be aware, however, that these clays are from tests on offshore samples that are inherently more disturbed than Drammen clay, which was preconsolidated in the laboratory. As discussed in Section 9.1.1, sample disturbance can cause a greater reduction in compression strength than in extension strength. Since the data are normalized to the static compression strength, this can be part of the reason why the offshore clays plot higher than Drammen clay and for their higher ratio between extension and compression strengths. When using diagrams like the one in Figure 12.33, one should therefore denormalize with the compression strength from a test with the same quality as used to establish the curves in the diagram.

12.4.2   *Effect of number of cycles*

The cyclic shear strength in Figure 12.33 is for 10 cycles. The cyclic shear strength for other number of cycles can be estimated by the curve for Drammen clay in Figure 12.20.
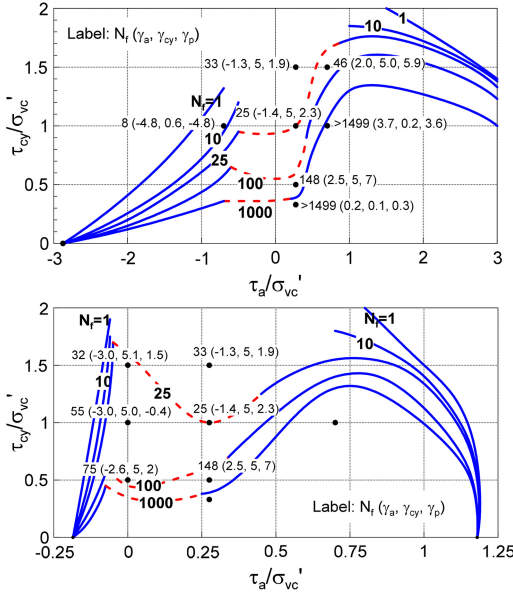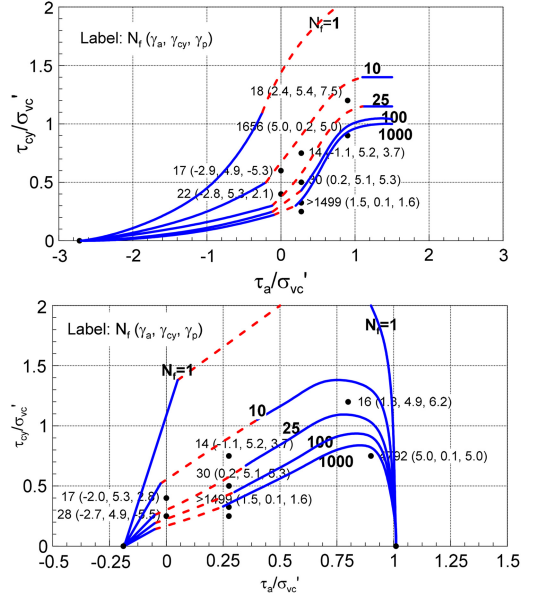
Figure 12.24. Number of cycles to failure as a function of average and cyclic shear stresses. Triaxial tests on normally consolidated very dense ($D_r \sim 97\%$, w = 23%) Dogger Bank sand with no fines (Blaker & Andersen 2015). $\sigma'_{vc} = 200$ kPa. Preshearing: 400 cycles at $\tau_{cy}/\sigma'_{vc} = 0.06$. Upper: Undrained $\Delta\tau_a$. Lower: Drained $\Delta\tau_a$, applied by increasing σ_v in compression and decreasing σ_v in extension.

Figure 12.25. Number of cycles to failure as a function of average and cyclic shear stresses. Triaxial tests on normally consolidated dense ($D_r \sim 80\%$, w = 24%) Dogger Bank sand with no fines (Blaker & Andersen 2015). $\sigma'_{vc} = 200$ kPa. Preshearing: 400 cycles at $\tau_{cy}/\sigma'_{vc} = 0.06$. Upper: Undrained $\Delta\tau_a$. Lower: Drained $\Delta\tau_a$, applied by increasing σ_v in compression and decreasing σ_v in extension.

12.5 Cyclic shear strength anisotropy

The difference in cyclic shear strength between triaxial and DSS for the case with $\Delta\tau_a = 0$ (i.e. $\tau_a = \tau_0$ in triaxial tests and $\tau_a = 0$ in DSS tests) was discussed in Section 12.2.1. However, the cyclic shear strength anisotropy will depend on the ratio between the cyclic shear stress and the change in average shear stress, $\tau_{cy}/\Delta\tau_a$.

One simplification that could be made to estimate the shear strength anisotropy is to assume that the ratio $\tau_{cy}/\Delta\tau_a$ is proportional to the ratio between cyclic and average loads. This will give the paths indicated by the full line in the DSS diagram and the dotted lines in the triaxial diagram in Figure 12.34. However, inspection of the shear strain combinations where the paths intersect the failure envelope will often show that the average and cyclic shear strains at failure are very different and that there will not be strain compatibility along a failure surface that involves compression, DSS and extension type elements. In order to achieve strain compatibility, both average and cyclic shear stresses need to be redistributed, and the stress paths will look more like the dotted curves in Figure 12.34. Andersen & Lauritzsen (1988) proposed a limiting equilibrium approach where this redistribution is accounted for. The method is briefly described in Section 18.1. More recently, a finite element code (UDCAM) has been developed where the stress path is calculated in each integration point based on the stress strain characteristics defined by contour diagrams of

the type presented in Figure 12.34 (Jostad et al., 2014) for different number of cycles, i.e. a diagram of the type presented in Figure 7.10. Another finite element code (PDCAM) also accounts for the pore pressure redistribution and dissipation during the cyclic load history (Jostad et al. 2015).

One way to make a rough estimate of cyclic strength anisotropy that may be reasonably realistic is to determine the strain combination for the stress path considered to be governing (e.g. DSS), and to determine the strength for the two other stress paths (e.g. compression and extension) for the strain combination at failure in DSS. Table 12.1 presents anisotropy ratios for the case with a change in average load, ΔP_a, equal to cyclic load ($\Delta P_a = P_{cy}$) for normally consolidated dense sand, silty sand and clay, assuming DSS to be the governing stress path with $\Delta\tau_a/\tau_{cy} = \Delta P_a/P_{cy}$. Strength anisotropy ratios for undrained monotonic loading are also included, as presented for sands and silty sands in Section 10.2, and for clays in Section 9.1.1.

The strength anisotropy ratio depends on whether $\Delta\tau_a$ is applied drained or undrained. In the case of drained $\Delta\tau_a$ the anisotropy ratio also depends on whether $\Delta\tau_a$ is applied by increasing or decreasing the normal stress in the triaxial test. The different cases are identified by U (undrained), by D $(+\sigma')$ when $\Delta\tau_a$ is applied drained by increasing the normal stress, and by D $(-\sigma')$ when $\Delta\tau_a$ is applied drained by decreasing the normal stress. The data for sand in Table 12.1 are for a shear strain of 5%, apart from the Baskarp sand
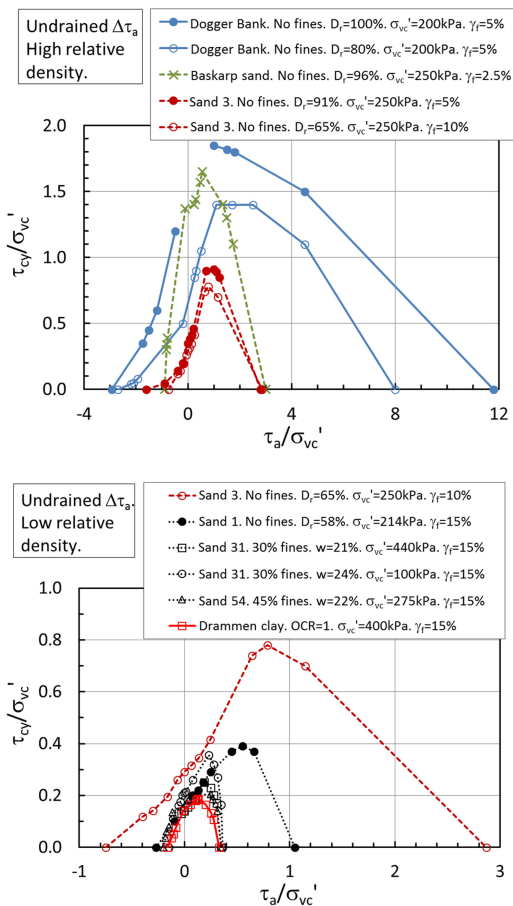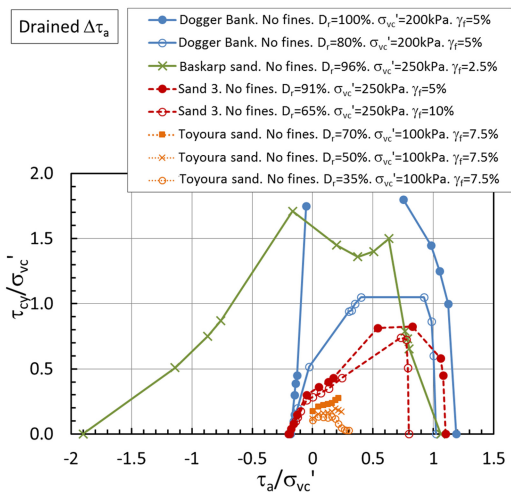
Figure 12.26. Average and cyclic shear stresses that give failure in 10 cycles in triaxial tests on different sands and silts. $\Delta\tau_a$ applied undrained. Upper: High density. Lower: Lower density.

Figure 12.27. Average and cyclic shear stresses that give failure in 10 cycles in triaxial tests on different sands and silts. $\Delta\tau_a$ applied drained by increasing σ'_{vc} in compression and decreasing σ'_{vc} in extension in all tests apart from Baskarp sand where σ'_{vc} was applied by increasing $\Delta\tau_a$ in extension.
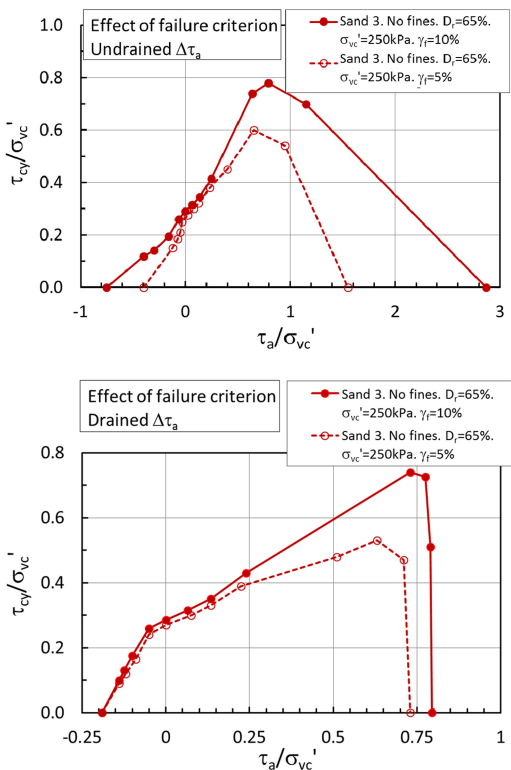
Figure 12.28. Effect of failure criterion on shear stresses that give failure in 10 cycles in triaxial tests on sands with $D_r = 65\%$ and w = 26%, Upper: Undrained $\Delta\tau_a$. Lower: Drained $\Delta\tau_a$.

where the shear strain is 3%. The reference cyclic DSS strength is with undrained or drained $\Delta\tau_a$, depending on which $\Delta\tau_a$-conditions are considered.

The data in Table 12.1 indicate that for dense sand and silty sand:

– The average of the triaxial compression and extension strengths is higher than the DSS strength, except when drained $\Delta\tau_a$ is applied by reducing the normal stress.

– The compression strength is typically more than twice the DSS strength, both for static and cyclic loading. The exception is when drained $\Delta\tau_a$ is applied by reducing the normal stress, although the anisotropy ratio still remains greater than 1.

– The extension strength is typically equal to or greater than the DSS strength for undrained static and cyclic loading, but there is significant variation around the average in some cases. The extension strength can be lower than the DSS strength, but the data are uncertain in this case.

Figure 12.29. Cyclic shear strength for 10 cycles with symmetrical stress controlled cyclic loading in DSS tests on normally consolidated clay ($>10\%$ clay content) as a function of consolidation stress.
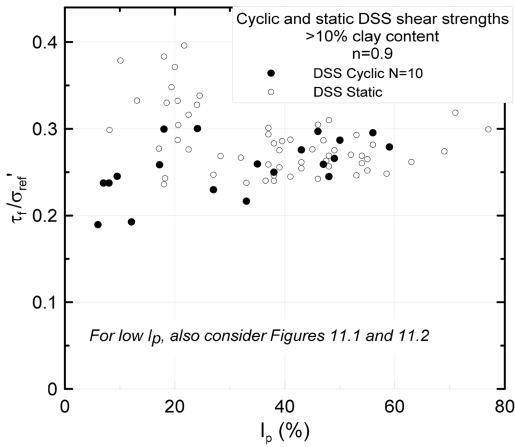
Figure 12.30. Cyclic shear strength for 10 cycles with symmetrical cyclic loading in DSS tests on normally consolidated clay ($>10\%$ clay content) as a function of plasticity index.
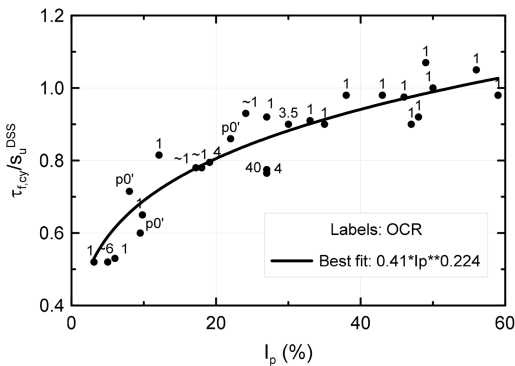
Figure 12.31. Ratio between cyclic and static shear strengths for 10 cycles with symmetrical cyclic loading in DSS tests on normally consolidated clay ($>10\%$ clay content) as a function of plasticity index.
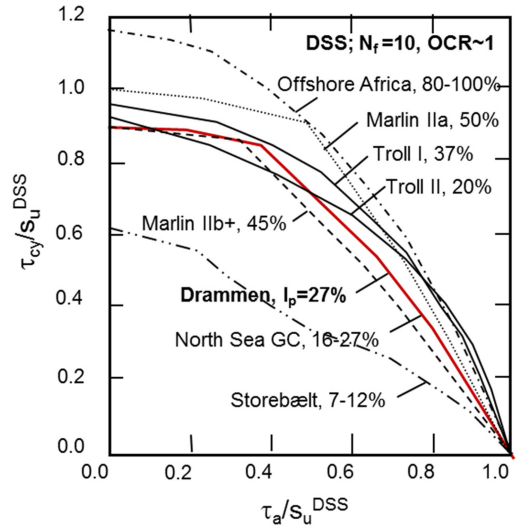
Figure 12.32. Combinations of average and cyclic shear stresses that cause failure in 10 cycles in DSS tests on different normally consolidated clays (based on Andersen 2004).
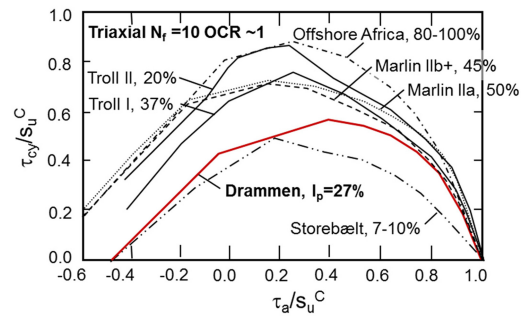
Figure 12.33. Combinations of average and cyclic shear stresses that cause failure in 10 cycles in triaxial tests on different normally consolidated clays (based on Andersen 2004).

– The extension strength is typically lower than the DSS strength in cases where the average shear stress, $\Delta\tau_a$, is applied drained by reducing the normal stresses and higher than the DSS strength in cases where $\Delta\tau_a$ is applied drained by increasing the normal stresses. However, there are no data for increasing normal stress for relative densities below $D_r = 80\%$.

– There are insufficient data to draw conclusions regarding the effect of OCR, but one set of data with clean sand at $D_r \sim 80\%$ (Dogger Bank with no fines and $D_r \sim 78\%$) seems to indicate that the ratio between extension and DSS increases with increasing OCR.

The data in Table 12.1 indicate that for clay:

– The anisotropy ratios are generally smaller than for sand, and the average of triaxial compression and extension strengths is close to the DSS strength.

50
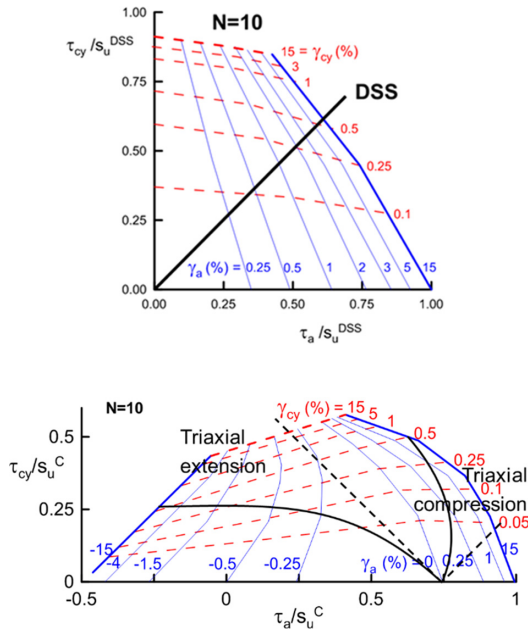
Figure 12.34. Example of stress paths in contour diagrams assuming 1) the ratio $\tau_{cy}/\Delta\tau_a$ is the same for DSS, compression and extension (full line in DSS, dotted curves in triaxial), and 2) that strain combination at failure in triaxial is same as in DSS (full curves). Example assumes $\tau_{cy}/\Delta\tau_a = 1:1$.

– Anisotropy increases with increasing sample quality (higher triaxial compression to DSS ratio and lower triaxial extension to DSS ratio).
– The anisotropy ratios for static loading are about the same for OCR of 1 and 4 (Drammen clay). For cyclic loading, the anisotropy ratio for Drammen clay is apparently independent of OCR for compression, but for extension it increases to 0.7 for OCR = 4 and to 0.85 for OCR = 40.

It may be reasonable to assume that the anisotropy ratios for loose sand and silt will be similar to clay, and that the anisotropy ratios for medium dense sand and silt will be between those for dense and loose sand.

The anisotropy ratios did not show any systematic variation with number of cycles.

Strength anisotropy ratios as presented above, especially those for sand and silty sand, can have significant influence on the failure mechanism and the capacity of a foundation, and should be given attention in design.

12.6 *Effect of preshearing*

Soils are often subjected to preshearing, i.e. small cyclic shear stresses accompanied by drainage, in the field prior to the main design event. Preshearing will influence the undrained cyclic shear strength of a soil and should be considered for the laboratory tests, as discussed in Section 9.1.2, in cases where preshearing is expected to occur or have occurred in situ.

Table 12.1. Anisotropy ratios for normally consolidated dense sand, silty sand and clay for conditions in Fig. 12.34. Static and cyclic loading and different drainage conditions. (Numbers are average values with max. and min. values in brackets).

	Triaxial comp/DSS		Triaxial ext/DSS	
Drainage	Sand	Clay	Sand	Clay
-Static-				
U	$\sim 5^a$	$1.25^c/1.45^b$	$\sim 1 - \sim 1.1^a$	$0.61^b/0.78^c$
-Cyclic $\Delta\tau_a = \tau_{cy}$ in DSS and strain compatibility-				
U	2.0	1.35^d	1.34	0.6^d
	(1.6–2.3)		$(0.6^e$–2.0)	
D	2.5	–	1.5	–
$(+\sigma')$	(2.0–3.5)		$(1.0^f$-1.8)	
D	1.5	–	0.6	–
$(-\sigma')$	(1.1–1.8)		(0.4–0.75)	

U: undrained; D: drained
$(+\sigma')$: $\Delta\tau_a$ applied by increasing σ_v' or σ_h'
$(-\sigma')$: $\Delta\tau_a$ applied by decreasing σ_v' or σ_h'
a) Section 10.2; b) High quality specimens (Table 9.1); c) Offshore samples (Table 9.1); d) Drammen clay; e) Values <1 are for sand where DSS data is uncertain; f) Uncertain data

Figure 12.35 shows how the undrained cyclic shear strength for 10 load cycles depends on the degree of preshearing, defined by normalized cyclic shear stress, τ_{cy}/σ_{vc}', and number of cycles during preshearing. The figure contains DSS, shaking table and triaxial tests subjected to various degrees of preshearing. Grain size characteristics for the different soils are presented in Table 7.1.

In DSS tests, the preshearing may:

– improve the seating between the sand and the horizontal end plates
– level out stress concentrations from the consolidation
– increase the horizontal effective stress
– change the soil structure

The volume reduction is generally small during preshearing, and the increase in density is alone by far not enough to explain the increased cyclic resistance. One might expect preshearing to have less effect in triaxial tests than in DSS tests, since seating and stress concentrations are likely to be less important and the horizontal stress is kept constant in triaxial tests.

The data in Figure 12.35 show that:

– the cyclic shear stress at failure increases with increasing preshearing, i.e. both with increasing cyclic shear stress and increasing number of cycles during preshearing
– preshearing has an important effect for both low and high relative density. No clear trend is observed as a function of D_r.
– the data does not show clear differences between triaxial and DSS tests, but there are less data with preshearing in triaxial than in DSS tests.
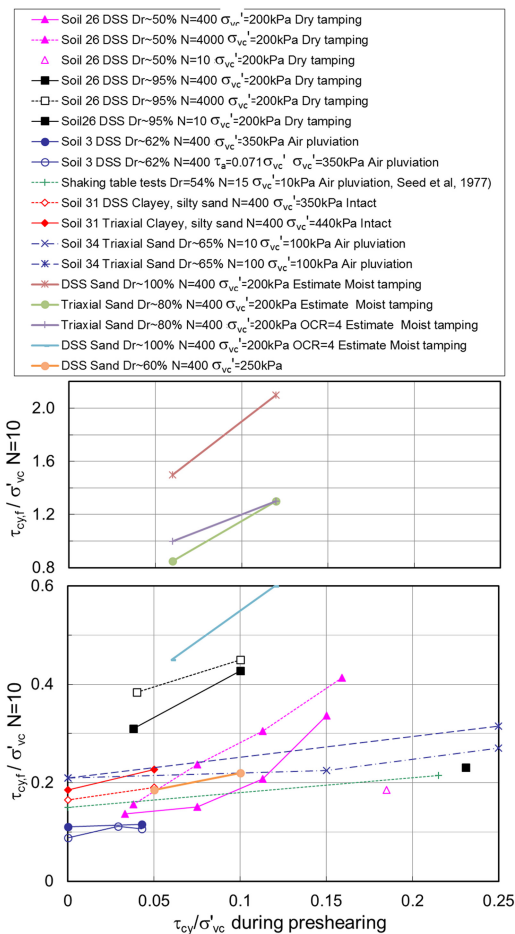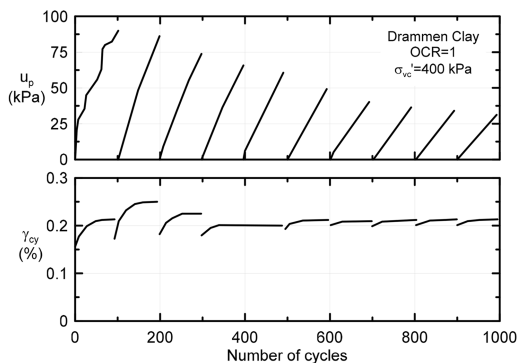
Figure 12.36. Permanent pore pressure and cyclic shear strain during consecutive series of undrained cyclic loading with drainage between the series. DSS tests on normally consolidated Drammen clay (based on Andersen 1988).
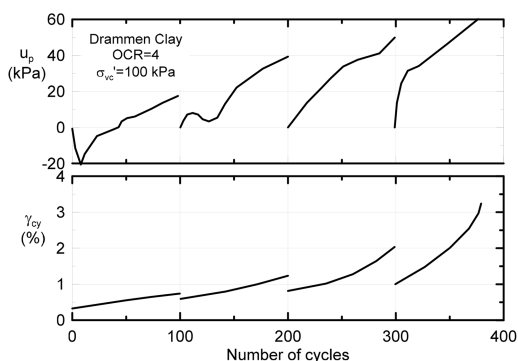

Figure 12.37. Pore pressure and cyclic shear strain during consecutive series of undrained cyclic loading with drainage between the series. DSS tests on overconsolidated Drammen clay (OCR = 4) (based on Andersen 1988).

Figure 12.35. Effect of preshearing on undrained cyclic shear stress at failure in triaxial and DSS tests on sand and silty sand.

– preshearing with 400 cycles at $\tau_{cy}/\sigma'_{vc} = 0.04$ may give a cyclic shear strength increase between about 5 and 25% compared to no preshearing.

The effect of preshearing may be the opposite of what is presented above if the preshearing causes large shear strains that may break down the structure, e.g. Oda et al. (2001) and Wijewickreme & Sanin (2005).

Most of the data in Figure 12.35 are for normally consolidated soil. Preshearing may give less positive effects on overconsolidated soil. Cyclic tests on Drammen clay show that preshearing with 100 cycles at a cyclic shear stress of half the static shear strength gives an increased resistance to subsequent undrained cyclic loading in normally consolidated clay (Figure 12.36), but a reduced resistance in clay with an over-consolidation ratio of 4 (Figure 12.37). The data in Figures 12.36 and 12.37 show that the pore pressure and the cyclic shear strain decrease after each series of undrained cyclic loading and drainage in the normally consolidated clay, but increases in the overconsolidated clay.

The effect of preshearing is further illustrated in Figure 12.38, which shows the effect of preshearing on the static and cyclic shear strengths in DSS tests on Drammen clay with OCR of 1, 4 and 10. Most of the tests had a moderate preshearing with 10 times 100 undrained cycles with drainage after each series of 100 cycles at $\tau_{cy}/s_u = 0.12$ to 0.175. The results show that the preshearing increased the strengths for clay with OCR=1 and decreased the strengths for clay with OCR = 10. Stronger preshearing tended to give more effect, as shown in Figure 12.38. The preshearing and the cyclic strength tests were run with symmetrical cyclic loading, i.e. $\tau_a = 0$. The cyclic strengths were determined from tests that failed after about 200 cycles.

An overconsolidated clay may thus become less capable to withstand the design storm and may get a reduced stiffness if it is subjected to previous storms and time for drainage before the main design event. Similar effects of overconsolidation may also exist for cohesionless soil, but no data have been available for overconsolidated sand.

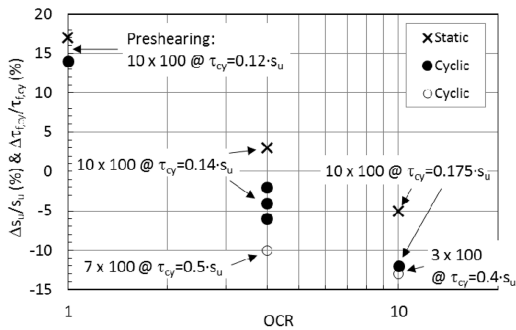The negative effect of preshearing in overconsolidated clay should therefore be considered, especially

Figure 12.38. Effect of preshearing with drainage on static and cyclic undrained DSS shear strengths of Drammen clay.

for design of monopiles and driven piles, as the weakening may reduce both stiffness and capacity. The effect will be less severe for gravity structures, as they are normally designed without drawing on the effective stress increase from consolidation under the platform weight. The weakening due to preshearing will therefore be counteracted by the effective stress increase from the platform weight with time.

12.7 *Effect of OCR*

The cyclic shear strength diagrams in the preceding sections are for normally consolidated soil. However, the in situ soil can be overconsolidated due to removal of previous overburden, variation in platform weight, or preloading by temporary weight or underpressure. The soil can also have an apparent overconsolidation due to long term secondary consolidation, as demonstrated for clays by Bjerrum (1967). Similar effects with creep leading to an apparent preconsolidation are also observed in sand, as illustrated in the oedometer test in Figure 16.1. If additional normal effective stresses that exceed the preconsolidation stress are added, like for instance due to the weight of a platform, the soil will become normally consolidated again. The time to generate a new apparent preconsolidation due to secondary consolidation will then be limited, but may still be important. Overconsolidation will increase the horizontal effective normal stress, increase the relative density and possibly change the soil structure. These changes will tend to increase both static and cyclic soil strength. The effect of OCR on static shear strength was discussed in Section 10.5.

The effect of overconsolidation on the cyclic shear stress at failure, $\tau_{cy,f}$, is compiled in the upper diagram in Figure 12.39 for the four soils that were considered for static shear strength (Figure 10.7). The cyclic data consist of DSS data with $\tau_a = 0$, apart from one CAU case. An empirical equation from Ishihara & Takatsu (1979) based on cyclic torsional tests on loose sand is also included. The equation is applied by assuming K_0 of 0.5, 0.7, 1.0 and 1.35 for OCR = 1, 2, 4 and 8, respectively. The results show that:

– The cyclic shear strength follows the same trend as the static shear strength, with effect of OCR being
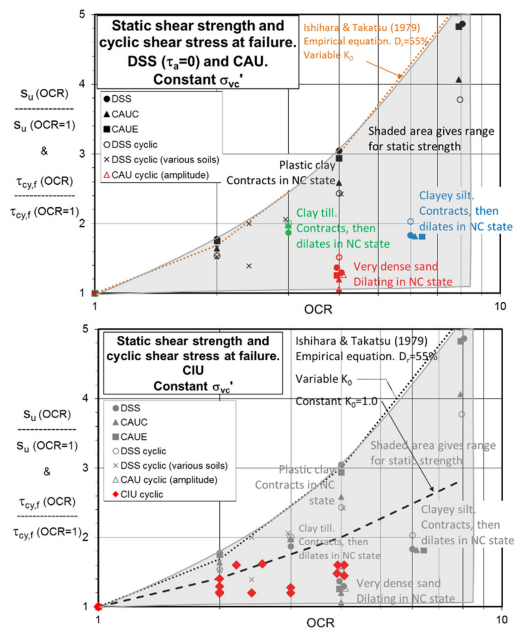
Figure 12.39. Undrained cyclic shear strength as a function of OCR. Upper: DSS ($\tau_a = 0$) and CAU triaxial tests; Lower: CIU triaxial tests.

significantly smaller for soils that dilate than for soils that contract under monotonic loading in the normally consolidated state. There is a tendency, however, for the difference between contractive and dilative soils to be somewhat smaller for cyclic than for static strength.

– The empirical equation confirms the data for contractive soils.

Additional DSS data are included (with different symbols) in addition to the data for the four soils considered for static shear strength. These data have dilative behavior between the plastic clay and the very dense sand, and plot between these soils, as expected.

As for the static strength in Figure 10.7, the diagram in Figure 12.39 is valid for the condition where the variation in OCR is generated by varying the preconsolidation stress, whilst keeping the consolidation stress the same. To go from a constant consolidation stress to a constant preconsolidation stress, the vertical axis in Figure 12.39 shall be multiplied with OCR^{n-1}. For cyclic shear strengths, $n = 0.9$ is used for both sand and clay, as determined in Sections 12.1 and 12.3, respectively.

Data for cyclic CIU triaxial tests are presented in the lower diagram in Figure 12.39. The empirical equation from Ishihara & Takatsu (1979) is also included, this time assuming $K_0 = 1.0$ for all OCRs to match the CIU triaxial conditions. Both the test data and the empirical equations indicate that the effect of OCR is smaller for CIU triaxial tests than for DSS tests.

Examples showing the effect of OCR on cyclic shear strength for $\tau_a > 0$ are presented in Figure 12.40.
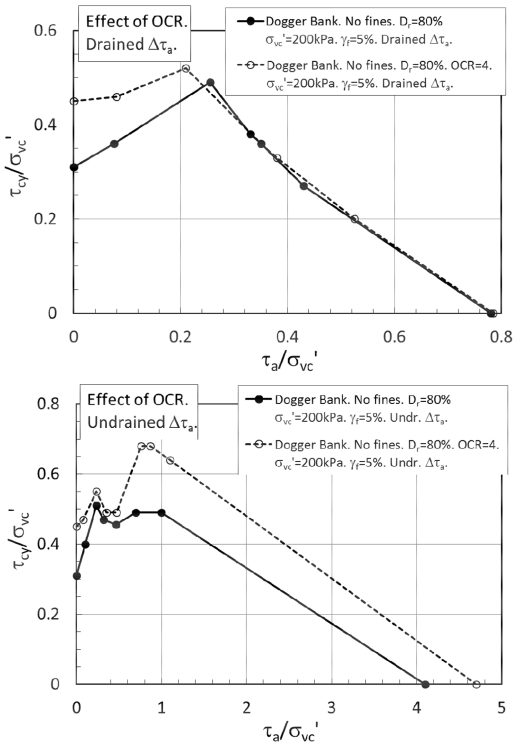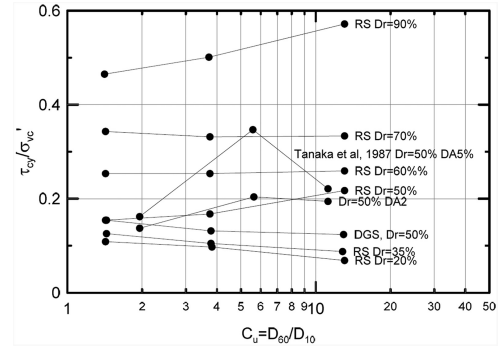
Figure 12.41.   Undrained cyclic shear stress to cause cyclic failure after 20 cycles in triaxial tests on river sand/gravel (RS) and decomposed weathered granite (DGS) with various relative densities as a function of uniformity coefficient, $C_u = D_{60}/D_{10}$ (based on Kokusho et al. 2004).

Figure 12.40.   Effect of OCR on cyclic shear strength in DSS tests on clean sand with $D_r \sim 80\%$. N = 10. Upper: Drained $\Delta\tau_a$. Lower: Undrained $\Delta\tau_a$.

In the case with drained $\Delta\tau_a$, the intersection with the horizontal axis is governed by the drained shear strength, and there is no effect of OCR when failure is due to large average shear strains. For undrained $\Delta\tau_a$, however, the cyclic shear strength increases with increasing OCR when failure is due to large average shear strain. This is due to the dilatancy that occurs when the soil is subjected to average shear strains under undrained conditions.

12.8   Gravel

Coarser grained soils will in practice be less susceptible to pore pressure generation and reduction in shear strength due to cyclic loading than finer soils, since their higher permeability allows more drainage. However, case records of earthquake liquefaction failures show that not only sand and silt but also gravelly soils can liquefy, no matter how coarse they may be and whether they are well graded or not (e.g. Kokusho et al. 2004). Even gravelly soils are therefore susceptible to strength degradation or liquefaction if the drainage conditions are poor, for instance beneath large structures or if the coarse layer is confined by less permeable soil.

Various studies with triaxial testing on coarse grained soils with different coefficients of uniformity, $C_u = D_{60}/D_{10}$, reported in the literature are inconclusive with respect to effect of C_u on cyclic

strength. They seem to indicate that the undrained cyclic strength is either not influenced or increases with increasing C_u. As shown in Figure 12.41, Kokusho et al. (2004) found that the cyclic shear strength (defined as $\gamma_{cy} = 3.75\%$) was barely influenced by C_u in the range 1.44 to 13.1 for a given relative density. Siddiqi (1984) found for Lake Valley Gravel and Oroville Gravel that removal of gravel particles did not change the cyclic strength. In contradiction to Kokusho et al. (2004) and Siddiqi (1984), Evans & Zhow (1995) show that the resistance to cyclic loading increases with increasing gravel content (up to 60% gravel content) after correcting for membrane compliance. Previous literature (Wong et al. 1975, Tanaka et al. 1987) with cyclic triaxial testing, reports that gravelly soils are more resistant to cyclic loading than sand. This may, however, be due to membrane compliance, which was not corrected for in these studies.

Kokusho et al. (2004) found that the post cyclic undrained static strength was more than 8 times larger for well graded than for poorly graded material with the same relative density. This was explained by differences in dilatancy, with undrained cyclic stress-strain behavior of poorly graded gravel being less dilative at large displacements than well graded gravel.

Laboratory testing on gravelly soils has mainly been done in the traxial apparatus on samples that have been isotropically consolidated. Available test results are mainly for well graded soils, representing in situ materials. This also presents fewer problems with membrane compliance in the laboratory. There is little data about cyclic strength from DSS tests on more uniform gravel.

Laboratory tests on coarse grained soils can be difficult to perform in standard laboratory equipment due to the content of large grain sizes. Based on the results above, however, it seems that undrained cyclic tests can be performed with a modified grain size distribution where the larger grains are removed. The relative density, angularity and mineralogy should be the same as for the gravel.
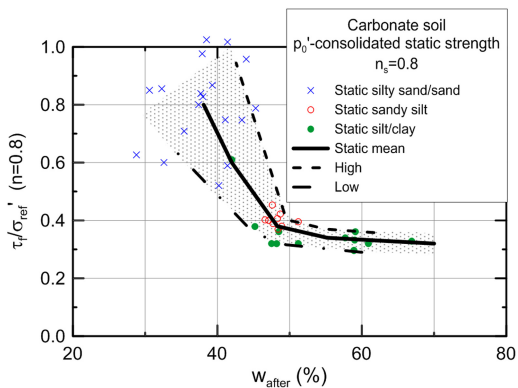
Figure 12.42. Static DSS shear strength of p_0'-consolidated non-cemented carbonate soils as a function of water content.
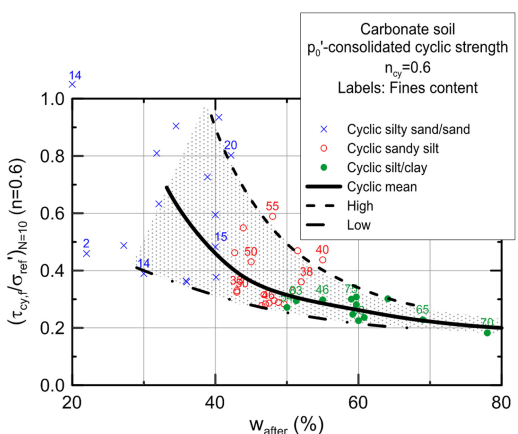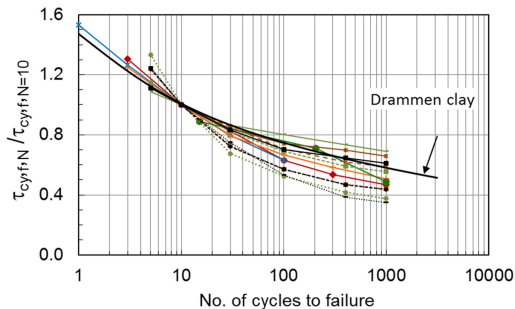

Figure 12.44. Cyclic shear strength of p_0'-consolidated non-cemented carbonate soils in DSS tests with $\tau_a = 0$ as a function of number of cycles. Normalized to number of cycles to failure in 10 cycles.

N	X_0	X_1	Y_1	X_2	Y_2
5	From	0.075	From Figs.	$0.4 \cdot X_0$	$0.67 \cdot Y_1$
10	Fig.	0.05	12.43 &	$0.33 \cdot X_0$	$0.6 \cdot Y_1$
100	12.42	0.025	12.44	$0.25 \cdot X_0$	$0.5 \cdot Y_1$
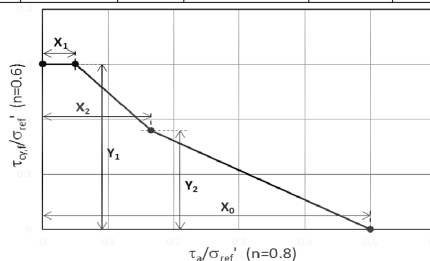
Figure 12.45. Approximate cyclic shear stress to failure in DSS tests on p_0'-consolidated non-cemented carbonate soils as a function of τ_a.

Figure 12.43. Cyclic shear strength of p_0'-consolidated non-cemented carbonate soils in DSS tests with $\tau_a = 0$ as a function of water content.

12.9 *Carbonate soils (non-cemented)*

This paper concentrates on non-carbonate soils. Carbonate soils may, due to their origin, behave differently and require special attention. This section attempts a rough estimate of the DSS shear strength of non-cemented carbonate soils in terms of the contour diagram concept. The interpretation is limited to undrained shear strength of soils consolidated to the in situ vertical effective overburden stress, p_0'. The deposits have not carried a higher overburden previously, but may have some apparent overconsolidation due to creep and some light cementation.

The static shear strength is presented as a function of water content after consolidation in Figure 12.42. The cyclic shear strength for 10 cycles with symmetrical cyclic loading is presented in Figure 12.43. The shear strengths are normalized to the reference stress, σ_{ref}', with an exponent $n = 0.8$ for static strength and $n = 0.6$ for cyclic strength. These exponents were found to give least dependence on consolidation stress. Soils with a range of grain size distributions are included.

The data for water content less than about 45% relates mainly to sand, mud for water content above about 52%, and silt in between. There is significant scatter in the data, but still a clear trend. The scatter is greatest for coarser grained soil. The exponent $n = 0.6$ for cyclic strength, is lower than for non-carbonate soils ($n = 0.9$), indicating that the cyclic shear strength of carbonate soils depends more on the consolidation stress than non-carbonate soils.

The cyclic shear strengths for different numbers of cycles are shown in Figure 12.44. The trend is similar to the trend for non-carbonate sands and silts in Figure 12.5 and somewhat more affected by number of cycles than Drammen clay. There is no clear difference between the different soil types.

The approximate effect of average shear stress $\tau_a > 0$ can be estimated from the diagram in Figure 12.45. The shape of the curve is uncertain and may be conservative for muds.

The diagrams are established based on literature (Finnie et al. 1999) and NGI's experience with carbonate soils from consulting projects. A large part of the data are reinterpreted from simple shear tests performed at UWA.

13 CYCLIC STRESS STRAIN CHARACTERISTICS

13.1 *Cyclic shear strain as a function of N in DSS tests on normally consolidated sand and silt.*

Figure 13.1 presents contours of cyclic shear strain as a function of cyclic shear stress and number of cycles in DSS tests with $\tau_a = 0$ on normally consolidated sand and silt. The contours are based on interpolation and extrapolation of data from various sands and silts in NGI's data base. This involves considerable uncertainty, and the contours should be regarded as estimates.

The diagrams are given for different values of $(\tau_{cy,f}/\sigma'_{ref})_{N=10}$ for $\tau_a = 0$ and can be related to relative density and water content through the diagrams for cyclic shear strength in Figures 12.1 and 12.2. The exponent in the reference stress used for normalization is consistent with the values established in Section 12.1.1, i.e. n = 0.9. Contours for the same conditions are presented for cyclic shear strength in Figures 12.15 and 12.16, for average and cyclic shear strain contours in Figures 13.2 to 13.11 and for pore pressure in Figure 14.1.

13.2 *Shear strains in DSS tests on normally consolidated sand and silt.*

Figures 13.2 to 13.11 present contours of average and cyclic shear strains as functions of average and cyclic shear stresses for normally consolidated sand and silt for N = 1, 10 and 100. These contours are based on interpolation and extrapolation of data from various sands and silts in NGI's data base. This involves considerable uncertainty, and the contours should be regarded as estimates. Figures 13.2 to 13.6 are valid for undrained τ_a. Figures 13.7 to 13.11 are valid for drained τ_a.

The exponents in the reference stress used for normalization are consistent with the values established in Sections 12.1.1 and 10.1; i.e. n = 0.9 for τ_{cy} on the vertical axis and n = 0.1 for undrained τ_a on the horizontal axis (Figures 13.2 to 13.6). n = 0.9 is used for drained τ_a on the horizontal axis in Figures 13.7 to 13.11, giving an intersection of the failure curves with the horizontal axis, reasonably consistent with the drained static shear strength based on the drained failure envelope angles, α', in Figure 10.10.

The diagrams are given for different values of $(\tau_{cy,f}/\sigma'_{ref})_{N=10}$ for $\tau_a = 0$ and can be related to relative density and water content through the diagrams for cyclic shear strength in Figures 12.1 and 12.2.

Cyclic strain contours for the same conditions are presented in Figure 13.1, pore pressure contours in Figure 14.1, and cyclic shear strength contours in Figures 12.15 and 12.16.

13.3 *Shear strains as functions of N in triaxial tests on normally consolidated sand and silt.*

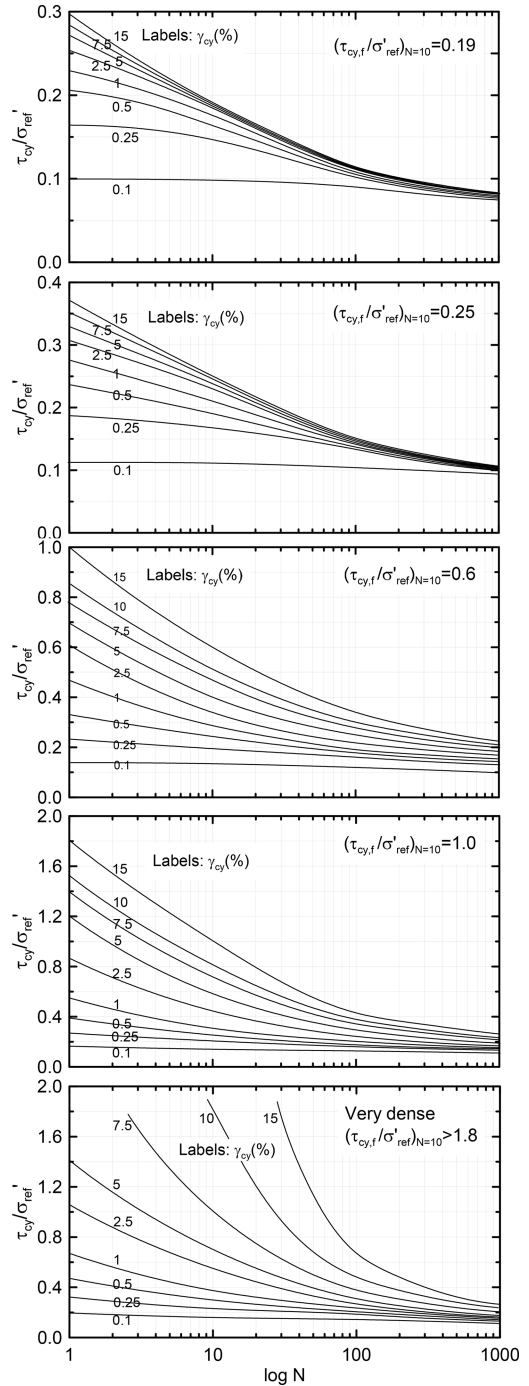Figures 13.12 to 13.14 present examples of average and cyclic shear strain contour diagrams from

Figure 13.1. Cyclic strain contours for DSS tests with $\tau_a = 0$ on normally consolidated sand and silt with different $(\tau_{cy,f}/\sigma'_{ref})_{N=10}$.

triaxial tests on 3 normally consolidated clean sands with average shear stress $\tau_a = \tau_0$. The density varies from $D_r = 65\%$ to $\sim 100\%$. The results show that the sand dilates less and becomes softer with decreasing density.
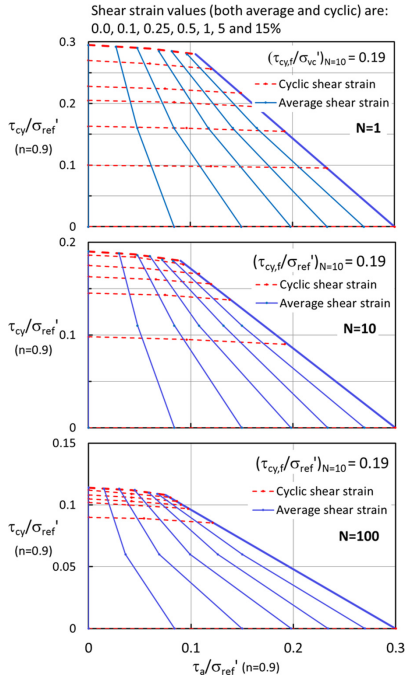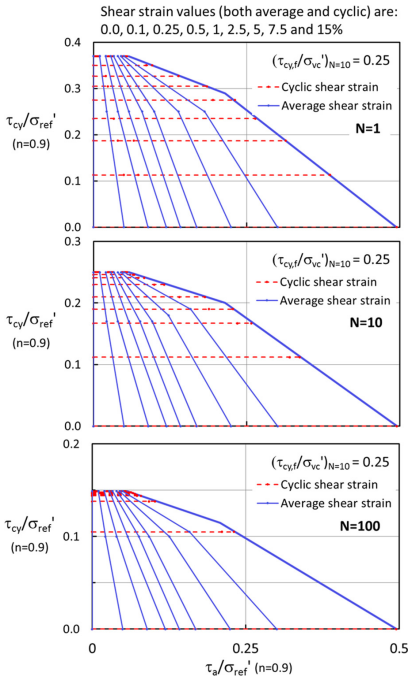
Figure 13.2. Average and cyclic shear strains as functions of average and cyclic shear stresses and number of cycles for sand with <5% fines with $(\tau_{cy,f}/\sigma'_{ref})_{N=10} = 0.19$. τ_a applied undrained.
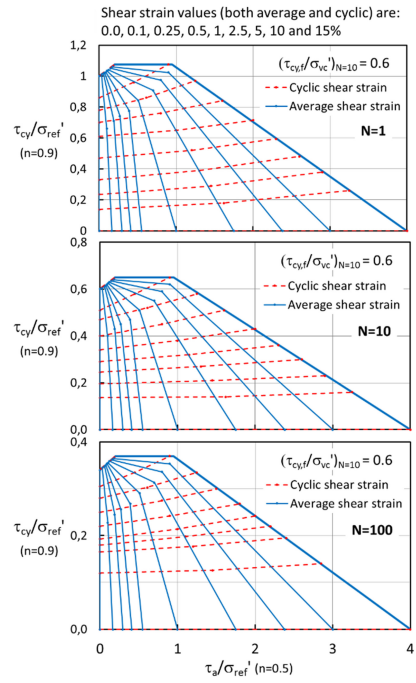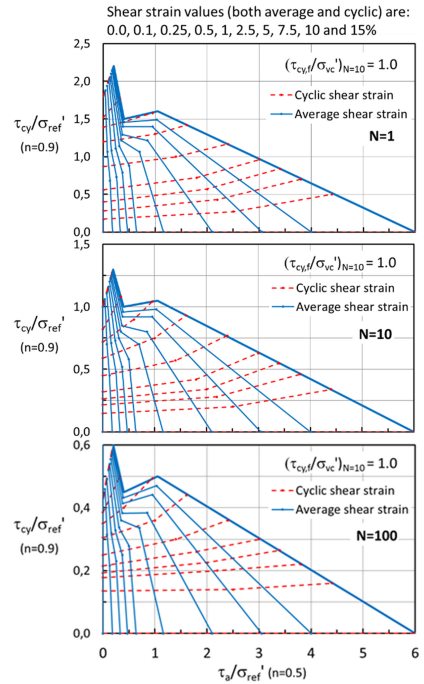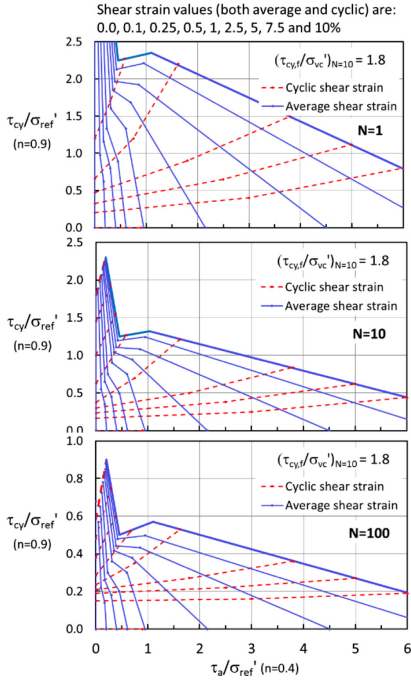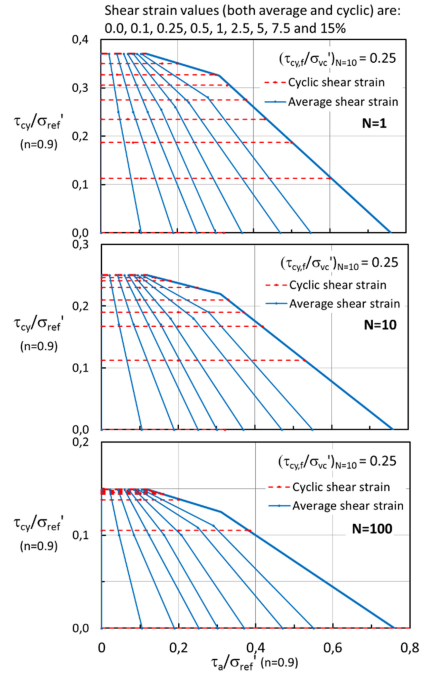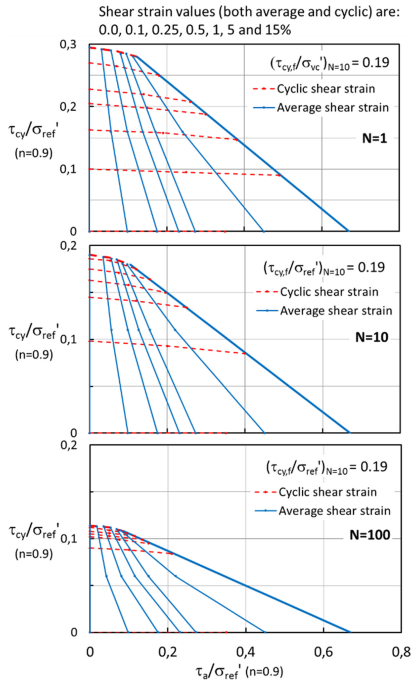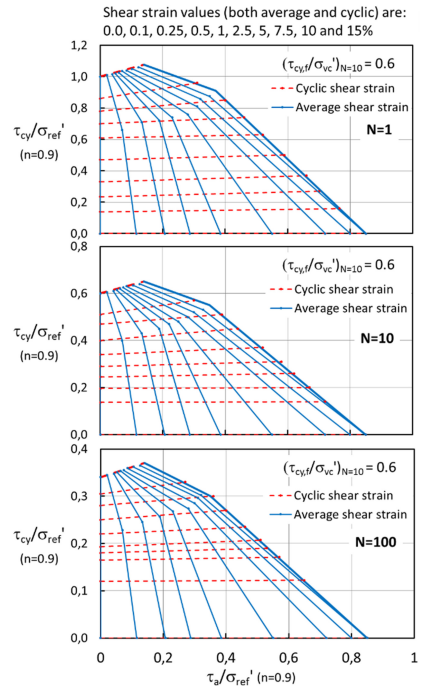

Figure 13.4. Average and cyclic shear strains as functions of average and cyclic shear stresses and number of cycles for sand and silt with $(\tau_{cy,f}/\sigma'_{ref})_{N=10} = 0.6$. τ_a applied undrained.

Figure 13.3. Average and cyclic shear strains as functions of average and cyclic shear stresses and number of cycles for sand with <5% fines with $(\tau_{cy,f}/\sigma'_{ref})_{N=10} = 0.25$. τ_a applied undrained.
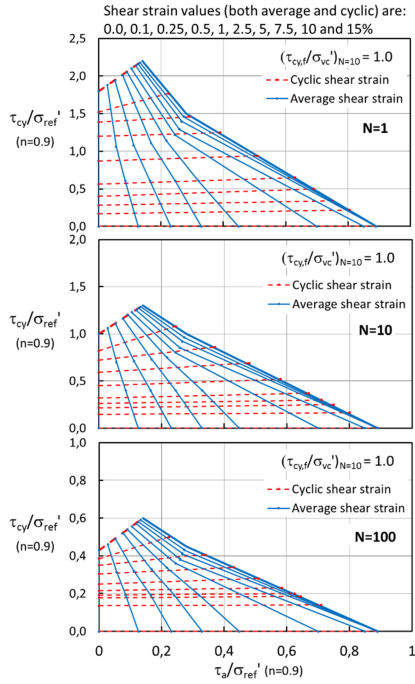

Figure 13.5. Average and cyclic shear strains as functions of average and cyclic shear stresses and number of cycles for sand and silt with $(\tau_{cy,f}/\sigma'_{ref})_{N=10} = 1.0$. τ_a applied undrained.
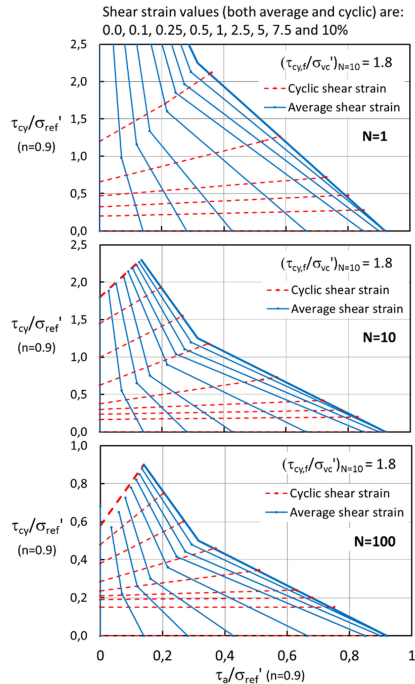
57

Figure 13.6. Average and cyclic shear strains as functions of average and cyclic shear stresses and number of cycles for sand and silt with $(\tau_{cy,f}/\sigma'_{ref})_{N=10} = 1.8$. τ_a applied undrained.

Figure 13.8. Average and cyclic shear strains as functions of average and cyclic shear stresses and number of cycles for sand and silt with $(\tau_{cy,f}/\sigma'_{ref})_{N=10} = 0.25$. τ_a applied drained.
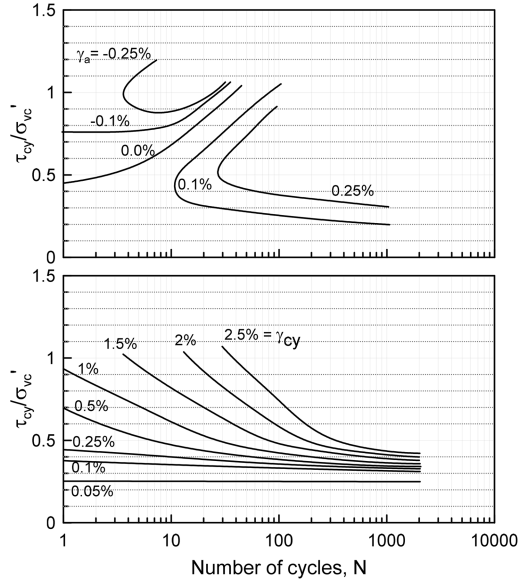

Figure 13.7. Average and cyclic shear strains as functions of average and cyclic shear stresses and number of cycles for sand and silt with $(\tau_{cy,f}/\sigma'_{ref})_{N=10} = 0.19$. τ_a applied drained.

Figure 13.9. Average and cyclic shear strains as functions of average and cyclic shear stresses and number of cycles for sand and silt with $(\tau_{cy,f}/\sigma'_{ref})_{N=10} = 0.6$. τ_a applied drained.

Figure 13.10. Average and cyclic shear strains as functions of average and cyclic shear stresses and number of cycles for sand and silt with $(\tau_{cy,f}/\sigma'_{ref})_{N=10} = 1.0$. τ_a applied drained.

Figure 13.11. Average and cyclic shear strains as functions of average and cyclic shear stresses and number of cycles for sand and silt with $(\tau_{cy,f}/\sigma'_{ref})_{N=10} = 1.8$. τ_a applied drained.

Figure 13.12. Average (upper) and cyclic (lower) shear strains as functions of number of cycles and cyclic shear stress for $\tau_a/\sigma'_{vc} = \tau/\sigma'_{v,c} = 0.25$. Triaxial tests on Baskarp sand. $D_r \sim 98\%$. $w = 20\%$. $\sigma'_{vc} = 250$ kPa. Precycling: 400 cycles of $\tau_{cy}/\sigma'_{vc} = 0.1$. Samples prepared by pluviation.
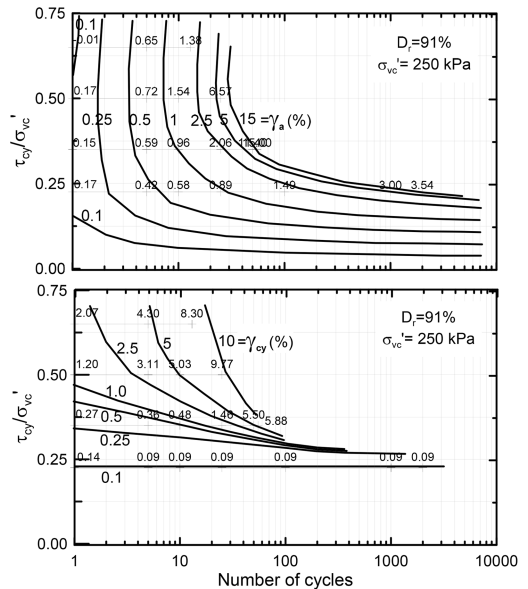
Figure 13.13. Average (upper) and cyclic (lower) shear strains as functions of N and τ_{cy}/σ'_{vc} for $\tau_a/\sigma'_{vc} = \tau/\sigma'_{vc} = 0.25$ in triaxial tests on Sand 3. $D_r \sim 91\%$ $w = 21\%$. $\sigma'_{vc} = 250$ kPa. Precycling: 400 cycles of $\tau_{cy}/\sigma'_{vc} = 0.1$. Prepared by pluviation.
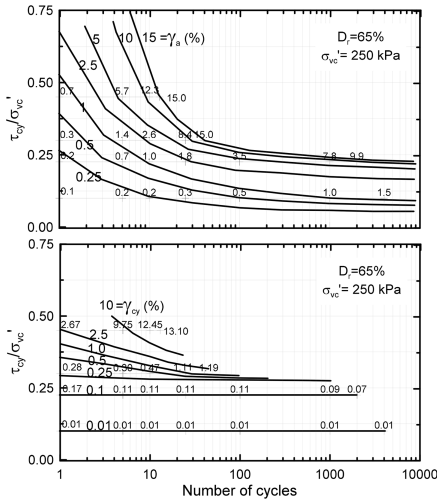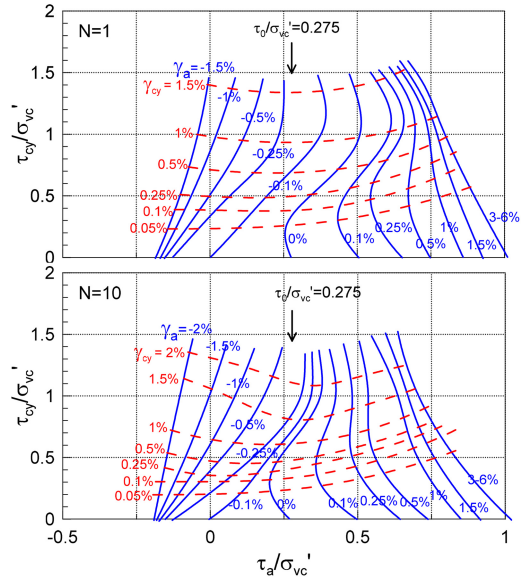
Figure 13.14. Average (upper) and cyclic (lower) shear strains as functions of N and τ_{cy}/σ'_{vc} for $\tau_a/\sigma'_{vc} = \tau/\sigma'_{vc} = 0.25$ in triaxial tests on Sand 3. $D_r \sim 65\%$ w = 26%. $\sigma'_{vc} = 250$ kPa. Precycling: 400 cycles of $\tau_{cy}/\sigma'_{vc} = 0.1$. Prepared by pluviation.
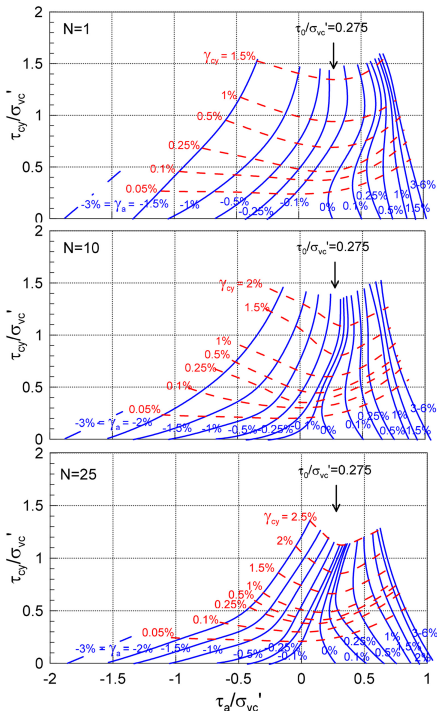

Figure 13.15. Average and cyclic shear strains as functions of average and cyclic shear stresses in triaxial tests on Baskarp Sand. $D_r \sim 96\%$. w = 20%. $\sigma'_{vc} = 250$ kPa. Precycling: 400 cycles of $\tau_{cy}/\sigma'_{vc} = 0.1$. $\Delta\tau_a$ applied drained by increasing vertical stress in compression and increasing the horizontal stress in extension. Upper: N = 1. Middle: N = 10. Lower: N = 25.

Figure 13.16. Average and cyclic shear strains as functions of average and cyclic shear stresses in triaxial tests on Baskarp Sand. $D_r \sim 96\%$. w = 20%. $\sigma'_{vc} = 250$ kPa. Precycling: 400 cycles of $\tau_{cy}/\sigma'_{vc} = 0.1$. $\Delta\tau_a$ applied drained by increasing the vertical stress in compression and decreasing the vertical stress in extension. Estimated extension side. Upper: N = 1. Lower: N = 10.

Cyclic shear strength contours for the same sands are presented in Figures 12.21 to 12.25, additional average and cyclic strain contours in Figures 13.15 to 13.21, and pore pressure contours in Figures 14.2 to 14.10.

13.4 *Shear strains in triaxial tests on normally consolidated sand and silt.*

Figures 13.15 to 13.21 present average and cyclic shear strains as functions of average and cyclic shear stresses for different values of N for three normally consolidated clean sands. The density varies from $D_r = 65\%$ to $\sim 100\%$. Grain size characteristics for the different soils are presented in Table 7.1. Separate diagrams are presented for undrained and drained application of $\Delta\tau_a$. As for the number of cycles to failure in Section 12.2.3, the shear strains depend strongly on whether $\Delta\tau_a$ is applied undrained and drained, and whether $\Delta\tau_a$ is applied drained by increasing or decreasing the normal stress.

The shear strain in the triaxial tests is assumed to be 1.5 times the vertical strain. This is an approximation for γ_a in the drained tests, which will also experience volumetric strains due to change in octahedral stress and dilatancy. Volumetric strains can be calculated with the constrained moduli in Section 16 and the dilatancy parameters in Andersen & Schjetne (2013).

Figures 13.12 to 13.14 present average and cyclic shear strain contours as functions of N, and Figures 14.2 to 14.10 present pore pressure contours for the same sands.
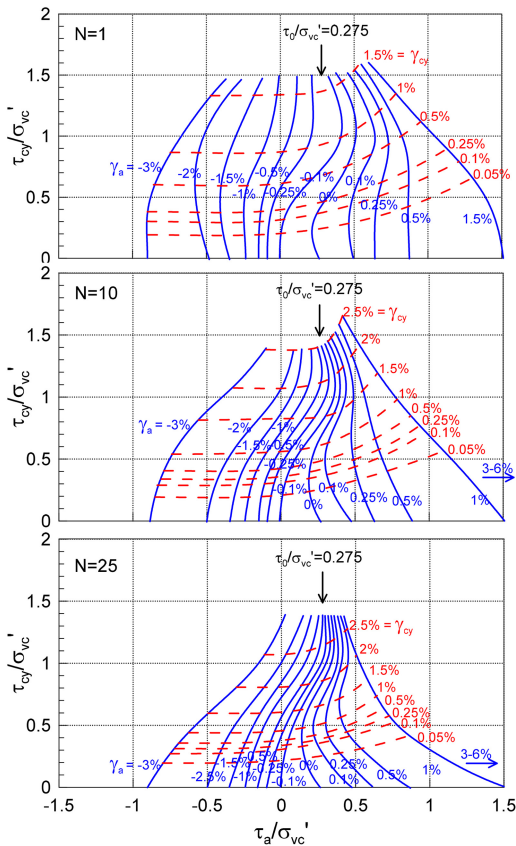
Figure 13.17. Average and cyclic shear strains as functions of average and cyclic shear stresses in triaxial tests on Baskarp Sand with $D_r \sim 96\%$ and $w = 20\%$. $\sigma'_{vc} = 250$ kPa. Precycling: 400 cycles of $\tau_{cy}/\sigma'_{vc} = 0.1$. $\Delta\tau_a$ applied undrained. Upper: $N = 1$. Middle: $N = 10$. Lower: $N = 25$.

13.5 *Shear strains in cyclic tests on clay.*

Shear strain contours for normally consolidated Drammen clay were presented for both DSS and triaxial tests in Section 7.3, as functions of number of cycles in Figures 7.9 and 7.11 and as functions of average and cyclic shear stresses in Figures 7.6 and 7.7. Shear strain contours for overconsolidated Drammen clay (OCR = 4 and 40) can be found in Andersen (2004).

13.6 *Cyclic stress strain anisotropy*

In Sections 11.1 and 11.2 it was shown that the monotonic stress-strain behavior of both sand, silt and clay is highly anisotropic and non-linear. The same is true for cyclic stress-strain behavior. The relationships between average shear stress and strain and between cyclic shear stress and strain after 10 cycles are shown for very dense Baskarp sand in Figure 13.22 and for Drammen clay in Figure 13.23. The stress-strain behavior depends on the ratio between average and cyclic shear stresses. The curves in Figures 13.22 and 13.23 were based on the assumption of $\tau_{cy}/\Delta\tau_a = 1{:}1$
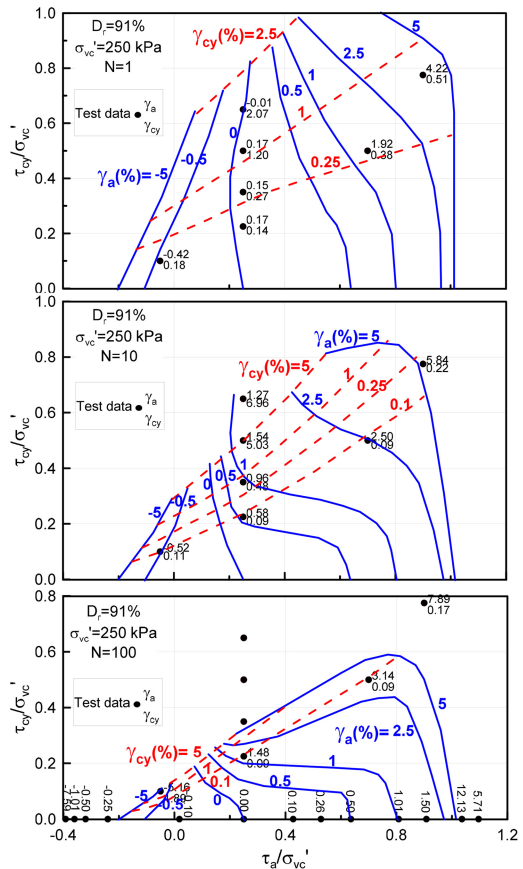
Figure 13.18. Average and cyclic shear strains as functions of average and cyclic shear stresses in triaxial tests on Sand 3. $D_r \sim 91\%$. $w = 21\%$. $\sigma'_{vc} = 250$ kPa. Precycling: 400 cycles of $\tau_{cy}/\sigma'_{vc} = 0.1$. $\Delta\tau_a$ applied drained by increasing vertical stress in compression and decreasing vertical stress in extension. Upper: $N = 1$. Middle: $N = 10$. Lower: $N = 100$.

in the DSS test and estimated triaxial stress paths ending at the same shear strain combinations as in the DSS test, as illustrated in Figure 12.34. This is the same assumption as used for cyclic strength anisotropy in Section 12.5 (Table 12.1). The stress-strain curves in Figures 13.22 and 13.23 were established by plotting corresponding values of shear stresses and strains at the intersections between the stress paths and the contours in the contour diagrams. It is in the triaxial tests assumed that the shear strain is 1.5 times the vertical strain. This is an approximation for γ_a in the triaxial tests with drained $\Delta\tau_a$, as discussed in Section 13.4.

Similar relationships can be established between average shear stress and permanent shear strain, based on permanent shear strain contour diagrams (see discussion in Section 6.2).

For Baskarp sand in Figure 13.22 the average shear stress is applied drained by increasing the vertical stress in compression and increasing the horizontal stress in extension. The estimated behavior for applying the average shear stress by decreasing the vertical
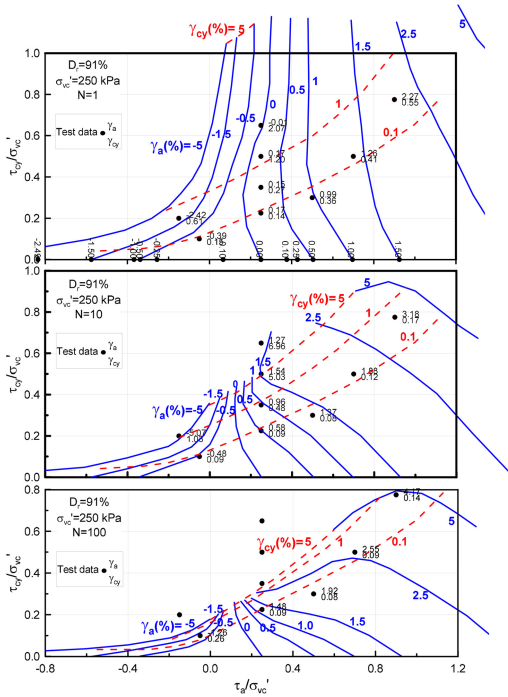
Figure 13.19. Average and cyclic shear strains as functions of average and cyclic shear stresses in triaxial tests on Sand 3. $D_r \sim 91\%$. $w = 21\%$. $\sigma'_{vc} = 250$ kPa. Precycling: 400 cycles of $\tau_{cy}/\sigma'_{vc} = 0.1$. $\Delta\tau_a$ applied undrained. Upper: $N = 1$. Middle: $N = 10$. Lower: $N = 100$.

stress in extension is also shown. This latter situation can be important in many cases, such as for the windward leg of multi-legged structures. The data in Figure 13.22 show that the cyclic stress-strain behavior is highly non-linear and anisotropic. The cyclic stress-strain relationship for DSS loading is lower than both triaxial compression and extension, even when the average shear stress in extension is applied by decreasing the vertical stress. This means that analyses based on DSS tests may overestimate the cyclic displacements and underestimate soil spring stiffnesses of structures on very dense sand. The difference in cyclic stiffness between triaxial and DSS tests will decrease with decreasing relative density.

Drammen clay also exhibits strong anisotropy and non-linearity, but the DSS curves plot between compression and extension. For clays it may therefore be more acceptable to perform stiffness and displacement analyses based on DSS data alone. This assumption was applied with reasonable success for the interpretation of the Brent B cyclic displacement analyses described in Section 19.

13.7 Effect of OCR

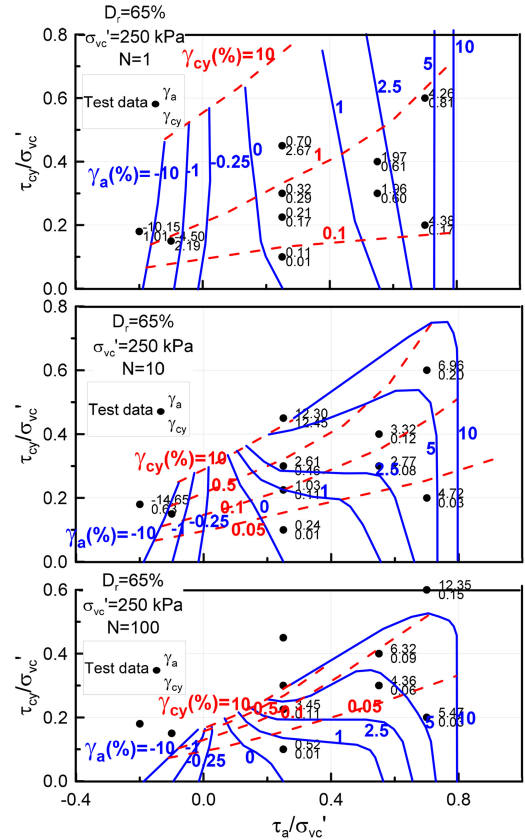The effect of overconsolidation on the stress strain behavior in monotonic tests was discussed in Section

Figure 13.20. Average and cyclic shear strains as functions of average and cyclic shear stresses in triaxial tests on Sand 3. $D_r \sim 65\%$. $w = 26\%$. $\sigma'_{vc} = 250$ kPa. Precycling: 400 cycles of $\tau_{cy}/\sigma'_{vc} = 0.1$. $\Delta\tau_a$ applied drained by increasing vertical stress in compression and decreasing vertical stress in extension. Upper: $N = 1$. Middle: $N = 10$. Lower: $N = 100$.

11.3. Figure 13.24 presents the reduction in shear modulus for both monotonic and two-way cyclic undrained DSS tests in a different manner. The plot shows the ratio between secant shear moduli of overconsolidated and normally consolidated soils as a function of the degree of shear strength mobilization, τ/τ_f. The cyclic data are given for $N = 10$, but the normalized results were not sensitive to N. The monotonic data are normalized by the undrained static shear strength, and the cyclic data are normalized by the cyclic shear strength for $N = 10$. The plot includes Drammen clay with $OCR = 4$, 10, 25, 40 and 50, a clay till with $OCR = 3$, a clayey silt with $OCR \sim 6$ and a very dense sand with $OCR = 4$. These are the same soils that were plotted to show the effect of OCR on static shear strength in Figure 10.7, and cover soils with different dilation response in the normally consolidated state (Section 10.5).

The plot shows that the effect of OCR:

– is relatively constant with degree of shear strength mobilization, τ/τ_f, for a given soil and a given OCR
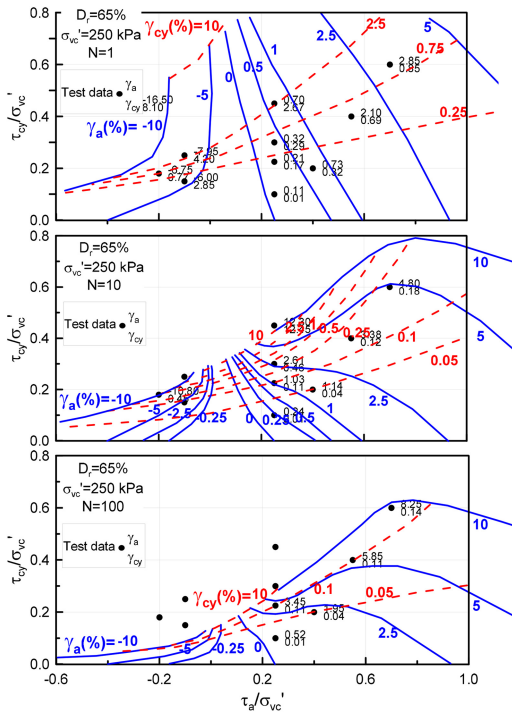
Figure 13.21. Average and cyclic shear strains as functions of average and cyclic shear stresses in triaxial tests on Sand 3. $D_r \sim 65\%$. $w = 26\%$. $\sigma'_{vc} = 250$ kPa. Precycling: 400 cycles of $\tau_{cy}/\sigma'_{vc} = 0.1$. $\Delta\tau_a$ applied undrained. Upper: N = 1. Middle: N = 10. Lower: N = 100.
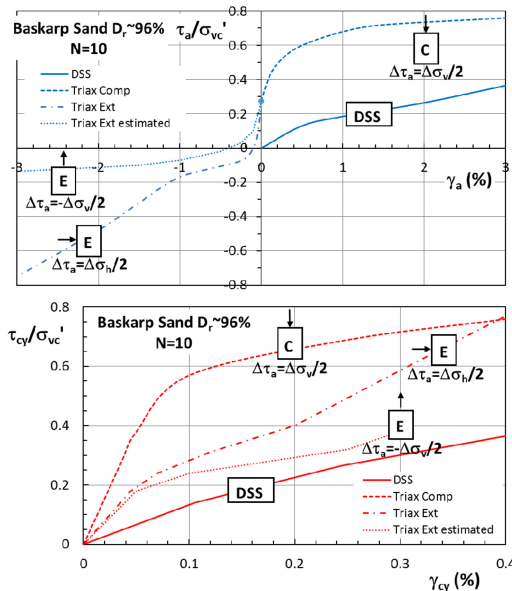

Figure 13.22. Relationships between average shear stress and strain (upper) and cyclic shear stress and strain (lower) for very dense normally consolidated Baskarp sand after 10 cycles. $\Delta\tau_a$ applied drained.
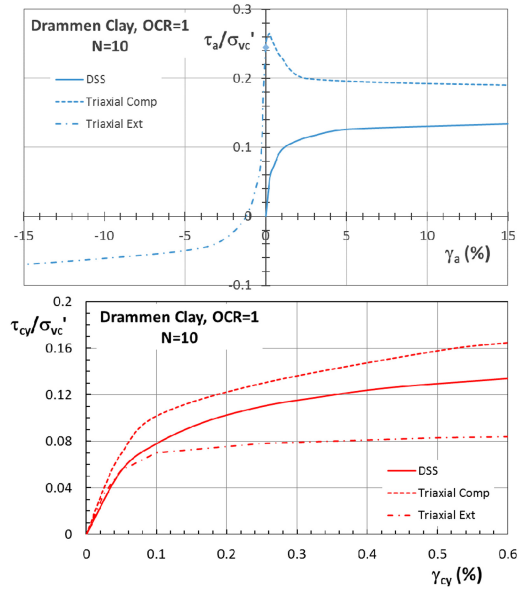

Figure 13.23. Relationships between average shear stress and strain (upper) and cyclic shear stress and strain (lower) for normally consolidated Drammen clay after 10 cycles.
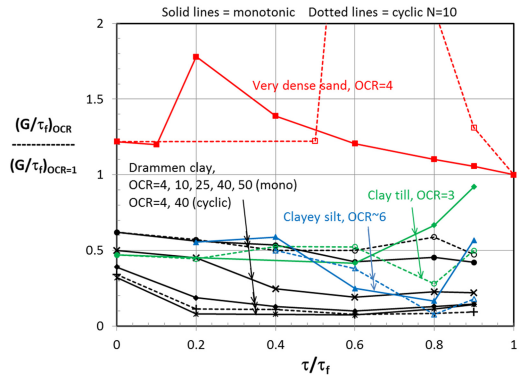

Figure 13.24. Secant shear modulus for overconsolidated relative to normally consolidated soils as a function of degree of shear strength mobilization. Undrained monotonic and two-way cyclic DSS tests.

– is reasonably similar for cyclic and monotonic loading
– increases with increasing overconsolidation ratio

The ratio between secant modulus of overconsolidated and normally consolidated soils is smaller than 1 for clays and larger than 1 for very dense sand. The clay till and the clayey silt are closer to the clay.

The practical consequence of this effect of OCR is that structures designed with the same safety factor (degree of strength mobilization) will experience larger displacements than structures on normally consolidated soils for soils that are contractant in their normally consolidated state. The effect can be the

opposite for structures on soils that are dilative in their normally consolidated state.

The absolute value of the stiffness will increase with increasing OCR for given consolidation stress and strength mobilization, both for clay and sand, but significantly less than the increase in shear strength.

14 PORE PRESSURE

14.1 Pore pressure in DSS tests on normally consolidated sand and silt

Figure 14.1 presents contours of permanent pore pressure as a function of cyclic shear stress and number of cycles in DSS tests with $\tau_a = 0$ on normally consolidated sand and silt. These contours are based on interpolation and extrapolation of data from various sands and silts in NGI's data base. This involves considerable uncertainty, and the contours should be regarded as estimates.

The diagrams are given for different values of $(\tau_{cy,f}/\sigma'_{ref})_{N=10}$ for $\tau_a = 0$ and can be related to relative density and water content through the diagrams for cyclic shear strength in Figures 12.1 and 12.2. The exponent in the reference stress used for normalization is consistent with the values established in Section 12.1.1, i.e. n = 0.9. Cyclic shear strain contours for the same conditions are presented in Figure 13.1, cyclic shear strength in Figures 12.15 and 12.16, and average and cyclic shear strain contours in Figures 13.2 to 13.11.

14.2 Pore pressure in triaxial tests on normally consolidated sand and silt

Figures 14.2 to 14.4 present examples of permanent pore pressure contour diagrams for triaxial tests on 3 clean sands for average shear stress of $\tau_a = \tau_0$. Figures 14.5 to 14.10 present examples of pore pressure contours as functions of average and cyclic shear stresses. Grain size characteristics for the different soils are presented in Table 7.1. The density varies from $D_r = 65$ to 100%. The results show that the sand dilates less and become softer with decreasing density and increasing fines content.

Cyclic shear strength contours for the same sands are presented in Figures 12.21 to 12.25, and average and cyclic shear strain contours in Figures 13.12 to 13.21.

14.3 Pore pressure in cyclic tests on clay

Permanent pore pressure contours for normally consolidated Drammen clay were presented for both DSS and triaxial tests in Section 7.6, as a function of number of cycles in Figure 7.13 and as a function of average and cyclic shear stresses in Figure 7.12. Pore pressure contours for overconsolidated Drammen clay (OCR = 4 and 40) can be found in Andersen (2004).
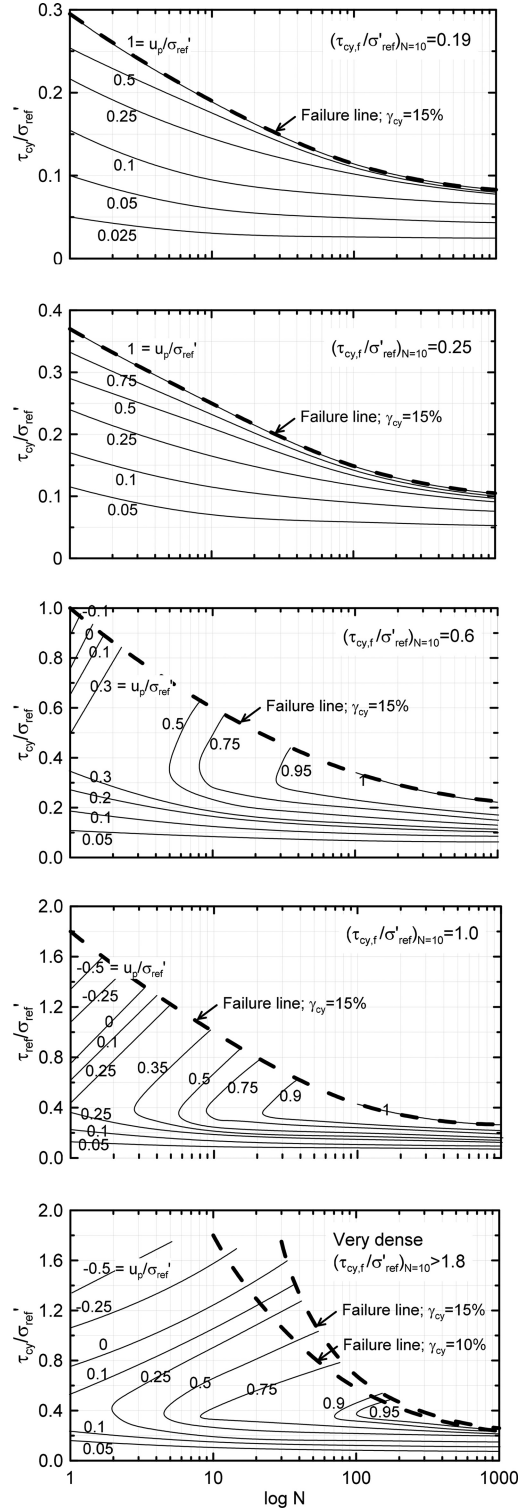

Figure 14.1. Pore pressure contours for DSS tests with $\tau_a = 0$ on normally consolidated sand and silt with different $(\tau_{cy,f}/\sigma'_{ref})_{N=10}$.
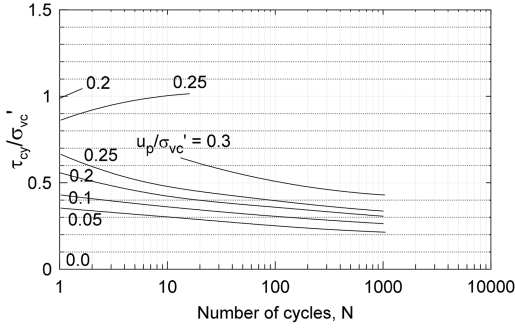
Figure 14.2. Permanent pore pressure as a function of number of cycles and cyclic shear stress for $\tau_a/\sigma'_{v,c} = \tau/\sigma'_{v,c} = 0.25$. Triaxial tests on Baskarp sand. $D_r \sim 96\%$. $w = 20\%$. $\sigma'_{vc} = 250$ kPa. Precycling: 400 cycles of $\tau_{cy}/\sigma'_{oct,c} = 0.1$. Samples prepared by pluviation.

Figure 14.3. Permanent pore pressure as a function of number of cycles and cyclic shear stress for $\tau_a/\sigma'_{v,c} = \tau/\sigma'_{v,c} = 0.25$. Triaxial tests on Sand 3. $D_r \sim 91\%$. $w = 21\%$. $\sigma'_{vc} = 250$ kPa. Precycling: 400 cycles of $\tau_{cy}/\sigma'_{oct,c} = 0.1$. Samples prepared by pluviation.
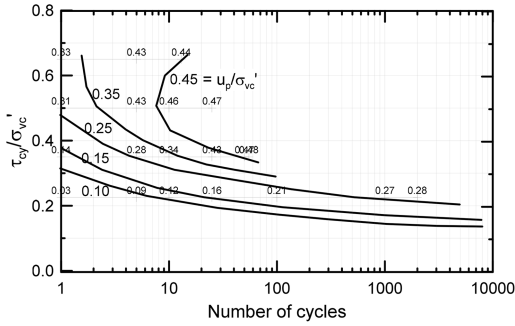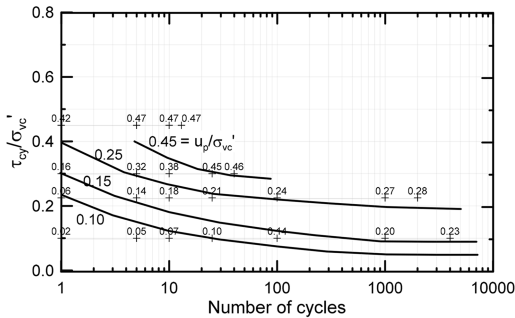

Figure 14.4. Permanent pore pressure as a function of number of cycles and cyclic shear stress for $\tau_a/\sigma'_{v,c} = \tau/\sigma'_{v,c} = 0.25$. Triaxial tests on Sand 3. $D_r \sim 65\%$. $w = 26\%$. $\sigma'_{vc} = 250$ kPa. Precycling: 400 cycles of $\tau_{cy}/\sigma'_{oct,c} = 0.1$. Samples prepared by pluviation.
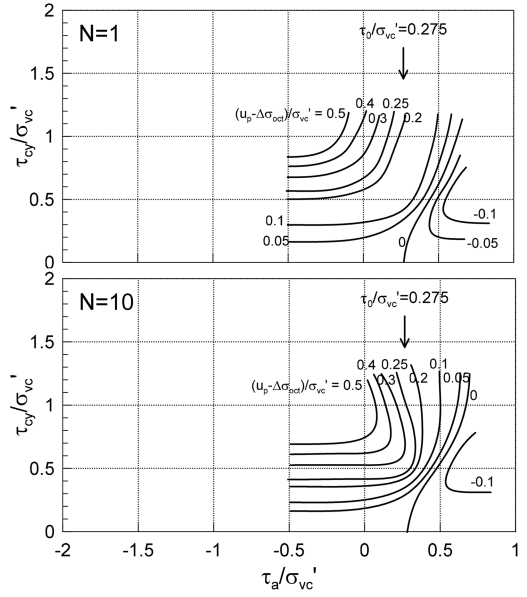

Figure 14.5. Permanent pore pressure as a function of average and cyclic shear stresses. Triaxial tests on Baskarp sand. $D_r \sim 96\%$. $w = 20\%$. $\sigma'_{vc} = 250$ kPa. Precycling: 400 cycles of $\tau_{cy}/\sigma'_{oct,c} = 0.1$. $\Delta\tau_a$ applied drained. Upper: N = 1. Lower: N = 10.
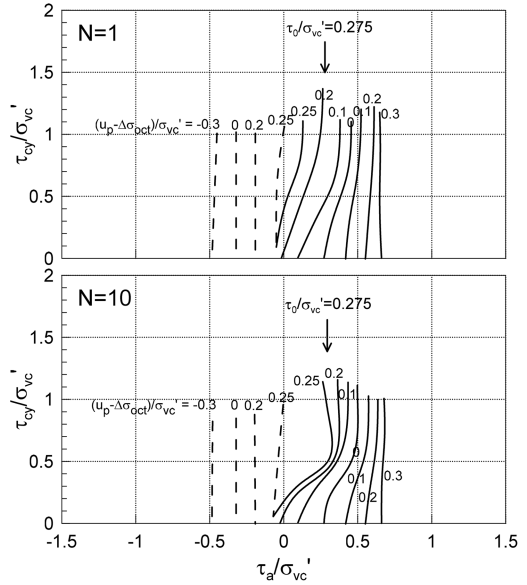

Figure 14.6. Permanent pore pressure as a function of average and cyclic shear stresses. Triaxial tests on Baskarp sand. $D_r \sim 96\%$. $w = 20\%$. $\sigma'_{vc} = 250$ kPa. Precycling: 400 cycles of $\tau_{cy}/\sigma'_{oct,c} = 0.1$. $\Delta\tau_a$ applied undrained. Upper: N = 1. Lower: N = 10.

Figure 14.7. Permanent pore pressure as a function of average and cyclic shear stresses. Triaxial tests on Sand 3. $D_r \sim 91\%$. $w = 21\%$. $\sigma'_{vc} = 250$ kPa. Precycling: 400 cycles of $\tau_{cy}/\sigma'_{vc} = 0.1$. $\Delta \tau_a$ applied drained by increasing vertical stress in compression and decreasing vertical stress in extension. Upper: $N = 1$. Middle: $N = 10$. Lower: $N = 100$.

Figure 14.9. Permanent pore pressure as a function of average and cyclic shear stresses. Triaxial tests on Sand 3. $D_r \sim 65\%$. $w = 26\%$. $\sigma'_{vc} = 250$ kPa. Precycling: 400 cycles of $\tau_{cy}/\sigma'_{vc} = 0.1$. $\Delta \tau_a$ applied drained by increasing vertical stress in compression and decreasing vertical stress in extension. Upper: $N = 1$. Middle: $N = 10$. Lower: $N = 100$.
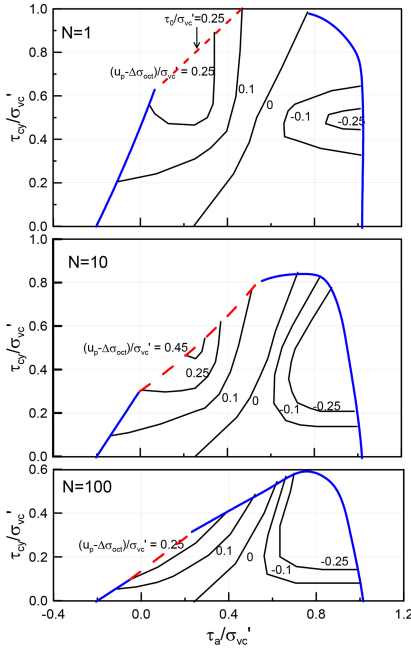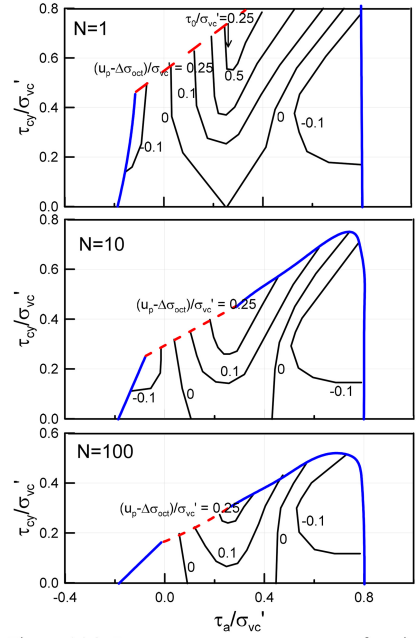

Figure 14.8. Permanent pore pressure as a function of average and cyclic shear stresses. Triaxial tests on Sand 3. $D_r \sim 91\%$. $w = 21\%$. $\sigma'_{vc} = 250$ kPa. Precycling: 400 cycles of $\tau_{cy}/\sigma'_{vc} = 0.1$. $\Delta \tau_a$ applied undrained. Upper: $N = 1$. Middle: $N = 10$. Lower: $N = 100$.
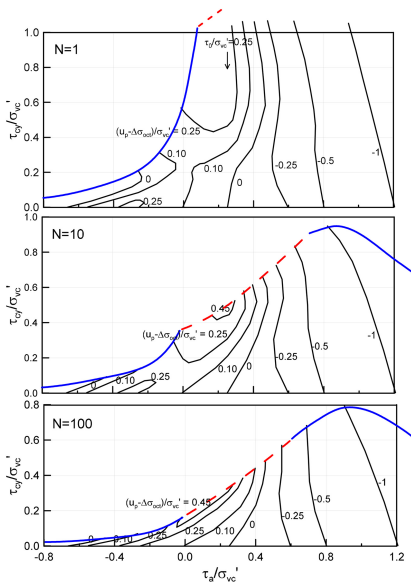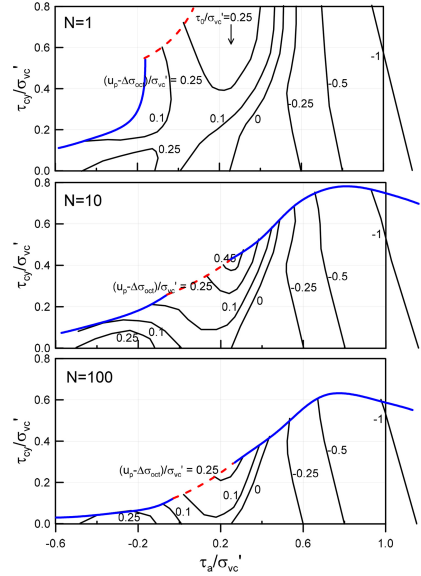

Figure 14.10. Permanent pore pressure as a function of average and cyclic shear stresses. Triaxial tests on Sand 3. $D_r \sim 65\%$. $w = 26\%$. $\sigma'_{vc} = 250$ kPa. Precycling: 400 cycles of $\tau_{cy}/\sigma'_{vc} = 0.1$. $\Delta \tau_a$ applied undrained. Upper: $N = 1$. Middle: $N = 10$. Lower: $N = 100$.
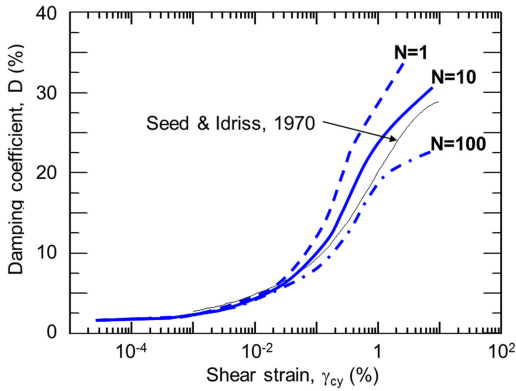
Figure 15.1. Damping coefficient as determined in stress-controlled two-way cyclic DSS tests.

15 DAMPING

The damping coefficient, D, will also depend on the average and cyclic shear stresses, number of cycles, and stress path (i.e. triaxial vs. DSS), and should be plotted in contour diagrams as the other cyclic soil parameters. However, cyclic tests have so far not been used to determine damping to the same extent as the other parameters. Some available data are plotted as a function of cyclic shear strain in Figure 15.1. The curves are mainly based on results from stress-controlled two-way cyclic DSS tests with 10 s load period and resonant column tests on Great Belt Clay with OCR = 3 (Kleven & Andersen, 1991). The Great Belt Clay is a low plasticity clay till with $I_p = 13\%$. However, tests on normally consolidated offshore clay with $I_p = 25$–30% have given very similar results.

The curves in Figure 15.1 show that the damping coefficient depends on the number of cycles. The Seed & Idriss (1970) curve is shown to be equivalent to a curve for about 25 cycles. The curves are not checked for various different clays, and should therefore be used with caution. As mentioned above, the damping will also depend on average shear stress and stress path.

The tests on Great Belt clay seemed to indicate that the damping ratio may decrease with decreasing load period.

16 CONSOLIDATION CHARACTERISTICS

The reconsolidation modulus and the permeability are needed to calculate the dissipation of cyclically-induced pore pressure, as mentioned in Section 5.3. The reconsolidation modulus can be determined from unload/reload sequences in the oedometer. Experience for clays is that the reconsolidation modulus after cyclic loading is about 2/3 of the oedometer reloading modulus (Yashuara & Andersen 1991). Similar information is not available for sand and silt.

Correlations for coefficient of permeability can be found in Andersen & Schjetne (2013). The permeability was correlated to water content and clay content for clay, and with water content and D_{10} for sand and silt.

16.1 *Constrained modulus formulation, sand and silt*

The constrained modulus is non-linear, and also depends on the stress history; i.e. virgin loading versus unloading and reloading (Figure 16.1). The constrained tangential modulus can be expressed by the following non-linear formulation (e.g. Andersen & Schjetne 2013):

$$M_l = m_l \cdot p_a \cdot (\sigma_v'/p_a)^{nl}$$

$$M_u = m_l \cdot p_a \cdot (\sigma_{v,max}'/p_a)^{nl} \cdot m_u \cdot (\sigma_v'/\sigma_{v,max}')^{nu}$$

$$M_r = m_l \cdot p_a \cdot (\sigma_{v,max}'/p_a)^{nl} \cdot m_r \cdot (\sigma_v'/\sigma_{v,max}')^{nr}$$

where:

- M_l, M_u, M_r are the tangential constrained moduli for first loading (virgin), unloading and reloading, respectively.
- m_l, m_u, m_r are the constrained modulus numbers for first loading (virgin), unloading and reloading, respectively.
- n_l, n_u, n_r are the exponents for first loading (virgin), unloading and reloading, respectively.
- p_a is the atmospheric pressure (100 kPa).
- σ_v' is the vertical effective stress.
- $\sigma_{v,max}'$ is the maximum vertical effective stress prior to unloading.

Formulae to calculate the volumetric strains can be established by integration and are given in Andersen and Schjetne (2013).

The formulation for virgin loading was proposed for sand by Janbu (1963), who used an exponent of n = 0.5. A modification to this exponent is proposed in Section 16.2.

The formulation has been tested for sand and silt. An example of measured oedometer test data is presented in Figure 16.1, which includes the results of curve fitting with the proposed formulation. The test was run with constant rate of strain and had overnight rest periods of 16hrs before unloading. Significant creep occurred during the rest periods even if the fines content was only 1%. The rest period is not modeled in the curve fitting, and the unload/reload curve is shifted to the start of the rest period. It is assumed that the creep causes an apparent preconsolidation effect and that the loading curve will join the virgin loading curve at a stress above the previous maximum stress, as in clay. The example shows that the proposed formulation is able to give excellent agreement with measured behavior. The formulas capture differences in moduli for virgin loading, unloading and reloading as well as non-linearity within each of these loading branches.
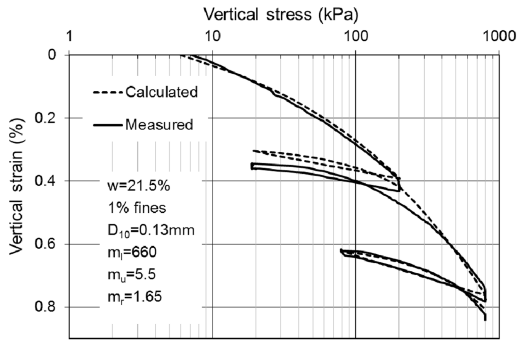
Figure 16.1.   Example of measured and calculated vertical strains with best fit parameters in oedometer test on clean sand.
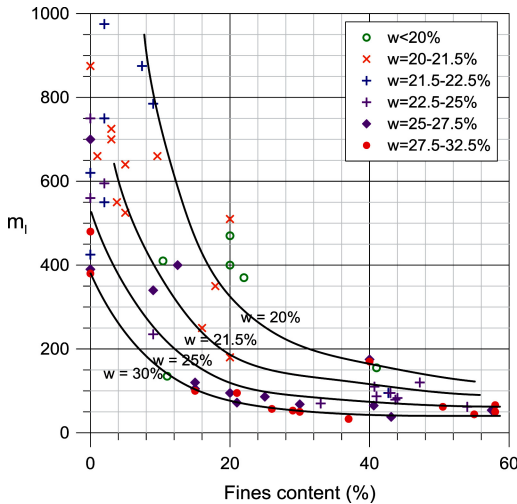

Figure 16.2. Modulus number for virgin loading as a function of fines content and water content.

16.2   Correlations for modulus formulation, sand and silt

Andersen & Schjetne (2013) presented parameter correlations for sands and silts for the proposed formula. More data has since become available. Updated and improved correlations are presented in Figures 16.2 and 16.3. The correlations are valid for exponent values of $n_l = 0.65$, $n_u = 1.05$ and $n_r = 0.1$. The average ratio between modulus numbers for unloading and reloading is 2.87 with a standard deviation of 0.78.

The parameters were determined by curve fitting to the measured oedometer data. Since the measured data can be influenced by seating problems and false deformations at low effective stresses, the curve fitting was generally made for vertical stresses at 10 kPa and higher. The exponents were fixed to the numbers specified above in order to make it possible to establish correlations, but it was still possible to achieve a good curve fitting. In a few cases, better agreement with the measured data could have been obtained by using different exponents.
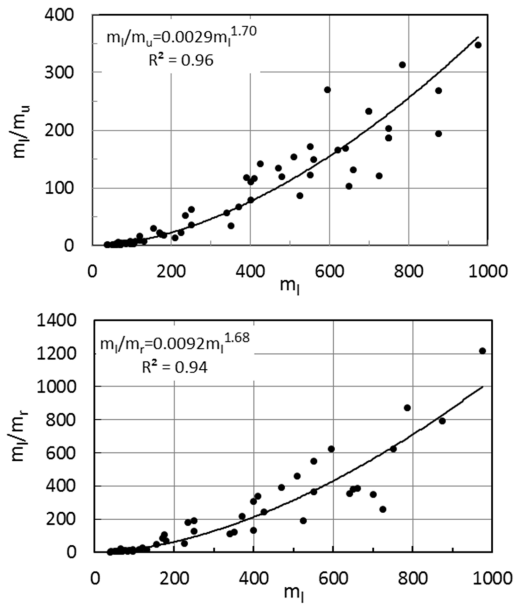

Figure 16.3.   Modulus numbers for unloading (upper) and reloading (lower) as functions of modulus number for virgin loading.

16.3   Constrained modulus for clay

The validity of the formulation in Section 16.1 has not been properly tested for clays. The formulation $M = m \cdot (\sigma'_v - p'_r)$ proposed by Janbu (1963) is often used for virgin constrained modulus of clays.

Karlsrud & Hernandez-Martinez (2013) proposed the following correlations for the parameter m based on Norwegian clays where w is the water content in %:

$m = 410 \cdot w^{-0.76}$ upper
$m = 319 \cdot w^{-0.76}$ average
$m = 250 \cdot w^{-0.76}$ lower

Their plot of p_r (in kPa) against m gives:

$p_r = 11.5 \cdot m$ upper
$p_r = 7.5 \cdot m$ average
$p_r = 3.5 \cdot m$ lower

However, consistent combinations of m and p_r should ideally be used. When the stress change gives a resulting effective stress moderately larger than the preconsolidation pressure, one may assume $p_r = 0$, and then Karlsrud & Hernandez-Martinez (2013) propose:

$m_0 = 235 \cdot w^{-0.76}$ upper
$m_0 = 172 \cdot w^{-0.76}$ average
$m_0 = 120 \cdot w^{-0.76}$ lower

The reloading secant constrained modulus after 50% unloading, $M_{secant,50}$, is presented in Figure 16.4. The modulus is measured in oedometer tests where the sample is first loaded past the preconsolidation pressure, p'_c, to a vertical stress, $\sigma'_{v,max}$, left for about 16 to 24 hours, unloaded by 50% and reloaded to $\sigma'_{v,max}$. This is done twice in most tests, first at $\sigma'_{v,max} \sim 2 \cdot p'_c$ and then at $\sigma'_{v,max} \sim 9 \cdot p'_c$. The results show that the
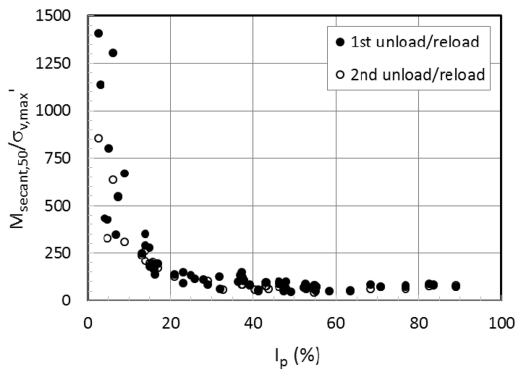
Figure 16.4. Reloading secant constrained modulus after 50% unloading from maximum past stress.

normalized reloading modulus is essentially independent of $\sigma'_{v,max}$, and that $M_{secant,50}/\sigma'_{v,max}$ increases with decreasing plasticity index. The reloading modulus is non-linear and will decrease with increasing degree of unloading.

17 SLOPE STABILITY UNDER CYCLIC LOADING

17.1 *Failure mechanism and stress conditions*

Slopes can be subjected to cyclic loading from different sources, like earthquakes, blasting, machine vibrations and wave pressure under water. The stability of slopes can be reduced by cyclic loading, but the mechanism can be different from that of a foundation or an anchor, since the strength mobilization in the soil under the weight can be much higher. A slope that may be vulnerable to cyclic degradation will normally have a low safety against failure under its own weight, whereas a foundation or an anchor will have a high safety under its weight and other permanent loads that act longer than the design event. A slope will experience both permanent and cyclic displacements during cyclic loading, but the failure mode is likely to be large permanent displacements due to the significant average shear stress from the weight. The duration of the cyclic load may be too short to accelerate the soil mass during the peak load, especially for cyclic events with load period of 1s or less. The critical mechanism is thus likely to be development of large permanent displacements during or after the cyclic event. A delayed failure can occur some time after the cycling event due to accelerated creep initiated by the cycling. The slope will stabilize as the excess pore pressure from the cyclic loading dissipates.

17.2 *Laboratory testing*

The loading conditions described above were simulated in two series of DSS tests in order to understand the mechanism and to recommend a design procedure. The laboratory tests were performed on high quality
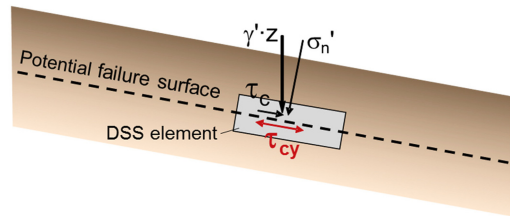

Figure 17.1. Simplified stress conditions in an infinitely long slope.

block samples of a quick clay (29 tests) and a soft marine clay from Onsøy (6 tests), both normally consolidated with an apparent overconsolidation ratio of about 1.5. Quick clay is not common offshore, but was tested since the stability of quick clay slopes on land under different cyclic loading events is relevant, and because highly sensitive quick clay may demonstrate mechanisms more clearly than less sensitive clays. The quick clay has a plasticity index of about 10%, a clay content of about 38%, a sensitivity of about 100, and a water content of about 39%. The Onsøy clay has a plasticity index of about 40%, a sensitivity of about 7 and a water content after consolidation of about 67%. There was some variability in the results due to soil inhomogeneity, and this shows up in some aspects in the following. The interpretation is, however, based on a larger database than given here.

The tests simulated the stress conditions in an infinitely long slope and were consolidated under a vertical effective normal stress and a horizontal shear stress due to the weight of the slope, as illustrated in Figure 17.1. The shear stress was varied to simulate different slope angles from 9.5° to 16°. The test program contained (1) monotonic strain-controlled reference tests with different strain rate and (2) tests with cyclic loading around the consolidation shear stress followed by creep and post creep monotonic tests. The cyclic tests were run to different prescribed permanent shear strain and then allowed to creep under the consolidation shear stress. The tests were undrained throughout, apart from one test that was allowed to drain between the creep phase and the subsequent monotonic phase, in order to see how much of the initial strength the slope would regain after the cyclically-induced pore pressure had dissipated. The quick clay test series included cyclic load periods of 1 s (13 tests) and 10 s (7 tests). The Onsøy clay test series was run with 10 s period. The load period influenced the number of cycles to reach a given shear strain, but the post cyclic creep and monotonic behavior were not influenced by whether the shear strain was generated by 1 s or 10 s load period.

17.3 *Laboratory test results*

The monotonic shear strength was found to increase with increasing consolidation shear stress as shown in Figure 17.2. This shear induced strength anisotropy is compared with the shear strength interpolated between triaxial compression and extension shear strengths
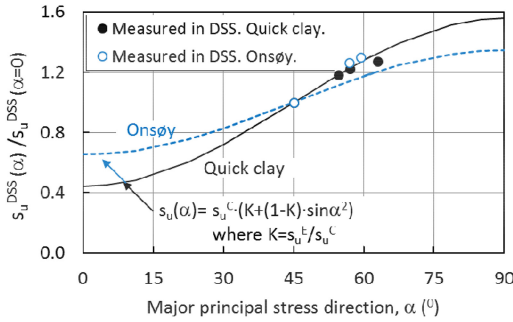
Figure 17.2. Shear strength as a function of inclination of major principal normal stress.

Figure 17.3. Typical results of monotonic tests and tests with cyclic loading and creep followed by monotonic loading. Quick clay with $\tau_a = \tau_c = 0.17 \cdot \sigma'_{vc}$.

Figure 17.4. Shear strain during creep phase in tests that have first been cycled to different permanent shear strain. Quick clay with $\tau_a = \tau_c = 0.06, 0.22$, and $0.29 \cdot \sigma'_{vc}$.

by the expression $s_u(\alpha') = s_u^C \cdot (K + (1 - K) \cdot \sin \alpha'^2)$, where $K = s_u^E / s_u^C$, and α' is the inclination of the major principal normal stress with the horizontal. The agreement is good for the quick clay, as one would expect based on Bjerrum (1973), but the measured DSS strengths are higher than expected from the interpolation between the triaxial strengths for Onsøy clay.

Figure 17.3 shows typical results of one monotonic test and two tests with cyclic loading and subsequent monotonic loading. The two cyclic tests were cycled to prescribed permanent shear strains of $\gamma_p = 2\%$ and 12%, respectively, before being sheared monotonically. The results show that:

– The strains in the cyclic tests can exceed the monotonic stress-strain curve. This is due to rate effect. The cyclic tests were run with 10 s load period. The monotonic test was run with 4.5% shear strain/hr.
– The permanent shear strain increases with number of cycles for the stress conditions of the tests in Figure 17.3, and failure can develop if cycling is continued.
– The static shear strength is reduced by cyclic loading. The post cyclic monotonic stress strain curves rapidly join the virgin monotonic stress strain curve. (The difference between the monotonic curves at large strain in Figure 17.3 is believed to be due to soil variability). This implies that the static shear strength is reduced if the permanent shear strain under cyclic loading approaches or exceeds the peak strain in virgin monotonic shearing. It should be mentioned that the reduction in static shear strength can be more significant if the cyclic loading generates large cyclic shear strains. This was seen both in the quick clay and in tests on the less sensitive Drammen clay (Andersen 1988). For slope stability, however, where the average shear stress is large, permanent shear strain will be predominant.

Figure 17.4 shows typical creep test results, where tests that have been cycled to different permanent shear strains, γ_p, at three different consolidation shear stress levels, $\tau_a = \tau_c$, before being left to creep at this shear stress. The γ_p at end of cycling is defined by the start of the creep curves. The results show that:
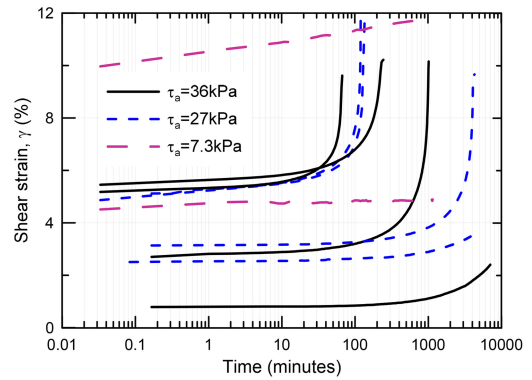
– Cyclic loading influences the creep rate, and the time to creep failure decreases with increasing γ_p at end of cycling and increasing τ_a.

Figure 17.5 illustrates the correlation between creep and monotonic behavior, showing the results of one monotonic test and 3 tests with various combinations of cyclic loading, creep and post-cyclic monotonic loading. The tests were all consolidated with a shear stress of $\tau_a = 0.22 \cdot \sigma'_{vc}$. The monotonic test was sheared with a strain rate of 4.5%/hr to a shear strain of 5.5%, when the rate was temporarily increased to 31%/hr. The 3 other tests were first cycled to a specified permanent shear strain. One test was cycled to $\gamma_p = 2.5\%$, left to creep to 3.5% and then sheared monotonically with about 5%/hr. The two other tests were left to creep after being cycled to $\gamma_p = 3.1$ and

Figure 17.5. Stress-strain behavior (upper) and effective stress paths (lower) for creep and monotonic tests with different rate of shear strain. Quick clay with $\tau_a = \tau_c = 0.22 \cdot \sigma'_{vc}$.

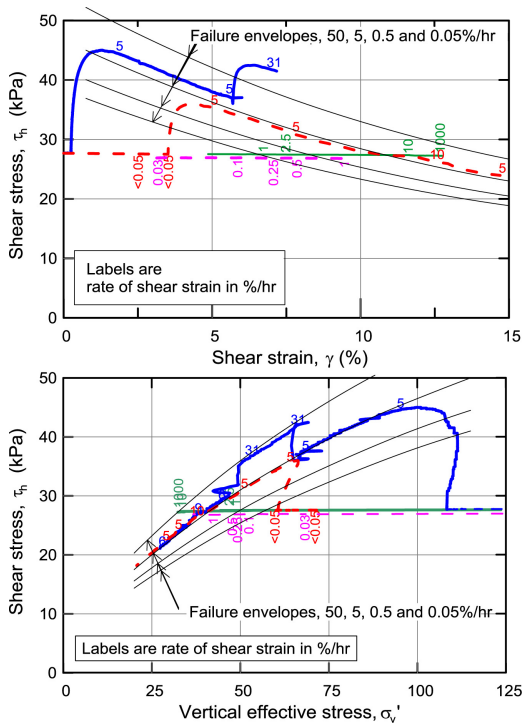5%, respectively. There is some scatter due to sample inhomogeneity, but the results indicate that:

- The peak and the post peak part of the stress-strain curves and the failure envelopes in the effective stress path plot are rate dependent. Contours can be drawn to define how the peak, the post peak stress-strain curve and the failure envelope depend on the rate of shear strain.
- The creep tests fail at a contour consistent with the rate of creep in the monotonic tests.

17.4 Strains due to cyclic loading

Contours of average and cyclic shear strains that develop during cyclic loading are determined based on the laboratory tests and presented in Figure 17.6 for quick clay and in Figure 17.7 for Onsøy clay. The average shear stress is applied drained, and the axes are normalized by the shear strength after consolidation to the relevant shear stress (Figure 17.2). The curves intersect the horizontal axis at $\tau_a/s_{u,\tau c} = \tau_c/s_{u,\tau c} = 0.82$ because the reference shear strength is from tests sheared to failure in about 2 hrs, whereas the consolidation shear stress was allowed to act for significantly longer in order to reach a stable condition. The contours in Figure 17.6 are valid for 10 s load period. They can be extrapolated to other load periods by multiplying the numbers on the vertical axis by the factors in Table 17.1. The tests with 1s load period were also

Table 17.1. Factor to convert diagrams in Figures 17.6 and 17.7 to other load periods.

Load period (s):	10	1	0.1
Factor on vertical axis:	1.0	1.2	1.45

Figure 17.6. Average and cyclic shear strains as functions of average (drained) and cyclic shear stresses after 1 (upper) and 10 (lower) cycles. Quick clay. 10 s load period.

utilized when drawing the quick clay contours, even if these tests are not presented herein.

Ideally the diagrams in Figures 17.6 and 17.7 should present the permanent rather than the average shear strain. However, inspection of the test results show that the permanent shear strain is marginally smaller than the average shear strain when there is no shear stress reversal (i.e. when $\tau_{cy} < \tau_a$). In cases with shear stress reversal, the ratio between permanent and average shear strains will increase with increasing degree of shear stress reversal. In cases with full reversal (symmetrical cyclic loading), the permanent shear strain will be negative and the average shear strain will be small. For a slope to be vulnerable to cyclic loading and subsequent creep, it needs to have a relatively high degree of average shear stress mobilization, and large shear stress reversal is not likely to be critical. It is therefore considered fair to assume that the permanent shear strain is equal to the average shear strain for this purpose, where this assumption is on the conservative side. A discussion on permanent versus average shear strains is also given in Section 7.4.
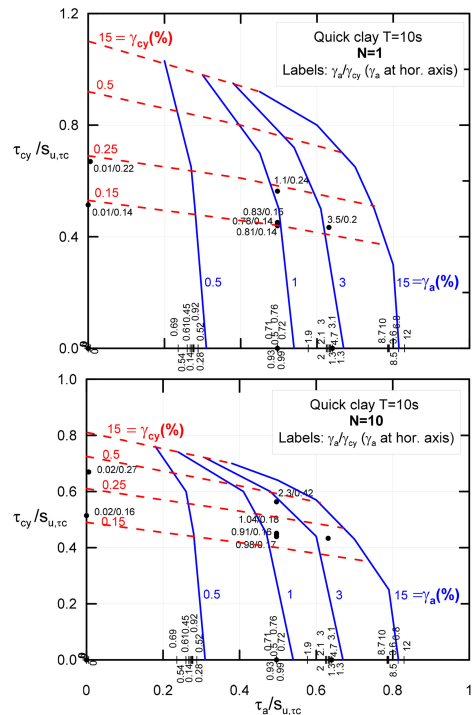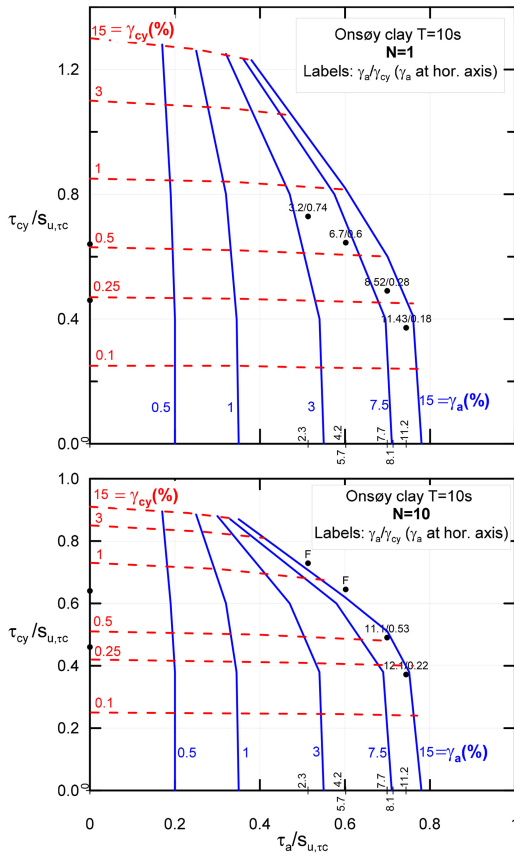
Figure 17.7. Average and cyclic shear strains as functions of average (drained) and cyclic shear stresses after 1 (upper) and 10 (lower) cycles. Onsøy clay. 10 s load period.

Figure 17.8. Time to failure under constant shear stress as a function of γ_p. Quick clay.
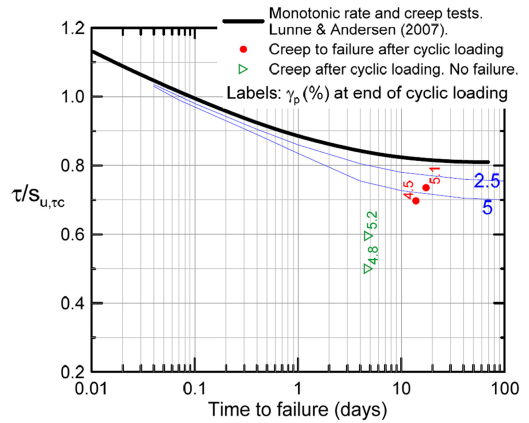
Figure 17.9. Time to failure under constant shear stress as a function of γ_p. Onsøy clay.

17.5 Time to failure as a function of γ_p and τ_c

Creep test data, such as in Figure 17.4, was used to construct the diagrams in Figure 17.8 and 17.9, where the time to failure after a cyclic loading event is given as a function of cyclic loading, expressed by γ_p, and the slope angle, expressed by $\tau_c/s_{u,\tau c}$, for quick clay and Onsøy clay, respectively. The shear strain in these diagrams is the shear strain at the end of cyclic loading. This shear strain can be determined from the diagrams in Figures 17.6 and 17.7. The permanent shear strain during consolidation is included in γ_a in these diagrams, and should be subtracted to get the permanent shear strain that develops during cyclic loading. The shear strain during consolidation is defined by the average shear strain along the horizontal axis in Figures 17.6 and 17.7.

Figures 17.8 and 17.9 show that Onsøy clay is less influenced by cyclic loading than the quick clay.

17.6 Strength repair from pore pressure dissipation

To see the effect of a serious cyclic event on the long term stability of a slope, one monotonic test was run on a quick clay after it had been allowed to drain after cyclic loading to $\gamma_p = 3.1\%$ and subsequent creep to 9.8%. The result is compared to a standard monotonic test in Figure 17.10. The results show that drainage gives almost full regain of the original static shear strength (95%). The shear strength without drainage would have been about 70% of the original shear strength.

17.7 Design procedure

The diagrams presented above can be used to evaluate if an infinitely long slope with homogeneous clay is stable after a cyclic loading event or if the event can initiate an immediate or a delayed slope failure. The evaluation can be done as follows:

1) Determine the normalized average and cyclic shear stresses in the slope and the equivalent number of cycles, N_{eq}. The shear stresses shall be normalized to a shear strength determined in a standard laboratory test without correction for rate effect,
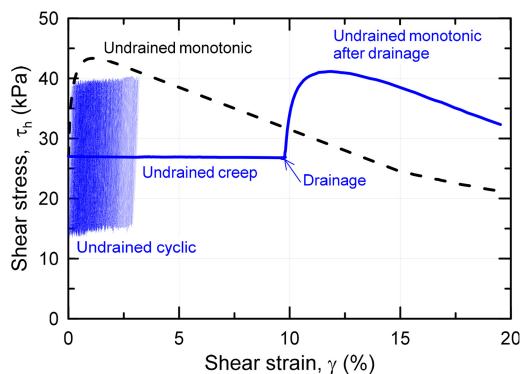
Figure 17.10. Effect of drainage after undrained cycling and creep on monotonic behavior of quick clay with $\tau_a = \tau_c = 0.22 \cdot \sigma'_{vc}$.

but accounting for the effect of shear stress during consolidation. The average shear stress can be found as illustrated in Figure 17.1. If the slope is consolidated under permanent loads in addition to the soil weight, the average shear stress can be assumed equal to the inverse of the safety factor of the slope under the permanent loads, including the soil weight. The maximum cyclic shear stress and the corresponding N_{eq} can be determined from the cyclic load history, as explained in Section 8.

2) Determine the permanent shear strain due to cyclic loading from diagrams such as Figure 17.6 or 17.7. This is done by entering the diagram with the average and cyclic shear stresses and N_{eq} from Point 1. The shear strain during consolidation shall be subtracted from the average shear strain. Interpolation between the diagrams must be done if N_{eq} differs from the N-values in the diagrams.

3) Calculate the time for dissipation of cyclically-induced pore pressure in order to estimate the duration of the undrained creep period. The pore pressure will start to dissipate when the cyclic event is over, counteracting the degradation due to creep. The reloading modulus (Section 16) should be applied in this analysis. Figure 17.10 shows that most of the original strength is regained when the pore pressure has dissipated.

4) Determine time to undrained creep failure by entering diagrams such as Figure 17.8 or 17.9 with the average shear stress from Point 1 and the permanent shear strain from Point 2. One can see from the diagrams that a quick clay slope that experiences a permanent shear strain of 2.5% due to cyclic loading will fail in about 10 days if the average shear stress is 0.64 times the undrained monotonic shear strength, i.e. if the safety factor for permanent loads is about 1.6. A slope on a less sensitive clay, like the Onsøy clay, which may be more representative for offshore clays, is less susceptible to failure due to cyclic loading and the corresponding safety factor would be 1.3.

5) In case the slope is subjected to additional permanent loads after the cyclic event and before the pore pressure has dissipated, determine whether the reduced strength is sufficient to carry the additional load. The reduced strength can be found as the shear stress of the original stress-strain curve at the shear strain determined in Point 2, in line with the finding in Figure 17.3. This shear stress should be reduced by about 5% to account for the strain it requires to reach the original stress-strain curve. In addition it is necessary to reduce the shear strength for rate effects according to Figure 7.5, since standard laboratory test are typically run with a rate of shear strain of ~4.5%/hr (~2 hrs to failure) and the load may act for a much longer time.

Important assumptions in this procedure are that:

– The slope is infinitely long, meaning that progressive failure is not considered. However, the general behaviour described herein will also be valid for progressive mechanisms.
– The slope consists of homogeneous clay. If thin silt layers are present, they may be more critical to cyclic loading than the clay.
– The above diagrams are for normally or lightly overconsolidated clays. The soil in the lower part of a slope can be overconsolidated if the slope is generated by erosion. Overconsolidation may influence the creep properties, but the effect of OCR has not been studied.

Johansson et al. (2013) applied the procedure to study the effect of blasting on the stability of a quick clay slope. They also report cases where blasting is believed to be the trigger of slope failures. Some of these failures were reported to occur some time after the blasting event.

18 CALCULATION PROCEDURES

The contour diagram concept has been used extensively to define soil behavior in practical foundation design of gravity structures, suction anchors, piles and monopiles. Typical calculation procedures are briefly summarized below.

18.1 *Capacity*

The capacity of a foundation under cyclic loading can be calculated by limit equilibrium, plastic limit or finite element procedures. Strength anisotropy can significantly influence the calculated failure mechanism and capacity, especially for dense sand and silt, and should be accounted for.

Andersen & Lauritzsen (1988) describe how the data from contour diagrams can be used in limit equilibrium methods to calculate the capacity under combined static and cyclic loads. The cyclic shear strength of the clay is determined from diagrams such as Figures 7.3 and 7.4. The irregular cyclic load history

is represented by an equivalent number of cycles of the maximum cyclic load, N_{eq}, that can be determined as described in Section 8. The cyclic shear strength at a given point on the failure surface (see Figure 6.1) is interpolated between the strengths from compression, DSS, and extension tests. The procedure is based on the assumption that the combination of average and cyclic shear strains is the same along the potential failure surface (strain compatibility), and on the condition that the average shear stresses along the potential failure surface are in equilibrium with the average loads. The procedure accounts for the redistribution of average soil stresses during cyclic loading and determines whether the failure mode will be large cyclic displacements, large average displacements, or a combination of the two.

One simplification that could be made to estimate the shear strength and the shear strength anisotropy is to assume that the ratio $\tau_{cy}/\Delta\tau_a$ in the individual elements is constant and proportional to the ratio between cyclic and average loads. However, this will not capture the redistribution of average shear stresses during the storm. This can be improved by determining the strain combination for the stress path considered the most important (e.g. DSS), and deriving the strength for the two other stress paths (e.g. compression and extension) for the strain combination at failure in DSS. The simplified methods are discussed in Section 12.5 and illustrated in Figure 12.34.

More recently, a finite element code (UDCAM, Jostad et al. 2014) has been developed where the $\tau_{cy}/\Delta\tau_a$-stress path is calculated in each integration point based on stress strain characteristics defined by contour diagrams of the type presented in Figures 7.6 and 7.7. Another finite element code (PDCAM, Jostad et al. 2015) also accounts for the pore pressure redistribution and dissipation during the cyclic load history. PDCAM need input in the form of compressibility and permeability in addition to the cyclic contour diagrams; see Section 16 for input. These programs perform the cyclic strain or pore pressure accumulation and dissipation on an element basis, redistributing both average and cyclic stresses within the foundation during the load history. The shear stress history, the cyclic degradation, and thus N_{eq}, can then be different from one integration point to the next, enabling progressive behavior to be captured.

The capacity of piles under vertical cyclic loading can be calculated by modelling the pile-soil interface with non-linear "t-z"-springs (Karlsrud & Nadim 1990), where t and z represent mobilized skin friction and vertical displacement, respectively, with cyclic and average components determined through strain contour diagrams such as in Figure 7.6.

18.2   *Cyclic displacements*

Cyclic displacements can be calculated using simplified finite element analyses with input in the form of cyclic stress vs cyclic strain curves established as discussed in Section 13.6 (Andersen & Hoeg 1991).

N_{eq} can be determined by assuming proportionality between shear stresses and loads as described in Section 8.

The shear stresses and shear strains become small at some distance from the structure, but the shear strains in this region may still contribute to the displacement since they are integrated over a large volume. The initial part of the stress strain curves is therefore important. Conventional laboratory tests may not be accurate at small strains, and should be supplemented by the initial shear modulus. Correlations for initial shear modulus are given in Section 11.4.

More refined analyses can also be performed by the finite element programs UDCAM and PDCAM described in Section 18.1, where N_{eq} and the shear stress path are determined on an element basis within the finite element program.

18.3   *Permanent displacements*

The calculation of permanent displacements must include components from both permanent shear strains during cyclic loading and volumetric strains from dissipation of cyclically induced pore pressure.

The permanent displacements due to shear strains can be calculated as described in Section 18.2. In the simplified analysis, the soil model is then defined in the form of permanent shear strain vs average shear stress instead of cyclic components. The relationship can be determined as discussed in Section 12.5.

The permanent displacements due to volumetric strains can be determined in a simplistic manner by first establishing the average and cyclic shear stress distribution in the soil, for instance from the simplified finite element analysis described above and in Section 18.2. The finite element analysis also gives information about major principal stress direction in the different elements and whether the DSS or triaxial stress paths should be used. When the average and cyclic shear stresses and the stress path are known, the permanent pore pressure can be determined from diagrams such as given in Figure 7.12 and Section 14. The permanent pore pressure develops under constant volume and leads to a reduced effective stress, as illustrated by path A-B in Figure 18.1. The soil will follow the reloading path B-C when the pore pressure dissipates, and the volumetric strains can be calculated as $\varepsilon = \Delta\sigma'/M = \Delta u_p/M$, where M is the reloading modulus. Reconsolidation characteristics are presented in Section 16.

More refined analyses with UDCAM and PDCAM, as described in Section 18.2 will give the permanent displacements due to shear strains. PDCAM will also provide the displacements due to volumetric strains.

If the conditions are essentially drained, the volumetric strains can, instead of entering pore pressure contour diagrams and using reconsolidation parameters, be determined by using volumetric strain contour diagrams. Examples of volumetric strain contour diagrams are not included herein, but can be established from drained cyclic tests.
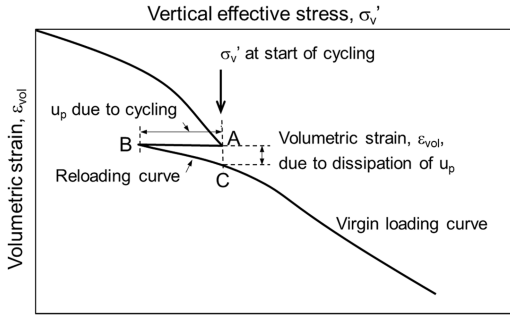
Figure 18.1. Vertical effective stress and volumetric strain during undrained cyclic loading and subsequent drainage.

Figure 18.2. Backbone curve to calculate displacement as a function of load during a cycle (based on Kaynia & Andersen 2015).

18.4 *Equivalent soil spring stiffnesses and damping*

Fully-integrated dynamic analyses require significant computational power and highly sophisticated soil models. Dynamic analyses of platforms have therefore traditionally been performed using equivalent linear or nonlinear foundation springs to represent the soil. These equivalent soil springs do not follow the behavior during an individual cycle, but represent the ratio between amplitudes of load and displacement and can be calculated with the procedures described for cyclic displacements (Section 18.2). A method to follow the behavior during a cycle is proposed in Section 18.5.

For wave loading, two definitions have often been used for the equivalent stiffness (Andersen 1991):

– Average stiffness, defined as the ratio between standard deviation of forces and displacements of the waves in the peak part of the design storm. This stiffness has often been the basis for dynamic analyses during design of gravity based structures. Calculated and measured values are presented for the Brent B Condeep platform in Figure 19.1.
– Secant stiffness for the maximum wave in the design storm, assuming the maximum wave arrives at the end of the peak part of the design storm. This stiffness gives the maximum cyclic displacements under the characteristic wave and will be lower than the average stiffness defined above. Andersen & Aas (1980) present calculated maximum displacements as functions of the maximum wave load for the Brent B Condeep platform.

Equivalent damping can be calculated by finite element analyses (e.g. INFIDEL, Hansteen 1991), where the damping in the integration points is integrated over the soil volume. The stress-strain input is the same as for the simplified finite element analysis in Section 18.2, but including additional input about damping properties (Section 15).

18.5 *Foundation springs for individual cycles*

Kaynia & Andersen (2015) present a nonlinear soil spring method where the foundation is represented by a nonlinear force-deformation (or moment-rotation) curve, often 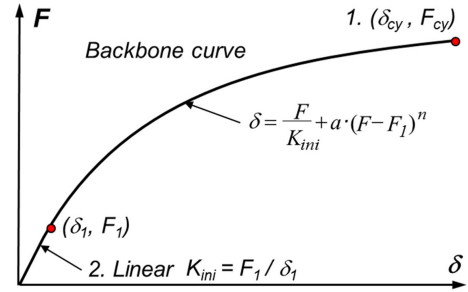referred to as a backbone curve, which can be used for the whole response cycle in a time domain dynamic analysis. The model accounts for the degradation from previous cycles and can be used by applying the Masing rule (Masing 1926) for a cycle at a given time in the load history.

With reference to Figure 18.2, the backbone curve is established as follows:

1) Calculate cyclic displacement (amplitude), δ_{cy}, for the cyclic load (amplitude), F_{cy}, of the given cycle. This can be done as described in Section 18.2.
2) Determine initial stiffness. This can be done by determining $u_p = f(\tau_{cy}/s_u)$ as described in Section 18.3 for the N_{eq} applied in (1). An equivalent over-consolidation ratio, $OCR_{eq} = \sigma'_{vpc}/(\sigma'_{vc}-u_p)$ is calculated, and G_{max} is determined from the expression in Section 11.4. $G_{max} = f(\tau_{cy}/s_u)$ can be transformed to a fictitious stress strain curve that can be used in a FE model to calculate the initial stiffness, K_{ini}, of the backbone curve.
3) Determine soil damping by integrating the damping in the soil in a finite element analyses as described at the end of Section 18.4.
4) Establish the load-displacement backbone curve for a given characteristic cyclic load by finding the curve that fulfils the following conditions when applying the Masing rule: cyclic displacement amplitude from (1), initial stiffness from (2) and damping from (3). Kaynia & Andersen (2015) proposed the mathematical expression proposed in Figure 18.2 that can be used in cases with limited dilatancy within a cycle. Iteration is required to shape the backbone curve to fulfil the third requirement. The mathematical expression and the use of the Masing rule may not be straightforward in cases with significant dilation within the cycle, as for dense sand in the left part of Figure 6.7.

19 VERIFICATION BY PROTOTYPE OBSERVATIONS AND MODEL TESTS

The calculation methods using the soil models described herein, and briefly summarized in Section 18, have been verified by prediction and

backcalculation of prototype observations and several series of model tests, including:

- The Brent B Condeep gravity platform in the North Sea in 140 m water depth during several severe storms the second winter after platform installation (Andersen & Aas 1980).
- The Troll A Condeep gravity platform with 36 m long skirts on soft clay in 303 m water depth installed in 1996.
- Five 1 g laboratory model tests of an offshore gravity base structure with monotonic and cyclic loading on a soft clay (Andersen et al. 1989).
- Twelve 1 g laboratory model tests with monotonic and cyclic loading on an offshore tripod gravity platform on soft clay (Aas & Andersen 1992).
- One monotonic and one cyclic centrifuge test of a gravity structure similar to the Ekofisk oil storage tank on very dense sand (Andersen et al. 1994).
- Two series of large scale field tests with monotonic and cyclic loading of offshore suction anchors in clays. One series was run with a load inclination of 10° with the vertical to simulate anchors for a tension leg platform, TLP (Andersen et al. 1993). The other series was run with a load inclination of 10° with the horizontal to simulate anchors with more horizontal loading (Keaveny et al. 1994).

The results of the comparison of calculated and measured displacements, resonant frequencies and capacities are presented in the references for the various model tests above. The calculated displacements, failure loads, type of failure surface, failure surface location, and failure mode (large permanent displacements, large cyclic displacements, or a combination) generally agreed very well with the measurements in all cases. As examples, some details are given below for the Troll A platform, the Brent B platform, the centrifuge model tests on very dense sand, and the large scale anchor field model tests in soft clay.

The soil stiffnesses were during design of the Troll A platform calculated by the procedure described in Sections 18.2 and 18.4. Interpretation of the natural frequencies measured during several storms during 1998 to 2005 indicate that the measured soil stiffnesses agree very well with the best estimate design soil stiffnesses (8 to 13% higher) (Kaynia et al. 2015).

Calculated and measured cyclic displacements of the Brent B Condeep platform during the second winter after installation in August 1975 are compared in Figure 19.1. The displacements are in terms of standard deviations during recording periods of 20 minutes. The probable maximum displacements would be about 4 times the standard deviation values. The storms reached a significant wave height of 10.3 m, corresponding to 2/3 of the design significant wave height. The design maximum wave height was 27.5 m. The calculated displacements were 1.06 and 0.71 of the measured values for rotations and horizontal displacements, respectively. The calculated soil stiffnesses also agreed well with the measured natural frequencies (Hansteen 1980).
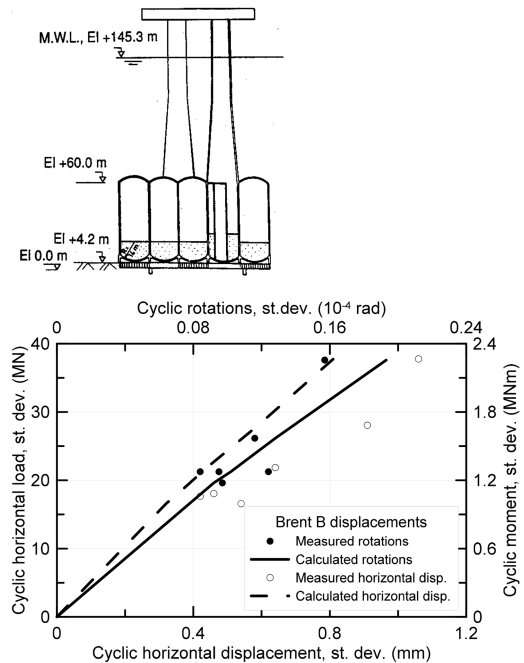
Figure 19.1. Calculated and measured horizontal and rotational displacements at seabed of the Brent B Condep platform (based on Andersen & Aas 1980).
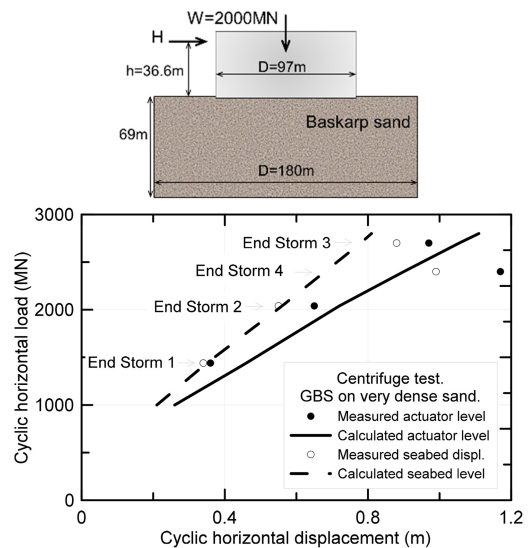
Figure 19.2. Comparison between calculated and measured displacements in centrifuge tests of a gravity platform on very dense sand (based on Andersen et al. 1994).

The calculated and measured cyclic displacements of the gravity structure modelled in the centrifuge tests on very dense sand are shown in Figure 19.2. The calculations are performed with the simplified finite element model described in Section 18.2. Similar agreement is later obtained with more refined

Table 19.1. Predicted and measured failure loads for the TLP field model tests.

Test No	Test type	Predicted/measured failure load
1	Monotonic	1.00
2	Cyclic	1.05
3	Cyclic	1.06
4	Cyclic	1.01

Figure 19.3. Geometry and soil characteristics of the TLP field model tests.

Figure 19.4. Predicted and measured rotations, TLP field model test.

Figure 19.5. Predicted and measured cyclic displacements, TLP field model Tests 2 and 3.

Figure 19.6. TLP model after being loaded to failure (Photo: R. Dyvik, NGI).

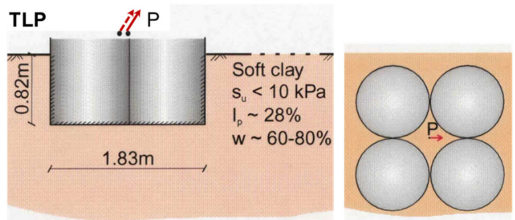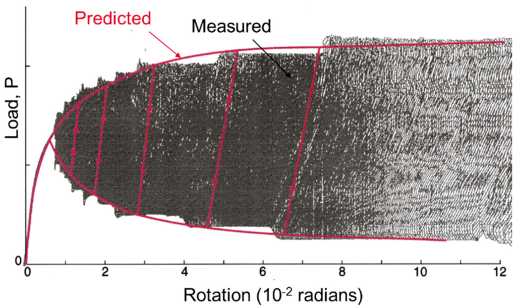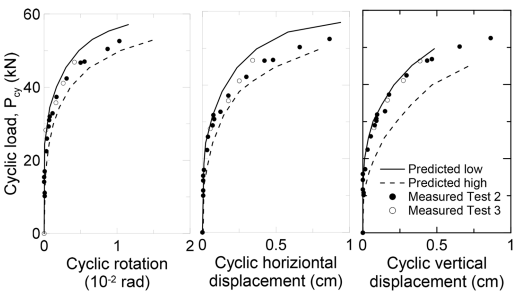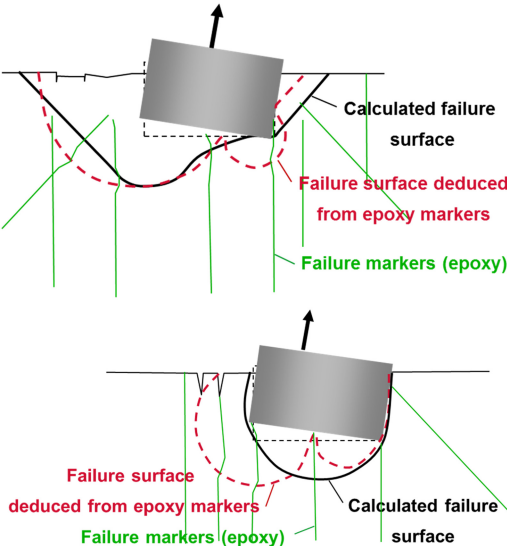Figure 19.7. Predicted and observed failure surfaces in TLP field model tests.

UDCAM analyses (Jostad et al. 2015). The calculated cyclic horizontal displacements at seabed and at actuator level are in good agreement with the measured values. Cavitation occurred in part of the foundation during Storms 3 and 4, but was not modelled in the calculations. This may explain the tendency for somewhat lower calculated displacements in these storms. The calculated cyclic rotations were greater than measured, but they were small, as they correspond to vertical displacements at the periphery of only about 1/5 of the horizontal displacements.

The centrifuge tests also showed that significant negative cyclic pore pressures could be relied upon in dense sand with essentially no fines. The maximum negative pore pressures are governed by the cavitation pressure, which depends on the water depth.

The applied cyclic loads were significantly higher than the design loads, and the results indicate that displacements rather than capacity may govern design in this case.

The model geometry and soil data for the TLP large scale anchor field tests are summarized in Figure 19.3. Capacities predicted prior to testing agree very well with the measured capacities, as can be seen from Table 19.1. Failure occurred as large permanent displacements, as indicated in Figure 19.4, which shows that predicted and measured displacements also agreed very well. Figure 19.5 shows that predicted and measured cyclic displacements also agreed well, even if

the cyclic displacements are small compared to the permanent displacements.

The model after it was brought to failure is shown in Figure 19.6. The predicted and observed failure surfaces in Figure 19.7 agree reasonably well, but with some differences. Back-calculations with the observed failure surfaces gave insignificant differences in the calculated capacities. The reason for the difference in failure surface between Test 4 and the other tests is that Test 4 was subjected to a greater moment.

20 SUMMARY AND CONCLUDING REMARKS

The contour diagram framework for cyclic soil parameters presented herein provides a sound basis for practical foundation design and has proven to be a useful and practical way to interpret and present cyclic soil data. This is supported by successful prediction and backcalculation of observed prototype behavior and model test results.

In addition to direct application in design, the framework also provides a basis for developing constitutive cyclic soil models and to check constitutive soil models for different stress conditions.

Even if one should be cautious about relying on correlations, it is hoped that the correlations herein for cyclic soil parameters with index parameters will provide useful guidance for practical projects and help to optimize the number of site specific cyclic tests. The same is true for the correlations presented for other parameters that are required in design of foundations under cyclic loading, such as initial shear modulus, static shear strength, friction angle and consolidation characteristics.

Focus has been given to the foundation design of structures, but the stability of a slope subjected to cyclic loading, such as from an earthquake, is also discussed. A structure and a slope can behave differently under cyclic loading because of the difference in safety factor under permanent load. In a slope, the cyclic loading is more likely to initiate increased rate of undrained creep strain, and failure may occur during or some time after the cyclic event.

The following gives a more detailed summary:

- Section 2 presents examples of situations where cyclic loading is important for the foundation design.
- Section 3 summarizes cyclic load characteristics, including load period and storm duration, for typical cases offshore, along the coast and on land.
- Section 4 identifies foundation design requirements where cyclic loading effects are important. This includes stability, cyclic displacements, soil stiffness and damping for dynamic soil structure calculations and earthquake analyses, permanent displacements due to cyclic loading, and soil reactions.
- Section 5 presents the soil parameters that are needed to address the foundation design requirements, grouped into cyclic soil data, monotonic soil data and consolidation characteristics.

- Section 6 describes the behavior of soil under cyclic loading and the laboratory tests that can be performed to determine the soil parameters that are needed in design. Attention is also drawn to the effect of drainage within a cycle and cavitation.
- Section 7 explains the contour diagram concept and how the contour diagrams can be constructed, both for shear strength, shear strains, pore pressure and damping. The construction requires both monotonic and cyclic tests.

The cyclic response, and thus the contour diagrams, depend on a number of factors, including relative density or water content, grain size distribution, plasticity index, overconsolidation ratio (OCR), sample preparation, consolidation time, load period, preshearing, strain-controlled vs. stress-controlled cycling, drained vs. undrained application of average shear stress, drainage within a cycle and cavitation. In some cases it can be important to distinguish between average and permanent shear strains.

A strategy for the laboratory testing to establish the contour diagrams is proposed, utilizing existing contours from the data base by first identifying contours for similar soils, and then running a few tests to check whether the diagrams can be used or modified for the actual soil. Additional tests will be required if the first tests do not fit existing contours well enough.

The normalized shear strength, τ_f/σ'_{vc}, is found to depend on the consolidation stress, σ'_{vc}. It is therefore proposed to normalize τ_f to $\sigma'_{ref} = p_a \cdot (\sigma'_{vc}/p_a)^n$, where p_a is the atmospheric pressure ($=100\,\text{kPa}$) and n is an empirical exponent, which is $n = 0.5$ for undrained static strength of sand and silt, $n = 0.9$ for undrained static strength of clay, and $n = 0.9$ for cyclic shear strength of sand and silt. Based on this, the shear stresses in the contour diagrams are normalized to the undrained static shear strength for clay and to σ'_{ref} for sand and silt.

- Section 8 shows how a design storm can be transformed into an equivalent number of the maximum load in the storm by accumulation procedures with pore pressure or shear strain as memory. It is shown that it is important to distinguish between stress-controlled and strain-controlled cyclic tests, and that strain-controlled cyclic tests can be predicted from stress-controlled tests, or vice versa, by the accumulation procedures.
- Section 9 points out that the target in situ relative density and water content for reconstitution are both challenging to determine. It is recommended to prepare sand and silt samples by wet tamping or water deposition, unless the silt content and the sample quality is high enough to use "intact" samples. It is shown that even sand and silt will creep during consolidation, and the specimens should be allowed to consolidate at least over night at the maximum consolidation stresses. The specimens should be presheared with representative cyclic shear stress and number of cycles, if it can be documented that

the foundation will be subjected to preshearing prior to the main design event. The cyclic soil parameters will depend on the load period. The number of cycles to failure relative to a 10 s load period can for clays be 5 times higher or smaller for 1 s and 100 s, respectively.

- Section 10 presents correlations of undrained static shear strength of sand and silt with both relative density and water content. The correlations show that the static strength depends on the fines content. Undrained shear strength of clay is given as a function of plasticity index. The shear strength anisotropy is more pronounced for sand than for clay, and increases with increasing relative density. The undrained shear strength increases with increasing overconsolidation ratio, but the effect is significantly smaller for dilatant than for contractant soils.

  The slope of the failure line in effective stress path plots, α', is correlated to relative density, water content and consolidation stress for drained DSS tests. α' for undrained tests is essentially independent of relative density, water content and consolidation stress, but decreases with increasing clay content and plasticity.

- Section 11 shows that the stress-strain behavior is highly non-linear and anisotropic. The anisotropy is, as for shear strength, more pronounced for sand than for clay, and increases with increasing relative density. The stress-strain properties also depend on the overconsolidation ratio, but more for clay than for dense sand.

  Correlations for the initial shear modulus show that the initial shear modulus decreases with increasing overconsolidation ratio when normalized with the undrained shear strength, and increases with overconsolidation ratio when normalized with the reference stress, σ'_{ref}. The initial shear modulus increases with decreasing plasticity index in both cases.

- Section 12 presents correlations of undrained cyclic shear strength of sand and silt with both relative density, water content and number of cycles. Examples of DSS and triaxial cyclic strength contour diagrams are presented for different soils and densities.

  The correlations show that the cyclic strength depends on the fines content. The cyclic shear strength also depends on the average shear stress. For dense sand the cyclic shear strength depends strongly on whether the additional average shear stress is applied drained or undrained, and for triaxial tests whether the drained average shear stress is applied by increasing or decreasing the normal stresses. The ratio of cyclic to static shear strength of clays decreases with decreasing plasticity.

  The cyclic shear strength anisotropy is more pronounced for sand than for clay, and increases with increasing relative density. The cyclic shear strength increases with increasing overconsolidation ratio, but the effect is significantly smaller for dilatant than for contractant soils.

Moderate preshearing increases the shear strength. Preshearing causing large shear strains may, however, break down the structure and reduce the shear strength. Special attention to negative effects should be given for overconsolidated soils.

The paper concentrates on non-carbonate soils, but correlations of cyclic DSS strengths of non-cemented carbonate soils with water content are presented in Section 12.9.

- Section 13 presents contours of cyclic and average shear strains as functions of number of cycles, and as functions of average and cyclic shear stresses, for sands and silts with different densities. The cyclic stress-strain behavior is non-linear and anisotropic. The stress-strain behavior also depends on the overconsolidation ratio, but more for clay than for sand.

- Section 14 presents contours of permanent pore pressure as a function of number of cycles, and as a function of average and cyclic shear stresses, for sands and silts with different densities.

- Section 15 show data that seem to indicate that that the damping ratio increases with increasing shear strain and number of cycles, but contours for damping are not established.

- Section 16 proposes expressions for virgin, unloading and reloading constrained moduli, and parameters are correlated to fines content and water content. Reloading moduli for clays are found to increase significantly with decreasing plasticity index.

- Section 17 shows that the vulnerability of a soft clay slope to cyclic loading, including earthquakes, depends on the permanent shear strain that develops during the cyclic event, and that a failure can occur due to accelerated creep during or after the cyclic event.

- Section 18 describes commonly used procedures of different complexity to calculate capacity, cyclic displacements, permanent displacements, and soil spring stiffnesses. A procedure to calculate behavior during a cycle is also described.

- Section 19 presents prediction and backcalculation of several different prototype observations and model tests that verify the soil models and the calculations procedures proposed herein.

Such work is also dependent on the varying challenges faced by the industry and the subsequent support from NGI's many clients over the years, including joint industry sponsored projects and research funded by the Research Council of Norway. The cooperation with colleagues from the industry has always been inspiring and rewarding.

I would therefore also like to acknowledge this important contribution from colleagues at NGI and within the industry, in addition to their willingness to share some of the results and information presented herein.

REFERENCES

Aas, P.M. & Andersen, K.H. 1992. Skirted foundations for offshore structures. *9th Offsh. South East Asia Conf. & Exhib*.

Andersen, K.H. 1976. Behavior of clay subjected to undrained cyclic loading. *Int. Conf. on Behaviour of Offsh. Struct., BOSS'76.* Trondh., Proc. (1): 392–403. Also NGI Pub. 114.

Andersen, K.H., Hansteen, O.E., Høeg, K. & Prévost, J.H. 1978. Soil deformations due to cyclic loads on offshore structures. *Numerical methods in offshore engineering*. Ed. by O.C. Zienkiewicz, R.W. Lewis & K.G. Stagg. Chichester, Wiley, pp. 413–452. Also NGI Pub. 120.

Andersen, K.H., Pool, J.H., Brown, S.F. & Rosenbrand, W.F. 1980. Cyclic and static laboratory tests on Drammen clay. *ASCE, J. of Geotech. Engrg.,* 106, (5): 499–529.

Andersen, K.H. & P.M. Aas. 1980. Foundation performance. *Shell Brent "B" Instrumentation Project. Seminar. Society for Underwater Technology.* Proc.: pp. 57–77. London 1979. Also in NGI Pub. 137.

Andersen, K.H. 1981. Discussion on "Pore pressure generation during variable cyclic loading" by Dyvik et al. *Int. Conf. on Recent Advances in Geotech. Earthquake Engrg and Soil Dynamics*, St Louis, MO. Proc., (III): 920–921.

Andersen, K.H. 1988. Properties of soft clay under static and cyclic loading. Invited lecture. *Int. Conf. on Engrg. Probl. of Regional Soils,* Proc., pp. 7–26, Beijing, China. Ed. by Chinese Inst. of Soil Mech. & Found. Engrg. Also: NGI Pub. 176.

Andersen, K.H., Kleven, A. & Heien, D. 1988. Cyclic soil data for design of gravity structures. *ASCE, J. of Geotech. Engrg*, 114 (5): 517–539.

Andersen, K.H. & Lauritzsen, R. 1988. Bearing capacity for foundations with cyclic loads. *ASCE, J. of Geotech. Engrg*, 114 (5): 540–555.

Andersen, K.H., Dyvik, R., Lauritzsen, R., Heien, D., Hårvik, L. & Amundsen, T. 1989. Model tests of offshore platforms. II. Interpretation. *ASCE, J. of Geotech. Engrg.*, 115 (11): 1550–1568.

Andersen, K.H. 1991. Foundation design of offshore gravity structures. Chapter 4 in *"Cyclic Loading of Soils. From Theory to Design"*. Ed. by M.P. O'Reilly and S.F. Brown. Publ. by Blackie & Son Ltd., pp. 122–173. Also in NGI Publ. 185.

Andersen, K.H. & Høeg, K. 1991. Deformations of soils and displacements of structures subjected to combined static and cyclic loads. *X ECSMFE*, Firenze, Proc., (4): 1147–1158.

Andersen, K.H., Dyvik, R., Schrøder, K. & Bysveen, S. 1993. Field tests of anchors in clay. II: Prediction and interpretation. *ASCE, J. of Geotech. Engrg.,* 119 (10): 1532–1549.

Andersen K.H., Dyvik, R., Kikuchi, Y. and Skomedal, E. 1992. Clay behaviour under irregular cyclic loading. Proc. *Int. Conf. on Behav. of Offsh. Structures*, London, (2): 937–950.

Andersen, K.H., Allard, M.A. & Hermstad, J. 1994. Centrifuge model tests of a gravity platform on very dense sand; II: Interpretation. *7th Int. Conf. on Behavior of Offshore Structures. BOSS'94*. Cambridge, Mass. Proc. (1): 255–282.

Andersen K.H. & Berre, T. 1999. Behaviour of a dense sand under monotonic and cyclic loading. *12th European Conf. on Soil Mech. and Geotechnical Engrg*. Amsterdam, The Netherlands. Proc. (2): 667–676. A.A. Balkema.

Andersen, K. H. & Jostad, H.P. 2002. Shear strength along outside wall of suction anchors in clay after installation. Proc. *XII ISOPE Conf.*, Kyushu, Japan.

Andersen, K.H. & Jostad, H.P. 2004. Shear strength along inside of suction anchor skirt wall in clay. Proc. Paper 16844, *OTC*, Houston.

Andersen, K.H. 2004. Cyclic clay data for foundation design of structures subjected to wave loading. Keynote Lecture; Proc., *Intern. Conf. on Cyclic Behavior of Soils and Liquefaction Phenomena, CBS04*, Bochum, Germany, 31.3–2.4, 2004, p. 371–387, A.A. Balkema, Ed Th. Triantafyllidis.

Andersen, K.H., Lunne, T., Kvalstad, T.J. & Forsberg, C.F. 2008. Deep water geotechnical engineering. *XXIV Nat. Conf. of Mexican Soc. of Soil Mechanics*, Aguascalientes, Nov. 2008. Proc., (IV): 57p. Also in NGI Pub. 208.

Andersen, K.H. 2009. Bearing capacity of structures under cyclic loading; offshore, along the coast and on land. 21st Bjerrum Lecture presented in Oslo 23 November 2007. *Can. Geotech. J.* 46: 513.535. Also: Norsk Geoteknisk Forening, Bjerrums Foredrag Nr. 21.

Andersen, K.H. & Schjetne, K. 2013. Data base of friction angles of sand and consolidation characteristics of sand, silt and clay. *ASCE J. of Geotech. & Env. Engrg.,* 139 (7), 1140–1155.

Andersen, K.H., Puech, A. & Jardine, R. 2013. Cyclic resistant geotechnical design and parameter selection for offshore engineering and other applications. *XVIIIth ICSMGE, TC209 Workshop – Design for cyclic loading; piles and other foundations*, Proc., Paris, 4 Sept. 2013.

Anderson, D.G. & Stokoe, K.H. 1978. Shear modulus: A time dependent soil property, Dynamic Geotechnical Testing. *ASTM STP 654*, pp. 60–90.

ASTM E1049-85. 2011. Standard Practices for Cycle Counting in Fatigue Analysis, *ASTM International*, West Conshohocken, PA. www.astm.org.

Berre, T., Lunne, T., Andersen, K.H., Strandvik, S. & Sjursen, M. 2007. Potential improvements of design parameters by taking block samples of soft marine Norwegian clays. *Can. Geotech J.* (44): 698–716.

Bjerrum, L. 1967. Engineering geology of Norwegian norrnally-consoIidated marine clays as related to settlements of buildings. 7th Rankine Lecture. *Geotechnique*, 17 (2): 81–117.

Bjerrum, L. 1973. Geotechnical problems involved in foundations in the North Sea. *Geotechniqu*e 23 (3): 319–358.

Blaker, Ø. & Andersen, K.H. 2015. Shear strength of dense to very dense Dogger Bank sand. Proc., *Int. Symp. on Frontiers in Offshore Geotechics, ISFOG*, Oslo, Norway.

Blaker, Ø., Lunne, T., Vestgården, T., Krogh, L., Thomsen, N.V., Powel, J.J.M. & Wallace, C.F. 2015. Method dependency for determining maximum and minimum dry unit weights of sands. Proc., *Int. Symp. on Frontiers in Offshore Geotechnics, ISFOG*, Oslo, Norway.

Evans, M. D. & Zhou, S. 1995. Liquefaction behavior of sand-gravel composites. *ASCE J. Geotech. Engrg.* 121 (3): 287–299.

Finnie, I.M.S., Hospers, B., Nowacki, F., Andersen, K.H. & Kalsnes, B. 1999. Cyclic simple shear behavior of a carbonate sand. 2nd *Int. Conf. on Engineering for calcareous sediments*, Bahrain. Proc. Vol. 1, 87–100. Ed. Al-Shafei. Balkema, Rotterdam, ISBN 90 5809 037X.

Hansteen O.E. 1980. Dynamic performance. *Shell Brent "B" Instrumentation Project. Seminar. Society for Underwater Techn.,* Proc.: 89–107. London 1979. Also in NGI Pub. 137.

Hansteen, O.E. 1991. Description of INFIDEL-A nonlinear 3-D FE Program. *NGI Internal Report* 514093-3, 9 Sept. 1991.

Heiberg, S. 1973. A method of analysis of the dissipation of excess pore pressure induced during cyclic loading. *NGI Internal Report* 51504-1.

Hight, D.W. & Lerouel, S. 2003. Characterisation of soils for engineering purposes. Intern. Workshop on Characterisation & Engrg. Properties of Natural Soils, Singapore: Balkema, 1, 255–360.

Høeg, K., Dyvik, R. & Sandbækken, G. 2000. Strength of undisturbed versus reconstituted silt and silty sand specimens. *ASCE, J. Geotech. & Geoenv. Engrg.* 126 (7): 606–617.

Ishihara, K. & Takatsu, H. 1979. Effects of overconsolidation and K conditions on the liquefaction characteristics of sands. *Soils & Foundations* 19 (4): 59–68.

Jamiolkowski, M. & Manassero, M. 1995. The role of in-situ testing in geotechnical engineering – thoughts about the future. Proc., *Int. Conf. in Advances in Site Investigation Practice.* Thomas Telford, pp. 929–951.

Janbu, N. 1963. Soil compressibility as determined by oedometer and triaxial tests. Proc. 3rd European Conf. on Soil Mechanics., Wiesbaden 1: 19–25.

Jardine, R., Puech, A. & Andersen, K.H. 2012. Cyclic loading of offshore piles: Potential effects and practical design. Keynote Lecture. *7th Intern. Offshore Site Investigation and Geotechnics Conf.,* Sept. 2012, London, UK, Proc. p. 59–100.

Jeanjean, P., Andersen, K.H. & Kalsnes, B. 1998. Soil parameters for design of suction caissons for Gulf of Mexico deepwater clays. *OTC*, Houston, Proc., Paper 8830.

Johansson, J., Løvholt, F., Andersen, K.H., Madshus, C. & Aabøe, R. 2013. Impact of blast vibrations on the release of quick clay slides. Proc., *XVIIIth ICSMGE*, Proc., Paris

Jostad, H.P., Andersen, K.H. & Tjelta, T.I. 1997. Analyses of skirted foundations and anchors in sand subjected to cyclic loading. Proc., *Int Conf on Behavior of Offsh Structures*, 8. Delft, The Netherlands, (1): 49–162. Also NGI Pub 199.

Jostad, H.P., Grimstad, G., Andersen, K.H., Saue, M., Shin, Y. & You, D. 2014. A FE procedure for foundation design of offshore structures – applied to study a potential OWT monopile foundation in the Korean Western Sea. *Geotech. Engrg. J. of SEAGS & AGSSEA*, Vol. 45 (4), Dec 2014.

Jostad, H.P., Grimstad, G., Andersen, K.H. & Sivasithamparam, N. 2015. A FE procedure for calculation of cyclic behaviour of offshore foundations under partly drained conditions. Proc., *Int. Symp. on Frontiers in Offshore Geotechnics, ISFOG*, Oslo, Norway.

Karlsrud, K. & Nadim, F. 1990. Axial capacity of offshore piles in clay. Proc., *22nd OTC*, Houston, Paper 6245, pp. 404–416.

Karlsrud, K. & Hernandez-Martinez, F.G. 2013. Strength and deformation properties of Norwegian clays from laboratory tests on high quality block samples. Canadian Geotechnical Journal. 50 (12): 1273–1293.

Kaynia, A.M. & Andersen, K.H. 2015. Development of nonlinear foundation springs for dynamic analysis of platforms. Proc., *Int. Symp. on Frontiers in Offshore Geotechnics, ISFOG*, Oslo, Norway, June 2015.

Kaynia, A.M., Noren-Cosgriff, K., Andersen, K.H. & Tuen, K.A. 2015. Nonlinear foundation spring and calibration against measured dynamic response of structure. Proc., *34th OMAE 2015-41236*, St. Johns's, NL, Canada.

Keaveny, J.M., Hansen, S.B., Madshus, C. & Dyvik, R. 1994. Horizontal capacity of large scale model anchors. Proc., *XIII ICSMFE.* New Delhi 1994. Vol. 2, pp. 677–680.

Kleven, A. & Andersen, K.H. 1991. Cyclic laboratory tests on Storebælt clay till. *Seminar, Design of Exposed Bridge Piers. Danish Soc. of Hydr. Engrg.* Copenh., Denmark. Also in NGI Pub. 199.

Kokusho, T., Hara, T. & Hiraoka, R. 2004. Undrained shear strength of granular soils with different particle gradation. *ASCE J. Geotech. and Geoenv. Engrg.*, 130 (6): 621–629.

Kort, A., Pederstad, H.J. & Nowacki, F. 2015. Planning of soil investigation for GBS foundation design. Proc., *Int. Symp. on Frontiers in Offsh. Geotechnics, ISFOG*, Oslo, Norway.

Ladd, C.C. & Foot, R. 1974. New design procedure for stability of soft clays. *ASCE, J. of Geotech. Engrg.,* 100 (7): 763–786.

Lambe, T.W. & Whitman, R.V. 1969. Soil Mechanics. *John Wiley & Sons, Inc.*

Lee, K. & Vernese, F.J. 1978. End restraint effects on cyclic triaxial strength of sand. *ASCE. J. Geotech. Engrg.*, 104 (6): 705–719.

Li, L.L., Dan, H.B. & Wang, L.Z. 2011. Undrained behaviour of natural marine clay under cyclic loading, *Ocean Engineering,* 38: 1792–1805.

Lunne, T., Berre, T., Andersen, K.H., Strandvik, S. & Sjursen, M. 2006. Effects of sample disturbance and consolidation procedures on measured shear strength of soft marine Norwegian clays. *Can. Geotech. J.* 43: 726–750.

Lunne, T. & Andersen, K.H. 2007. Soft clay shear strength parameters for deepwater geotechnical design. Keynote Address; Proc., *6th International Offshore Site Investigation and Geotechnics Conf.*; Confronting New Challenges and Sharing Knowledge, pp. 151–176, Sept. 2007, London, UK.

Lunne, T., Andersen, K.H., Yang, S.L., Tjelta, T.I. & Strøm, P. 2012. Undrained shear strength for foundation design at the Luva deep water field in the Norwegian Sea. Proc., *ICS4*, Brazil, Sept., 2012.

Madshus, C. & Hårvik, L. 1988. Solutions to the consolidation equation for some different geometries and initial pore pressure distributions. *NGI Internal Report* 514150–1.

Masing, G. 1926. Eigenspannungen und Verfestigung beim Messing. *Proc. 2nd International Congress on Applied Mechanics*, Zurich. pp. 332–335

Matsuishi, M. & Endo, T. 1968. Fatigue of metals subjected to varying stress, *Japan Soc. Mech. Engineering*

McManus, K.J. & Davis, R.O. 1997. Dilation-induced pore fluid cavitation in sands. *Geotechnique* 47 (1): 173–177.

Mesri, G., Feng, T. W. & Benak, J. M. 1990. Post densification penetration resistance of clean sands, *J. of Geotech. Engrg., A.S.C.E.*, 116 (7): 1095–1115.

Mitchell, J.K. 2004. Time – The Fourth Dimension of Soil Behavior in Geotechnical Engrg. *17th Nabor Carrillo Lecture*, ISBN 968-5350-12-4, 73 pp.

Mulilis, J.P., Seed, H.B., Chan, C.K., Mitchell, J.K. & Arulanandan, K. 1977a. Effects of sample preparation

on sand liquefaction. *ASCE, J. Geotech. Engrg.* 103 (2): 91–108.

Mulilis, J.P., Mori, K., Seed, H.B. & Chan, C.K. 1977b. Resistance to liquefaction due to sustained pressure. *ASCE, J. Geotech. Engrg.*, 103 (7): 793–797.

Norén-Cosgriff, K., Jostad, H.P. & Madshus, C. 2015. Idealized load composition for determination of cyclic undrained degradation of soils. *Proc., Int. Symp. on Frontiers in Offshore Geotechnics, ISFOG*, Oslo, Norway.

Papadopoulou, A. & Tika, T. 2008. The effect of fines on critical state and liquefaction resistance characteristics of non-plastic silty sands. *Soils and Foundations*, 48 (5): 713–725.

Oda, M., Kawamoto, K., Suzuki, K., Fujimori, H. & Sato, M. 2001. Microstruct. interpret. on reliquefaction of saturated granular soils under cyclic loading. *ASCE J. Geotech. and Geoenv. Engrg.* 127 (5): 416–423.

Quiros G.W., Little R.L. & Garmon S. 2000. A normalized soil parameter procedure for evaluating in situ undrained shear strength. Proc. *OTC*, Houston, USA. Paper 12090.

Seed, H.B. & Idriss, I.M. 1970. Soil moduli and damping factors for dynamic response analysis. *Earthq. Engrg. Res. Center*. Report EERC70-10.

Siddiqi, F.H. 1984. Strength evaluation of cohesionless soils with oversized particles. *PhD dissertation, University of California, Davis*, Calif.

Silver, M.L., Chan, C.K., Ladd, R.S., Lee, K.L., Tiedemann, D.A., Townsend, F.C., Valera, J.E. & Wilson, J.H. 1976. Cyclic triaxial strength of standard test sand. *ASCE, J. Geotech. Eng.,* 102(5): 511–524.

Tanaka, Y., Kudo, K., Yoshida., Y. & Ikemi, M. 1987. A study on the mechanical properties of gravel – Dynamic properties of reconstituted sample. Res. Rep. No. U87019, *Centr. Res. Inst. of Electric Power Industry,* Akibo, Japan (in Japanese).

Tatsuoka, F., Toki, S., Miura, S., Kato, H., Okamoto, M., Yamada, S., Yasuda, S. & Tanizawa, F. 1986a. Some factors affecting cyclic undrained triaxial strength of sand. *Soils & Foundations.* 26 (3): 99–116.

Tatsuoka, F., Ochi, K., Fujii, S. & Okamoto, M. 1986b. Cyclic undrained triaxial and torsional shear strength of sands for different sample preparation methods. *Soils & Foundations.* 26 (3): 23–41.

Tatsuoka, F., Kato, H., Kimura, M. & Pradhan, T.B.S. 1988. Liquefaction strength of sands subjected to sustained pressure. *Soils and Foundations*. 28 (1): 119–131.

Vaid, Y.P., Sivathayalan, S. & Stedman, D. 1999. Influence of specimen reconstitution method on the undrained response of sand. *ASTM Geotech. Testing J.* 22 (3): 187–195.

Wichtmann, T., Andersen, K.H., Sjursen, M.A. & Berre, T. 2013. Cyclic tests on high-quality undisturbed block samples of soft marine Norwegian clay. *Can. Geotech. J.* (50): 400–412. (2013) dx.doi.org/10.1139/cgj-2011-0390.

Wijewickreme D. & Sanin, M. 2005. Some observations on the cyclic loading response of a natural silt. Proc. *XVI ICSMGE*, Osaka, pp. 627–631.

Wong., R.T., Seed, H.B. & Chan, D.K. 1975. Cyclic loading liquefaction of gravelly soils. *ASCE, J. Geotech. Engrg*. 101 (6): 571–583.

Yang, S., Sandven, R. & Grande, L. 2004. Cyclic behaviour of sand-silt mixtures. Proc., *Intern. Conf. on Cyclic Behavior of Soils and Liquefaction Phenomena,* CBS04, Bochum, Germany, pp. 269–274, A.A. Balkema, Ed. Th. Triantafyllidis.

Yasuhara, K. & Andersen, K.H. 1991. Recompression of normally consolidated clay after cyclic loading. *Soils and Foundations.* 31 (1): 83–94. March 1991.